CHALMERS

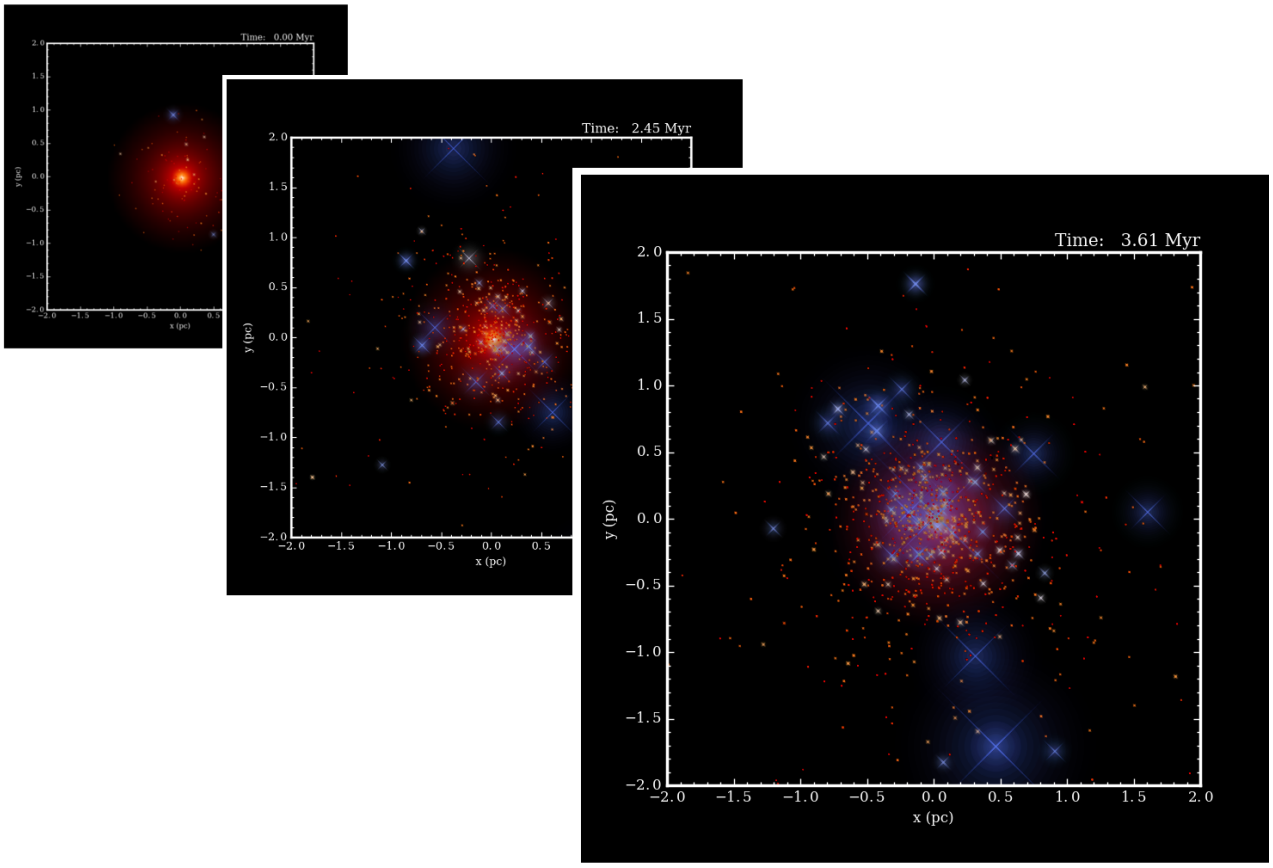

The Dynamics of Star Cluster Formation

JUAN PABLO FARIAS

Department of Earth, Space and Envirionment
CHALMERS UNIVERSITY OF TECHNOLOGY
Göteborg, Sweden 2018

Thesis for the degree of Licentiate of Philosophy

The Dynamics of Star Cluster Formation

Juan Pablo Farias

Department of Earth, Space and Envirionment
CHALMERS UNIVERSITY OF TECHNOLOGY
Göteborg, Sweden 2018

The Dynamics of Star Cluster Formation
Juan Pablo Farias

Department of Earth, Space and Envirionment
Chalmers University of Technology
SE–412 96 Göteborg, Sweden
Telephone + 46 (0) 31 – 772 1000

Cover: The formation and dynamical evolution of model young star cluster, background gas is modeled as an analytical potential which decrease as stars are born. See Paper II.

Typeset by the author using LaTeX.

Printed by Chalmers Reproservice
Göteborg, Sweden 2018

Abstract

A major question in astrophysics is how star clusters form. These objects are important, since they are the birth sites of most stars, perhaps including our own Sun.

There are different theoretical models of cluster formation and our main goal is to examine how they may affect the dynamical evolution of the stars in the system, including those stars that are ejected from the cluster. In particular, we set up cluster formation models with global initial conditions of the Turbulent Clump Model, which has been proposed as a description of gas structures within molecular clouds. We then investigate how global star formation efficiency from such a natal gas clump, overall clump density, degree of primordial mass segregation, degree of primordial binarity and binary population properties affect the subsequent dynamical evolution. In a second paper, after a major code development that allows modeling of gradual star formation, we investigate how the rate of star cluster formation affects its dynamical evolution, which is the first time such a study has been conducted for realistic clusters that have realistic binary properties.

We show througth this thesis that star clusters that formed fast, i.e., during about one free-fall time, show quite different properties than star clusters that forms in a slow quasi-equilibirum fashion. Quickly-formed clusters tend to expand much faster compared to slow-formed clusters, thus requiring higher initial densities to agree with observations. Creation of the runaway stellar population is also sensitive to the rate of cluster formation. Future directions of this work, adding greater degrees of realism are also discussed.

Finally, we carry out an example study of how the observed properties of a particular set of runaway stars can constrain properties of the dynamical ejection event, with implications for the closest region of massive star formation in the Orion Nebula Cluster.

Acknowledgments

First, I would like to thank my supervisor Jonathan Tan for all his support and shared knowledge, and also for inviting me to join on this adventure to the North. It has been an honor to work with him and to see how much a passionate and dedicated person can do. Working with him have certainly encouraged me to improve and to look more into my own future.

Starting my PhD here would not have been possible without the help of Wouter Vlemmings, who have been always there to help and clarify any problem or question we had. As well as to Camilla Andersson and Paula Rossell, for their patience and good will in helping me with a system that had overwhelmed me many times. In general, to all the people at the Onsala Space Observatory that have received me so well.

I would like to specially thank to my wife, Daniela, for taking the brave decision to come with me even though it has meant to be far from the people that she loves. I will always grateful for her company and support in these difficult, but enricher times. Also to my daughter Luna, that has been the (literal) reason to wake up in the morning and made my day every day with her joy.

List of Publications

This thesis is based on the following appended papers:

Paper I. Juan P. Farias, Jonathan C. Tan, Sourav Chatterjee. *Star Cluster Formation from Turbulent Clumps. I. The Fast Formation Limit.* The Astrophysical Journal, Volume 838, page 116. (2017)

Paper II. Juan P. Farias, Jonathan C. Tan, Sourav Chatterjee. *Star Cluster Formation from Turbulent Clumps. II. Gradual Star Cluster Formation.* Preparing for submission to The Astrophysical Journal.

Paper III. Juan P. Farias & Jonathan C. Tan. *On the formation of Runaway Stars BN and x in the Orion Nebula Cluster.* Accepted by Astronomy & Astrophysics Letters.

Contents

Chapter 1

Introduction

A major question in Astrophysics is how and where star formation happens. Many aspects of star formation are still under active debate, and the reason of such long debate is the complexity of the process. Star formation involves a wide range of scales and the interaction of multiple physical mechanisms. However, some agreement exists that the majority of stars appear to form in "clusters" instead of in isolation (e.g. Bressert et al. 2010; Gutermuth et al. 2009; Lada and Lada 2003). Therefore, to understand star formation it is necessary to understand how star clusters form.

There is a long standing debate on whether star cluster formation is a short process that happens in about one single cloud collapse timescale, i.e., a "free-fall timescale" (Elmegreen 2000, 2007; Hartmann and Burkert 2007), or if it takes place over a longer duration with clouds evolving in a quasi-equilibrium state (Nakamura and Li 2007; Tan et al. 2006). Star cluster formation, like individual star formation, is the result of a complex interaction of numerous physical processes inside molecular clouds. Star-forming regions are massive, self-gravitating systems, supported by a combination of magnetic fields and turbulent motions. Thermal pressure is not important on these scales, as gas in molecular clouds is able to cool to about 10 K. Formation of stars involves gas infall, accretion via disks, and jets and winds launched from these disks that enhance and support turbulence (Nakamura and Li 2007, 2014), i.e., part of the process of "feedback". Other forms of feedback, include when newly formed stars irradiate energy into their environments (e.g. Dale et al. 2015), launch stellar winds and ultimately when the most massive stars explode as supernovae injecting large amounts of energy into the clouds, potentially dispersing residual gas within the cluster.

It is extremely challenging to conduct a numerical simulation that accounts for all the physics involved during star cluster formation and with the necessary resolution to follow these processes accurately. Thus it can be useful and insightful to address the problem from different angles. Since the main ingredient during the transition from a molecular cloud to a star cluster is the dynamics of the gas, many studies have been focused on reproducing the outcome of star formation from hydrodynamical and magneto-hydrodynamical (MHD) simulations (e.g. Bate 2009; Dale et al. 2015; Gavagnin et al. 2017; Girichidis et al. 2012; Wu

et al. 2017). However, these kind of studies are very expensive computationally and only few simulations can be done per study. Furthermore, these simulations are still limited in their spatial resolution and typically cannot accurately follow the close orbits and interactions of stars, e.g., in typical binary systems with separations of less than 100 AU. Furthermore, star formation in typical clusters involves sparse sampling of the stellar initial mass function (IMF), especially at its upper end. It is thus a stochastic problem, which can only be addressed by an statistical approach involving analysis of many simulation realizations, which is not possible from expensive hydrodynamical simulations.

In this thesis we aim to address this problem by a statistical study of the dynamics of stars during the formation of star clusters. In order to achieve this, we accurately follow the dynamics of the stars, given simple assumptions, approximations and parameterizations for the individual star formation and the global cluster formation processes. We are then able to explore by numerical experiments the influence of these assumptions, approximations and parameterizations for the dynamical evolution of the clusters and their general properties, including for stars that escape from the clusters.

Here in Chapter 1 we introduce basic concepts of stellar dynamics that will be discussed during this thesis. In Chapter 2 we overview the physics involved in the evolution of star clusters. In Chapter 3 we describe the numerical codes used in this work and in Chapter 4 we introduce the appended papers that discuss our results.

1.1 Basic concepts

1.1.1 The virial theorem

The virial theorem applied to gas free stellar clusters, states that a system is in *virial equilibrium* if:

$$T_* = -\frac{1}{2}\sum_{\rm i=1}^{N} \mathbf{F}_{\rm i} \cdot \mathbf{r}_{\rm i} \tag{1.1}$$

$$= -\frac{1}{2}\Omega_{\rm tot} \tag{1.2}$$

where T_* is the kinetic energy of all stars in the cluster, $\mathbf{F}_{\rm i}$ is the force felt by the $i^{\rm th}$ particle by the other $N-1$ particles, $\mathbf{r}_{\rm i}$ is the position of the $i^{\rm th}$ star and $\Omega_{\rm tot}$ is the total potential energy of the cluster (Aarseth 2003). However, not all systems are in virial equilibrium and it is useful to characterize a system by its relation to the virial theorem.

Virial ratio, Q, is the ratio defined by the kinetic and total potential energies of the cluster, i.e.:

$$Q = -\frac{T_*}{\Omega_{\rm tot}}. \tag{1.3}$$

Depending on this value, we call a system with: $Q < 0.5$, a cold system, i.e., a highly bound system with low velocity particles; $Q = 0.5$, a system in virial equilibrium; $0.5 < Q < 1$, a hot system with high velocity particles; and $Q > 1$, an unbound system where a significant fraction

of particles have velocities higher than the escape velocity[1].

Virial radius, $r_{\rm vir}$, is characteristic length unit commonly used in numerical simulations (Aarseth 2003; Heggie and Hut 2003). It is defined in terms of the potential energy of an isolated system by:

$$r_{\rm vir} = -\frac{GM_*^2}{2\Omega_*} \tag{1.4}$$

where M_* and Ω_* are the system mass and potential energy of the system.

1.1.2 Dynamical timescales

One of the most debated features of star cluster formation is the timescale on which it happens, and this particular issue is the most important parameter we wish to constrain. The relevant timescales regarding star cluster formation and stellar dynamics are:

Free-fall time, $t_{\rm ff}$, is a commonly adopted timescale used in star formation simulations. The free-fall time defines the time it would take to a cloud of mass M and radius R to collapse under it own weight if no other forces support it against gravity. It only depends on the volume density of the cloud (ρ) and can be calculated to be:

$$t_{\rm ff} = \sqrt{\frac{3\pi}{32G\rho}} \tag{1.5}$$

for a uniform density sphere.
Crossing time, $t_{\rm cross}$, is a typical timescale used in stellar dynamics denoting the timescale for needed for a typical particle to cross the system, i.e., $t_{\rm cross} = 2R/v$ where R is the radius of the system and v is the typical speed of a star in the system. The value of v will depend of the dynamical state of the system, i.e., a hot system will have higher v than a cold system. The crossing time is generally used as a characteristic timescale, often used as the time against which to compare some other dynamical process.

A typical velocity of a stellar system is the velocity dispersion (σ) of the particles. Assuming virial equilibrium, we can define the crossing time as (see Aarseth 2003):

$$t_{\rm cross} \approx 2\frac{r_{\rm v}}{\sigma} \tag{1.6}$$

In virial equilibrium we can estimate the value of σ by $\sigma^2 \approx GM/2r_{\rm vir}$ where G is Newton's gravitational constant and M is the total mass of the cluster. Thus the crossing time can be estimated as (Aarseth 2003; Heggie and Hut 2003):

$$t_{\rm cross} \approx 2\sqrt{\frac{2r_{\rm vir}^3}{GM}} \tag{1.7}$$

[1]Note that this does not mean that the whole stellar system is completely unbound. In fact it can be shown that a system with $Q = 1$ that follows a Maxwell-Boltzmann velocity distribution would have ∼65% of their particles bound (see Farias et al. 2018) and figure 2.3.

This last equation is particularly useful in numerical simulations since a typical N-Body code uses units such that $G = 1$, $M = 1$ and $r_{\rm vir} = 1$ and thus $t_{\rm cross} = 2\sqrt{2}$.

Relaxation time, $t_{\rm relax}$, is the timescale on which a typical star in the system will lose any memory of its initial energy and angular momentum through interactions with other stars. It can also be defined as the typical timescale that a system needs to reach dynamical equilibrium or to come back to equilibrium after been disturbed. An useful approximation of this timescale is derived in Binney and Tremaine (1987) as:

$$t_{\rm relax} \approx \frac{0.1N}{\ln N} \times t_{\rm cross}. \tag{1.8}$$

This relation only depends on the number of particles in the system, and it is very important to understand the difference between a *collisional* and *collisionless* regime.

For galaxies with $N \approx 10^{11}$ stars and an age of approximately 10 Gyr and a few hundred crossing times old, the relaxation time-scale for the whole system is much longer than the age of the Universe, and it is possible to neglect the contribution from close encounters, i.e., these are *collisionless* systems.

On the other hand a globular cluster (GC) with $N \approx 10^5$ members and a relaxation time of $t_{\rm relax} \approx 100$ Myr, close encounters may be important over the lifetime of the cluster of ~ 10 Gyr and we can not ignore close encounters, i.e., these are *collisional* systems.

In general a system is called collisional when its lifetime or the time range that we are interested in is much greater than $t_{\rm relax}$, and collisionless when the time-scale of interest is much smaller than $t_{\rm relax}$. In this thesis we focus on highly collisional systems, so we need to follow their evolution accordingly.

1.2 The stellar population

Initial mass function (IMF), is the distribution function of individual masses of stars at birth on a given star formation event. Introduced by Salpeter (1955). A common form of this function is:

$$\xi(m) = \frac{dN}{dm} \propto m^{-\alpha}, \tag{1.9}$$

where m is the mass of a star and N the number of stars with masses in the range $m + dm$. Salpeter (1955) derived a slope of $\alpha = 2.35$ for stellar masses in the range $0.4 - 10\,{\rm M}_\odot$, however it has been found that this value overestimates the number of low mass stars, where this slope has been found to be shallower, and many variations have been proposed over the years (e.g. Chabrier 2003; Kroupa et al. 1990; Miller and Scalo 1979). In these works, it have been shown that the IMF slope varies in different mass ranges. Kroupa (2001) has proposed a three part power law, usually referred to as the canonical IMF, equivalent to equation 1.9 with the slopes:

$$\alpha = \begin{cases} 0.3 & , 0.01 \leq m/{\rm M}_\odot < 0.08, \\ 1.3 & , 0.08 \leq m/{\rm M}_\odot < 0.5, \\ 2.3 & , m/{\rm M}_\odot \geq 0.5 \end{cases} \tag{1.10}$$

This form of the IMF is adopted in this thesis to sample the initial stellar masses in our star cluster simulations.

Stellar binaries are pairs of stars orbiting each other. Stellar binaries are very important for stellar dynamics as they can store large amounts of energy in their orbits, and they can exchange this energy with nearby stars. The nature of the interchange of energy will depend on the relation between their internal binding energy and their environment. The internal mechanical energy of a binary is given by:

$$E_{\rm bin} = -G\frac{m_1 m_2}{2a}, \tag{1.11}$$

where m_1 and m_2 are the masses of the components and a is the semi-major axis of their orbit. If a binary is located in an environment where the mean stellar mass is $\bar{m}$ and the velocity dispersion is σ, then we call the binary *hard* if $|E_{\rm bin}| \gg \bar{m}\sigma^2$, *soft* if $|E_{\rm bin}| \ll \bar{m}\sigma^2$ and *intermediate* if $|E_{\rm bin}| \sim \bar{m}\sigma^2$.

Their interaction with their environment is given by the Heggie-Hills law: *hard binaries get harder, and soft binaries get softer with time* (Heggie 1975; Hills 1975). What this means is that a hard binary will decrease (on average) its internal energy on each interaction. For instance, if a single star approaches, the perturber star will absorb kinetic energy from the binary and it will leave the interaction with a higher velocity than it approached. The opposite happens to soft binaries that gain internal energy as they interact, eventually becoming positive and the binary is dissolved. An approaching perturber will give kinetic energy to the binary and so, it will leave the interaction with a smaller velocity. There is no rule for intermediate stars, and only numerical simulations can determine their individual behaviour in a given environment.

In general, energy exchanged for hardening a binary is much bigger than when a binary is softened (or disrupted). Therefore, in star clusters, binaries behave like sources of energy that can prevent the collapse of the internal, central, dense "core" regions of star clusters, thus keeping their central densities relatively flat (see, e.g., Chatterjee et al. 2013).

References

Aarseth, S. J. (2003). *Gravitational N-Body Simulations*, p. 430.

Bate, M. R. (2009). *Stellar, brown dwarf and multiple star properties from hydrodynamical simulations of star cluster formation*. MNRAS 392, pp. 590–616.

Binney, J. and Tremaine, S. (1987). *Galactic dynamics*. Princeton, NJ, Princeton University Press, 1987, 747 p.

Bressert, E., Bastian, N., Gutermuth, R., Megeath, S. T., Allen, L., Evans II, N. J., Rebull, L. M., Hatchell, J., Johnstone, D., Bourke, T. L., Cieza, L. A., Harvey, P. M., Merin, B., Ray, T. P., and Tothill, N. F. H. (2010). *The spatial distribution of star formation in the solar neighbourhood: do all stars form in dense clusters?* MNRAS 409, pp. L54–L58.

Chabrier, G. (2003). *Galactic Stellar and Substellar Initial Mass Function*. PASP 115, pp. 763–795.

Chatterjee, S., Umbreit, S., Fregeau, J. M., and Rasio, F. A. (2013). *Understanding the dynamical state of globular clusters: core-collapsed versus non-core-collapsed*. MNRAS 429, pp. 2881–2893.

Dale, J. E., Ercolano, B., and Bonnell, I. A. (2015). *Early evolution of embedded clusters*. MNRAS 451, pp. 987–1003.

Elmegreen, B. G. (2000). *Star Formation in a Crossing Time*. ApJ 530, pp. 277–281.

Elmegreen, B. G. (2007). *On the Rapid Collapse and Evolution of Molecular Clouds*. ApJ 668, pp. 1064–1082.

Farias, J. P., Fellhauer, M., Smith, R., Dominguez, R., and Dabringhausen, J. (2018). *Gas expulsion in highly substructured embedded star clusters*. MNRAS.

Gavagnin, E., Bleuler, A., Rosdahl, J., and Teyssier, R. (2017). *Star cluster formation in a turbulent molecular cloud self-regulated by photoionization feedback*. MNRAS 472, pp. 4155–4172.

Girichidis, P., Federrath, C., Allison, R., Banerjee, R., and Klessen, R. S. (2012). *Importance of the initial conditions for star formation - III. Statistical properties of embedded protostellar clusters*. MNRAS 420, pp. 3264–3280.

Gutermuth, R. A., Megeath, S. T., Myers, P. C., Allen, L. E., Pipher, J. L., and Fazio, G. G. (2009). *A Spitzer Survey of Young Stellar Clusters Within One Kiloparsec of the Sun: Cluster Core Extraction and Basic Structural Analysis*. ApJS 184, pp. 18–83.

Hartmann, L. and Burkert, A. (2007). *On the Structure of the Orion A Cloud and the Formation of the Orion Nebula Cluster*. ApJ 654, pp. 988–997.

Heggie, D. C. (1975). *Binary evolution in stellar dynamics*. MNRAS 173, pp. 729–787.

Heggie, D. and Hut, P. (2003). *The Gravitational Million-Body Problem: A Multidisciplinary Approach to Star Cluster Dynamics*.

Hills, J. G. (1975). *Encounters between binary and single stars and their effect on the dynamical evolution of stellar systems*. AJ 80, pp. 809–825.

Kroupa, P. (2001). *On the variation of the initial mass function*. MNRAS 322, pp. 231–246.

Kroupa, P., Tout, C. A., and Gilmore, G. (1990). *The low-luminosity stellar mass function*. MNRAS 244, pp. 76–85.

Lada, C. J. and Lada, E. A. (2003). *Embedded Clusters in Molecular Clouds*. ARA&A 41, pp. 57–115.

Miller, G. E. and Scalo, J. M. (1979). *The initial mass function and stellar birthrate in the solar neighborhood*. ApJS 41, pp. 513–547.

Nakamura, F. and Li, Z.-Y. (2007). *Protostellar Turbulence Driven by Collimated Outflows*. ApJ 662, pp. 395–412.

Nakamura, F. and Li, Z.-Y. (2014). *Confronting the Outflow-regulated Cluster Formation Model with Observations*. ApJ 783, 115, p. 115.

Salpeter, E. E. (1955). *The Luminosity Function and Stellar Evolution.* ApJ 121, p. 161.

Tan, J. C., Krumholz, M. R., and McKee, C. F. (2006). *Equilibrium Star Cluster Formation*. ApJ 641, pp. L121–L124.

Wu, B., Tan, J. C., Christie, D., Nakamura, F., Van Loo, S., and Collins, D. (2017). *GMC Collisions as Triggers of Star Formation. III. Density and Magnetically Regulated Star Formation*. ApJ 841, 88, p. 88.

Chapter 2

The Birth and Death of Star Clusters

While it is generally agreed that the majority of stars form in clusters instead of in an isolated, dispersed manner (e.g. Bressert et al. 2010; Gutermuth et al. 2009; Lada and Lada 2003), there is no general consensus for how this comes about. It is also agreed from the above studies that most young clusters dissolve into the Galactic field population fairly quickly, or, more accurately, most of their stars become unbound from the cluster, leaving behind a much smaller remnant bound central core.

In this thesis we are addressing the question of how the physics of star formation affects the dynamical evolution of young star clusters during their formation, as well as in their later evolution. While we are focused on stellar dynamics, the evolution of star clusters involves a set of physical process that rise and fall in relevance during the cluster's life. In this chapter we overview the life cycle of a star cluster and the physics involved at each stage. We discuss the relevant metrics that are outcomes of star formation, which have potential consequences for the long term evolution of star clusters.

2.1 Molecular clouds

Most star clusters form from the densest parts of Giant Molecular Clouds (GMCs) (McKee and Ostriker 2007), which are defined to have masses $> 10^4\,\mathrm{M}_\odot$. They are also observed to have mass surface densities $\Sigma \sim 0.01\,\mathrm{g\ cm^{-2}}$ (see Figure 2.1). Star clusters are formed within ~ 1 to 10 parsec structures, termed star-forming *clumps*. Within clumps, star-forming *cores* host the formation of individual stars or small multiple systems, such as binaries.

Overall, most GMCs appear to be gravitationally bound (McKee and Ostriker 2007; Tan et al. 2013). This is likely to be true for star-forming clumps also, including those traced as Infrared Dark Clouds (Kainulainen and Tan 2013). The stability of clumps is a competition between gravity and several internal pressures such as thermal, magnetic, as well as turbulent stochastic motions. However, the relative importance of magnetic fields and turbulence is still a matter of intense debate, in part because of the difficulty of accurately measuring magnetic

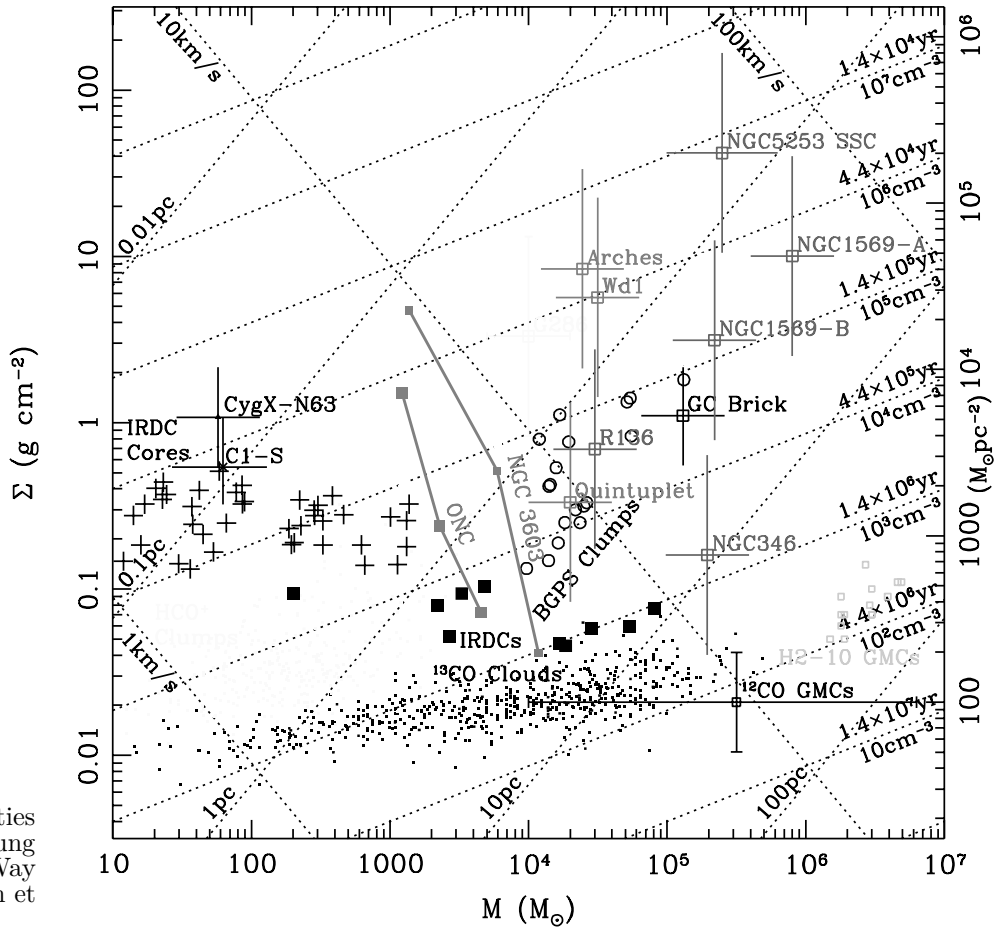

Figure 2.1: Physical properties of star forming clouds and young star clusters in the Milky Way and nearby galaxies (from Tan et al. 2014)

field strengths in molecular clouds (see, e.g., Li et al. 2014a; Pillai et al. 2015). Cores within clumps need to become dense enough to become gravitationally unstable and undergo star formation. However, when gas is adiabatically compressed thermal pressure increases stopping the collapse. It is necessary that gas is also able to cool down. This is possible due to the fact that molecular clouds contain several efficient cooling mechanisms, including dust and different molecular species, especially CO, that are able to emit energy in the form of radiation. The amount of energy radiated will depend on the internal chemical structure of the gas, but in general the equilibrium between cooling and external pressures causes local overdensities to become dense in approximate isothermal equilibrium. Only when the gas reaches very high densities, at number densities of $n(\mathrm{H_2}) > 10^{10}\,\mathrm{cm^{-3}}$ (Mac Low and Klessen 2004), does it become opaque to cooling radiation so that it starts behaving adiabatically. At this point, thermal pressure starts to support the core against gravity and formation of a "first hydrostatic core" as the first stage of star formation takes place.

2.2 Star cluster formation

As soon as a protostar forms it is also acting gravitationally with surrounding sources. It is in this stage that stellar dynamics starts to become important and the outcome of individual star formation affects the early evolution of the embedded star cluster. Star-forming cores can fragment and form binaries or small systems. Binaries are extremely important as they

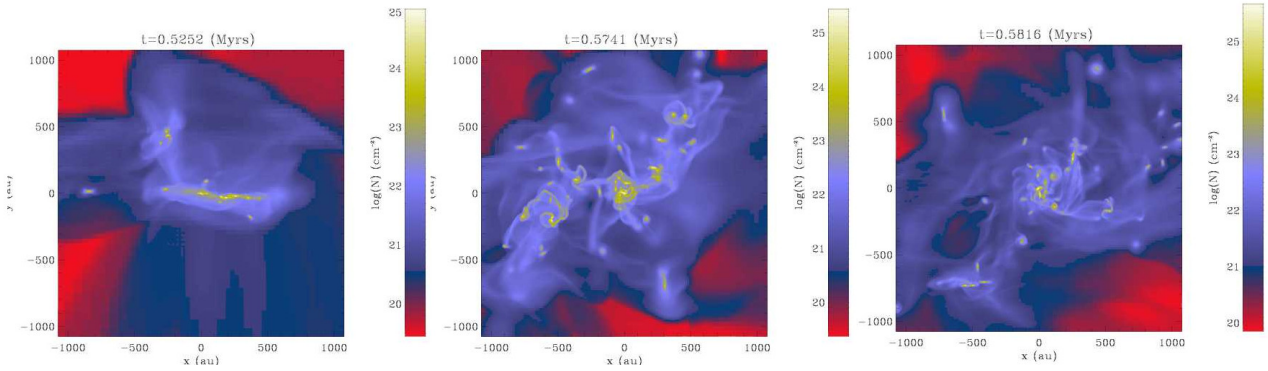

Figure 2.2: An example of fragmentation on a magneto-hydrodynamical simulation of the collapse of a turbulent magnetized cloud (from Hennebelle et al. 2011).

can store large amounts of energy in their orbits. They can either absorb or release energy into the environment depending on if they are hard or soft binaries (Heggie 1975; Hills 1975) (see Section 1.2). Observations shows that a large fraction of stars in the field are binary systems (Duquennoy and Mayor 1991; Fischer and Marcy 1992). However, the dynamical formation of binaries by capture is very inefficient, and the majority of observed binaries must have been formed initially as binaries (Goodman and Hut 1993; Goodwin 2010), i.e., as "primordial binaries" formed from a core. Binaries and small systems are formed through core fragmentation (Goodwin et al. 2007). Fragmentation happens in several modes, e.g., disk fragmentation and turbulent fragmentation, and depends on several factors such as the equation of state of the gas, the strength of magnetic fields, the amount of angular momentum, etc. The general idea is that as a core collapses it increases its rotation velocity by conservation of angular momentum and instabilities within the core cause it to fragment. However, magnetic fields can efficiently transport angular momentum (Li et al. 2014b), so the question of rotational evolution and disk formation is still debated.

An important outcome of star formation is the initial mass function of stars (IMF). The IMF has been shown to be quite invariant on a variety of environments, and its actual universality under debate (see Bastian et al. 2010). Stars of different masses can interact with other stars causing some of them to leave the cluster at high speeds, e.g. two stars can form a binary system and the excess of energy is loss ejecting a third star. This effect is suppressed for instance, if all stars had the same mass (see Pfalzner and Kaczmarek 2013).

Dynamical ejections can be particularly important during the early phases of star cluster formation and evolution. Star clusters are generally at their densest in these stages. Other factors are important for the relative numbers and energetic of ejected stars, such as multiplicity and mass segregation (Oh and Kroupa 2016). Both of these are potentially dependent on the star formation process, i.e., can have "primordial" values. However both can also be modified during the evolution of the cluster.

In the case of mass segregation, it has been argued that massive stars need higher densities and gas rich environments to form, and therefore should be born in the central areas of molecular clumps (Bonnell et al. 2001). However mass segregation can also develop dynamically, since more massive stars are more affected by dynamical friction than low-mass stars, so that they decay to the center of star clusters naturally. In fact, it has been shown that mass segregation timescales are quite short, and distinguishing between primordial or developed mass segregation is a very difficult task. While some efforts have been made to distinguish between primordial

or developed mass segregation (e.g. Baumgardt et al. 2008; Moeckel and Bonnell 2009; Parker et al. 2015) unfortunately most of these studies assumed that all stars are formed instantly and thus ignore the crucial star cluster formation stage.

It is also uncertain what are the primordial properties of binaries, as well as their initial fractions. If wide binaries are formed, then they are likely to be destroyed during the dense, early phase. However they can also form dynamically during the later expansion of the cluster(e.g. Kouwenhoven et al. 2010), in the stage discussed in the next section. Most of what we know about binary populations comes from observations of binaries in the field, i.e., when any dynamical processing is finished.

After stars are formed, they can be kept in a dense state by the background gas that is still present. Star formation is a highly inefficient process and only 20% to 50% of the initial gas is observed to be transformed into stars, at least in local young clusters in the Milky Way (Lada and Lada 2003). It is uncertain how long the residual gas stays within star cluster boundaries. However, while it is present it can be an important contribution to the potential well of the star cluster, and thus keep stars in a dense environment with high velocity dispersions.

When the first massive stars are born they can dissipate the surrounding gas via radiation pressures, ionization and strong stellar winds. Gas will start to dissipate and ultimately, the first supernovae explosion may remove any remaining gas from the cluster.

2.3 Surviving gas expulsion

After the gas is gone, the evolution of the star cluster is only determined by the gravitational interaction of its members, together with stellar evolution processes, which include some gas removal from stars, e.g., by winds. However, the transition from an embedded star cluster to naked bound entity is thought to be a violent process that might disperse most of young star clusters. The low global star formation efficiencies implies that the gas not used by star formation will be the main component of the potential well that keep the cluster bound. The violent removal of the gas results in that most of the stars suddenly having higher velocities than the escape velocity and therefore they leave the system. In the classical picture of this scenario, the only way for star clusters to remain bound is having relatively high SFE ($> 20\%$) or removing the gas on timescales much greater than their crossing time (Baumgardt and Kroupa 2007).

However, recent studies have shown that this transition may not be as destructive as originally thought. Many of the assumptions on star cluster formation that these classical models use are far from reality, and in fact these assumptions have a great influence on the survival and early evolution of star clusters.

Star clusters are likely to be out of equilibrium at formation, e.g., either sub- or super-virial. Then, they need time to reach equilibrium and relevant global parameters oscillate during several crossing times. The result is that survival rate, if gas expulsion is explosive, will depend on how these parameters end up when gas is expelled. The two relevant parameters are the stellar mas to gas fraction the central regions of the cluster, e.g. within the half mass radius, and the stellar virial ratio, both measured when gas expulsion beings.

The central stellar fraction may also be an outcome of star cluster formation. Star formation may happen faster in densest parts of the star forming clump where the free-fall time is shorter (Parmentier and Pfalzner 2013). Furthermore, stars do not form in spherical distributions.

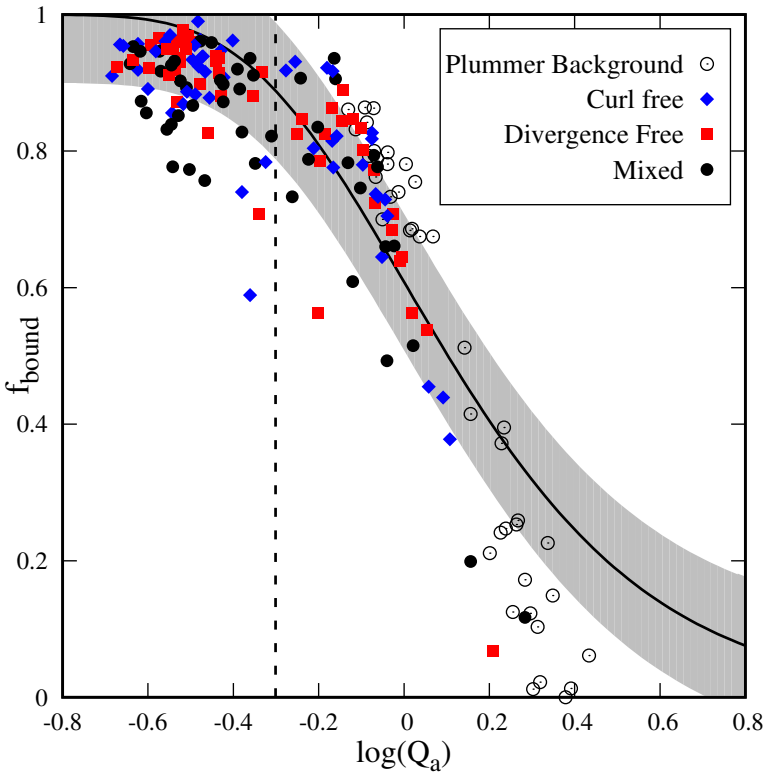

Figure 2.3: The bound fraction as a function of stellar virial ratio at gas expulsion time for star clusters with different levels of stellar and gaseous structure and SFE of 20% (from Farias et al. 2018).

Star forming clumps usually show filamentary structures on several scales. It has been shown that just by the introduction of substructure in numerical simulations, there is an increase in the central stellar fraction considerably via merging of substructures (Farias et al. 2015; Smith et al. 2011, 2013).

Most importantly, is has been shown that the stellar virial ratio at the time of final gas expulsion is the only necessary parameter to estimate the minimum amount of mass that a star cluster will retain (Lee and Goodwin 2016), even in the most complex stellar and gaseous distributions (Farias et al. 2018), as can be seen in Figure 2.3.

2.4 Gas-free evolution

Even if a star cluster survives gas expulsion, the process will likely expand it considerably. It is important that the cluster remain dense after gas expulsion so its internal binding energy is large. If is not dense enough it could be easily destroyed by tidal forces from nearby molecular clouds and/or from the host galaxy.

In the best scenario, if the star cluster remains dense after emerging from its parent clump, internal dynamical processing may also expand the cluster. Star clusters are collisional systems, which means that close encounters between stars determine the internal evolution and structure of the entity. Strong dynamical interactions between stars, especially multiples, typically end up in one or more stars being ejected with high velocities. High densities enhance these interactions in energy and frequency, therefore they are most likely to happen in the center of the cluster. These ejections remove binding energy from the cluster in the form of kinetic energy of the ejected stars and therefore the cluster expands. The timescale at which a star cluster *evaporates* completely is $\sim 100 t_{\rm relax} \approx (10N/\log N) t_{\rm cross}$ (Binney and Tremaine 1987).

For a small star cluster of 100 members, this means $1000t_{\rm cross}$ which is in general a relatively long timescale, especially compared to expected formation timescales.

At this stage, the most massive stars have already exploded as supernovae – and may have been the ones that removed any residual gas from the cluster – but at later stages, the mass loss from other intermediate- and lower-mass stars starts to play a role in the evolution of the star cluster. Stellar evolution becomes a secondary source of dynamical ejections. If one of the stars that explode as a supernova happens to be a binary system, the sudden mass loss will modify the binary orbit and it could even cause the ejection of both stars in opposite directions. Even the remnants of single massive stars can be ejected spontaneously when exploding as supernovae, since these explosions are not necessarily symmetrical and the supernovae remnant (neutron star or black hole) can be ejected in a random direction at very high speeds, i.e., a few hundred km/s.

Thus, once a star cluster is born its subsequent evolution will depend on its environment and the ability of the cluster to remain dense. Clusters will tend to keep losing mass by stellar evolution, dynamical evaporation and tidal stripping.

We have briefly overviewed the life cycle of star clusters and the physics involved. We have seen that the evolution and survivability is the combination and interplay of several physical processes. However, most of the factors that determine the dynamical evolution of star clusters are determined by the physics and the outcome of star formation. Many theories exist on how stars are formed and there is a long standing debate on what the outcome of star formation is and how star clusters are born. All these different theories have direct and indirect implications in the evolution of star clusters and in this thesis we will explore some of them. We will aim to identify the observables that could constrain some of these theories using a statistical approach.

References

Bastian, N., Covey, K. R., and Meyer, M. R. (2010). *A Universal Stellar Initial Mass Function? A Critical Look at Variations*. ARA&A 48, pp. 339–389.

Baumgardt, H., De Marchi, G., and Kroupa, P. (2008). *Evidence for Primordial Mass Segregation in Globular Clusters*. ApJ 685, 247-253, pp. 247–253.

Baumgardt, H. and Kroupa, P. (2007). *A comprehensive set of simulations studying the influence of gas expulsion on star cluster evolution*. MNRAS 380, pp. 1589–1598.

Binney, J. and Tremaine, S. (1987). *Galactic dynamics*. Princeton, NJ, Princeton University Press, 1987, 747 p.

Bonnell, I. A., Bate, M. R., Clarke, C. J., and Pringle, J. E. (2001). *Competitive accretion in embedded stellar clusters*. MNRAS 323, pp. 785–794.

Bressert, E., Bastian, N., Gutermuth, R., Megeath, S. T., Allen, L., Evans II, N. J., Rebull, L. M., Hatchell, J., Johnstone, D., Bourke, T. L., Cieza, L. A., Harvey, P. M., Merin, B., Ray, T. P., and Tothill, N. F. H. (2010). *The spatial distribution of star formation in the solar neighbourhood: do all stars form in dense clusters?* MNRAS 409, pp. L54–L58.

Duquennoy, A. and Mayor, M. (1991). *Multiplicity among solar-type stars in the solar neighbourhood. II - Distribution of the orbital elements in an unbiased sample*. A&A 248, pp. 485–524.

Farias, J. P., Fellhauer, M., Smith, R., Dominguez, R., and Dabringhausen, J. (2018). *Gas expulsion in highly substructured embedded star clusters*. MNRAS.

Farias, J. P., Smith, R., Fellhauer, M., Goodwin, S., Candlish, G. N., Blaña, M., and Dominguez, R. (2015). *The difficult early stages of embedded star clusters and the importance of the pre-gas expulsion virial ratio*. MNRAS 450, pp. 2451–2458.

Fischer, D. A. and Marcy, G. W. (1992). *Multiplicity among M dwarfs*. ApJ 396, pp. 178–194.

Goodman, J. and Hut, P. (1993). *Binary-single-star scattering. V - Steady state binary distribution in a homogeneous static background of single stars*. ApJ 403, pp. 271–277.

Goodwin, S. P. (2010). *Binaries in star clusters and the origin of the field stellar population*. Philosophical Transactions of the Royal Society of London Series A 368, pp. 851–866.

Goodwin, S. P., Kroupa, P., Goodman, A., and Burkert, A. (2007). *The Fragmentation of Cores and the Initial Binary Population*. Protostars and Planets V, pp. 133–147.

Gutermuth, R. A., Megeath, S. T., Myers, P. C., Allen, L. E., Pipher, J. L., and Fazio, G. G. (2009). *A Spitzer Survey of Young Stellar Clusters Within One Kiloparsec of the Sun: Cluster Core Extraction and Basic Structural Analysis*. ApJS 184, pp. 18–83.

Heggie, D. C. (1975). *Binary evolution in stellar dynamics*. MNRAS 173, pp. 729–787.

Hennebelle, P., Commerçon, B., Joos, M., Klessen, R. S., Krumholz, M., Tan, J. C., and Teyssier, R. (2011). *Collapse, outflows and fragmentation of massive, turbulent and magnetized prestellar barotropic cores*. A&A 528, A72, A72.

Hills, J. G. (1975). *Encounters between binary and single stars and their effect on the dynamical evolution of stellar systems*. AJ 80, pp. 809–825.

Kainulainen, J. and Tan, J. C. (2013). *High-dynamic-range extinction mapping of infrared dark clouds. Dependence of density variance with sonic Mach number in molecular clouds*. A&A 549, A53, A53.

Kouwenhoven, M. B. N., Goodwin, S. P., Parker, R. J., Davies, M. B., Malmberg, D., and Kroupa, P. (2010). *The formation of very wide binaries during the star cluster dissolution phase*. MNRAS 404, pp. 1835–1848.

Lada, C. J. and Lada, E. A. (2003). *Embedded Clusters in Molecular Clouds*. ARA&A 41, pp. 57–115.

Lee, P. L. and Goodwin, S. P. (2016). *Surviving gas expulsion with substructure*. MNRAS 460, pp. 2997–3001.

Li, H.-B., Goodman, A., Sridharan, T. K., Houde, M., Li, Z.-Y., Novak, G., and Tang, K. S. (2014a). *The Link Between Magnetic Fields and Cloud/Star Formation*. Protostars and Planets VI, pp. 101–123.

Li, Z.-Y., Banerjee, R., Pudritz, R. E., Jørgensen, J. K., Shang, H., Krasnopolsky, R., and Maury, A. (2014b). *The Earliest Stages of Star and Planet Formation: Core Collapse, and the Formation of Disks and Outflows*. Protostars and Planets VI, pp. 173–194.

Mac Low, M.-M. and Klessen, R. S. (2004). *Control of star formation by supersonic turbulence*. Reviews of Modern Physics 76, pp. 125–194.

McKee, C. F. and Ostriker, E. C. (2007). *Theory of Star Formation*. ARA&A 45, pp. 565–687.

Moeckel, N. and Bonnell, I. A. (2009). *Limits on initial mass segregation in young clusters*. MNRAS 396, pp. 1864–1874.

Oh, S. and Kroupa, P. (2016). *Dynamical ejections of massive stars from young star clusters under diverse initial conditions*. A&A 590, A107, A107.

Parker, R. J., Dale, J. E., and Ercolano, B. (2015). *Primordial mass segregation in simulations of star formation?* MNRAS 446, pp. 4278–4290.

Parmentier, G. and Pfalzner, S. (2013). *Local-density-driven clustered star formation*. A&A 549, A132, A132.

Pfalzner, S. and Kaczmarek, T. (2013). *Reaction of massive clusters to gas expulsion - The cluster density dependence*. A&A 555, A135, A135.

Pillai, T., Kauffmann, J., Tan, J. C., Goldsmith, P. F., Carey, S. J., and Menten, K. M. (2015). *Magnetic Fields in High-mass Infrared Dark Clouds*. ApJ 799, 74, p. 74.

Smith, R., Fellhauer, M., Goodwin, S., and Assmann, P. (2011). *Surviving infant mortality in the hierarchical merging scenario*. MNRAS 414, pp. 3036–3043.

Smith, R., Sánchez-Janssen, R., Fellhauer, M., Puzia, T. H., Aguerri, J. A. L., and Farias, J. P. (2013). *The impact of galaxy harassment on the globular cluster systems of early-type cluster dwarf galaxies*. MNRAS 429, pp. 1066–1079.

Tan, J. C., Beltrán, M. T., Caselli, P., Fontani, F., Fuente, A., Krumholz, M. R., McKee, C. F., and Stolte, A. (2014). *Massive Star Formation*. Protostars and Planets VI, pp. 149–172.

Tan, J. C., Shaske, S. N., and Van Loo, S. (2013). *Molecular Clouds: Internal Properties, Turbulence, Star Formation and Feedback. Molecular Gas, Dust, and Star Formation in Galaxies*. Ed. by T. Wong and J. Ott. Vol. 292. IAU Symposium, pp. 19–28.

Chapter 3

Numerical Methods

3.1 The N-body Code: `Nbody6`

In this thesis aim to follow accurately the dynamical evolution of star clusters over millions of years, mainly focussing on the gravitational interaction between their members. This treatment includes an accurate modeling of stellar binaries with a wide range of period distributions, including periods as short as ~ 1 day. This achievement is enabled by use of the `Nbody6++` (Wang et al. 2015), a multiprocessor optimized version of the extensively developed code `Nbody6`, the first version of which is almost 50 years old, and which is still under active development. Here we will briefly describe its main features, as well as the modification done by ourselves in order to accomplish our goals. A complete description of the code can be found in Aarseth (2003).

`Nbody6` is a sixth order Hermite integrator that calculates the forces between the particles directly with no approximations. The resulting acceleration vector of the forces acting on a given particle i by the rest of the $N-1$ particles is given by:

$$\ddot{\mathbf{r}}_i \;=\; \sum_{\mathrm{j}\neq\mathrm{i}} \frac{Gm_{\mathrm{j}}(\mathbf{r}_{\mathrm{i}}-\mathbf{r}_{\mathrm{j}})}{|\mathbf{r}_{\mathrm{i}}-\mathbf{r}_{\mathrm{j}}|^3}, \tag{3.1}$$

where m_j is the mass of the jth particle and $\mathbf{r}$ is the position. The equations of motion given by equation 3.1 need to be solved for each particle. Therefore there are $3N$ differential equations to be solved. For $N \leq 3$ it is possible to be done analytically, however for greater numbers is only possible to do numerically. There are multiple numerical schemes to solve equation 3.1, from which `Nbody6` uses the Hermite scheme, which solves the equations of motion using a Taylor expansion series up to 4th order. Here we briefly describe the scheme.

3.1.1 Hermite Scheme

In the Hermite scheme, accelerations $\mathbf{a}_0$ are given explicitly by equation 3.1 and their derivatives $\dot{\mathbf{a}}_0$ are calculated by:

$$\dot{\mathbf{a}}_0 = \sum_{\mathrm{j}\neq\mathrm{i}} Gm_\mathrm{j}\left[\frac{\mathbf{V}_\mathrm{ij}}{R_\mathrm{ij}^3} - \frac{3(\mathbf{V}_\mathrm{ij}\cdot\mathbf{R}_\mathrm{ij})\mathbf{R}_\mathrm{ij}}{R_\mathrm{ij}^5}\right] , \tag{3.2}$$

where G is the gravitational constant, $\mathbf{R}_\mathrm{ij} = \mathbf{r}_\mathrm{i} - \mathbf{r}_\mathrm{j}$, $\mathbf{V}_\mathrm{ij} = \mathbf{v}_\mathrm{i} - \mathbf{v}_\mathrm{j}$, $R_\mathrm{ij} = |\mathbf{R}_\mathrm{ij}|$, $V_\mathrm{j} = |\mathbf{V}_\mathrm{j}|$. Then a first (low order) prediction of the position and velocity of the particle i at $t = t_1$ is calculated (with $t_1 = t_0 + \Delta t$ and Δt as particle timestep) according to:

$$\mathbf{x}_p(t) = \frac{1}{6}(t-t_0)^3\dot{\mathbf{a}}_0 + \frac{1}{2}(t-t_0)^2\mathbf{a}_0 + (t-t_0)\mathbf{v} + \mathbf{x} , \tag{3.3}$$

$$\mathbf{v}_p(t) = \frac{1}{2}(t-t_0)^2\dot{\mathbf{a}}_0 + (t-t_0)\mathbf{a}_0 + \mathbf{v} , \tag{3.4}$$

where the subscript p stands for "predicted". This is done for all particles in the cluster. Thus, using again equations 3.1 and 3.2 with the new positions of the particles we obtain the accelerations and their derivatives at $t = t_1$ denoted $\mathbf{a}_1$ and $\dot{\mathbf{a}}_1$. However, $\mathbf{a}_1$ and $\dot{\mathbf{a}}_1$ can also be obtained using the Taylor series with higher derivatives of $\mathbf{a}$ at $t = t_0$:

$$\mathbf{a}_1 = \frac{1}{6}(t-t_0)^3\mathbf{a}_0^{(3)} + \frac{1}{2}(t-t_0)^2\mathbf{a}_0^{(2)} + (t-t_0)\dot{\mathbf{a}}_0 + \mathbf{a_0} , \tag{3.5}$$

$$\dot{\mathbf{a}}_1 = \frac{1}{2}(t-t_0)^2\mathbf{a}_0^{(3)} + (t-t_0)\mathbf{a}_0^{(2)} + \dot{\mathbf{a}}_0 . \tag{3.6}$$

Now, since we already know $\mathbf{a}_1$ and $\dot{\mathbf{a}}_1$ from the low order prediction, we can use that result to obtain the higher derivatives of $\mathbf{a}$, at $t = t_0$, i.e., $\mathbf{a}^{(2)}$ and $\mathbf{a}^{(3)}$:

$$\frac{1}{2}\mathbf{a}^{(2)} = -3\frac{\mathbf{a}_0 - \mathbf{a}_1}{(t-t_0)^2} - \frac{2\dot{\mathbf{a}}_0 + \dot{\mathbf{a}}_1}{(t-t_0)} \tag{3.7}$$

$$\frac{1}{6}\mathbf{a}^{(3)} = 2\frac{\mathbf{a}_0 - \mathbf{a}_1}{(t-t_0)^3} - \frac{\dot{\mathbf{a}}_0 + \dot{\mathbf{a}}_1}{(t-t_0)^2} . \tag{3.8}$$

The Hermite interpolation then finishes the timestep correcting the low order prediction of the positions and velocities to a higher order:

$$\mathbf{x}(t) = \mathbf{x}_p(t) + \frac{1}{24}(t-t_0)^4\mathbf{a}_0^{(2)} + \frac{1}{120}(t-t_0)^5\mathbf{a}^{(3)} , \tag{3.9}$$

$$\mathbf{v}(t) = \mathbf{v}_p(t) + \frac{1}{6}(t-t_0)^3\mathbf{a}_0^{(2)} + \frac{1}{24}(t-t_0)^4\mathbf{a}_0^{(3)} . \tag{3.10}$$

3.1.2 Block Timestep Scheme

Particles in the system feel very different accelerations and the timestep needed to accurately follow their motion depends on the strength of the acceleration. Therefore, individual timesteps are needed. `Nbody6` uses the *block timestep scheme* in which timesteps are sorted into a hierarchy of levels starting from a maximum timestep Δt_1 according to the rule:

$$\Delta t_n = \Delta t_1 / 2^{n-1}. \tag{3.11}$$

At the beginning of the calculation a reasonable timestep for each particle is specified. This reasonable timestep has been found by empirical experiments to be (see Aarseth 2003):

$$\Delta t_{\rm i} = \sqrt{\frac{\eta |\mathbf{a}||\mathbf{a}^{(2)}| + |\dot{\mathbf{a}}|^2}{|\dot{\mathbf{a}}||\mathbf{a}^{(3)}| + |\mathbf{a}^{(2)}|^2}}, \tag{3.12}$$

where η is a free parameter, which by experience is usually taken to be in the range $\eta = 0.01 - 0.04$. Then the nearest level is chosen according to Eq. 3.11. At any general time Eq. 3.11 is evaluated and any of these three cases apply when comparing with the previous timestep Δt_p: If $\Delta t_p > \Delta t_{\rm i}$ then the timestep is reduced by a factor of 2; if $2\Delta t_p < \Delta t_{\rm i}$ the timestep is increased by factor 2; otherwise there is no change. A detailed discussion about the implementation and special situations can be found in Aarseth (2003).

3.1.3 Neighbour scheme

In order to save computational time, the code adopts the Ahmad-Cohen neighbour scheme (Ahmad and Cohen 1973; Makino and Aarseth 1992). The basic idea is that the contribution to the acceleration given by distant particles does not need to be updated as frequently as close *neighbour* particles. As a difference of similar approaches like the Tree scheme (Barnes and Hut 1986), where the calculation of distant particles is done using their center of mass, in the neighbour scheme the forces are still calculated individually and therefore the method is not an approximation, but rather an optimization. The optimization is based on the fact that distant particles have smaller angular speeds and their force contribution does not change so fast as neighbouring particles.

3.1.4 Regularizations

Even with only single particles, the methods described above are not enough to efficiently handle all the length and time scales involved in the evolution of a realistic star cluster. However, the main problems are caused by binary systems with very short periods, on the order of days, that will likely keep their short separation during the whole duration of the calculation. In addition, small stable multiple systems, normally composed of a binary perturbed by another binary or single star, and very close encounters between stars, may slow down the simulations even with individual timesteps and the neighbour scheme. `Nbody6` uses several methods to deal with these special cases called *regularizations*. Close encounters and binaries are handled with the Kustaanheimo-Stiefel (KS) regularization (Kustaanheimo and Stiefel 1965), which uses a coordinate transformation in order to avoid singularities. The KS scheme has been expanded to the isolated and perturbed 3- (Aarseth et al. 1974) and 4-body problem as well as higher order hierarchies (Mikkola 1997; Mikkola and Aarseth 1990, 1993, 1996, 1998).

3.1.5 Gradual formation

In this thesis we study star cluster formation from the beginning, this is, during the stage of the cluster where stars are being created. Unfortunately, this is a feature not currently implemented in `Nbody6`. However, during a regular `Nbody6` run, particles are being created and removed all the time. Each time regularization starts, the particles involved in the regularization are removed from the calculation and replaced by a center of mass particle that interacts with

the rest of the cluster, while the regularized particles are integrated in isolation. Also, high velocity escapers are normally removed entirely from the calculation. Therefore, there is no reason that stop us from adding particles arbitrarily during the run-time. Through careful investigation of the code, we have introduced our own routines in order to achieve this feature. We are able couple a time evolving background gas potential with the creation of single and KS regularized binaries until the gas is exhausted.

This feature then enables us to study a regime only explored so far by state-of-the-art hybrid N-boody/hydrodynamical codes. However, because of the complexity of the N-body problem, these codes normally have not implemented regularizations of binaries or higher-order multiples. Also, they normally use approximations like the Tree scheme (Barnes and Hut 1986). We expect that the important feature we have developed, allowing gradual star formation, can enable `Nbody6` to be coupled with hydrodynamical codes in frameworks like the Astrophysical Multipurpose Software Envirionment (AMUSE) (Pelupessy et al. 2013; Portegies Zwart et al. 2013). Still, coupling `Nbody6` with hydro codes would be computationally expensive, and the pure N-body approach presented here, is the first necessary step to obtain a general statistical understanding of stellar dynamics during star cluster formation.

References

Aarseth, S. J. (2003). *Gravitational N-Body Simulations*, p. 430.

Aarseth, S. J., Henon, M., and Wielen, R. (1974). *A comparison of numerical methods for the study of star cluster dynamics*. A&A 37, pp. 183–187.

Ahmad, A. and Cohen, L. (1973). *A numerical integration scheme for the N-body gravitational problem*. Journal of Computational Physics 12, pp. 389–402.

Barnes, J. and Hut, P. (1986). *A hierarchical O(N log N) force-calculation algorithm*. Nature 324, pp. 446–449.

Kustaanheimo, P. and Stiefel, E. (1965). *Perturbation Theory of Kepler Motion based on Spinor Regularization*. Journal Fur Die Reine Und Angewandte Mathematik 218, pp. 204–219.

Makino, J. and Aarseth, S. J. (1992). *On a Hermite integrator with Ahmad-Cohen scheme for gravitational many-body problems*. PASJ 44, pp. 141–151.

Mikkola, S. (1997). *Numerical Treatment of Small Stellar Systems with Binaries*. Celestial Mechanics and Dynamical Astronomy 68, pp. 87–104.

Mikkola, S. and Aarseth, S. J. (1990). *A chain regularization method for the few-body problem*. Celestial Mechanics and Dynamical Astronomy 47, pp. 375–390.

Mikkola, S. and Aarseth, S. J. (1993). *An implementation of N-body chain regularization*. Celestial Mechanics and Dynamical Astronomy 57, pp. 439–459.

Mikkola, S. and Aarseth, S. J. (1996). *A Slow-down Treatment for Close Binaries*. Celestial Mechanics and Dynamical Astronomy 64, pp. 197–208.

Mikkola, S. and Aarseth, S. J. (1998). *An efficient integration method for binaries in N-body simulations*. 3, pp. 309–320.

Pelupessy, F. I., van Elteren, A., de Vries, N., McMillan, S. L. W., Drost, N., and Portegies Zwart, S. F. (2013). *The Astrophysical Multipurpose Software Environment*. A&A 557, A84, A84.

Portegies Zwart, S., McMillan, S. L. W., van Elteren, E., Pelupessy, I., and de Vries, N. (2013). *Multi-physics simulations using a hierarchical interchangeable software interface*. Computer Physics Communications 183, pp. 456–468.

Wang, L., Spurzem, R., Aarseth, S., Nitadori, K., Berczik, P., Kouwenhoven, M. B. N., and Naab, T. (2015). *NBODY6++GPU: ready for the gravitational million-body problem.* MNRAS 450, pp. 4070–4080.

Chapter 4

Introduction to papers

In this thesis, we wish to test the effects of several parameters of star cluster formation theories, such as initial mass surface densities of the gas clumps, the frequency of the primordial binary population, the degree of primordial mass segregation, and, of particular importance, the timescale of star cluster formation. We have developed novel techniques in order to model star cluster formation, while accurately following stellar dynamics. One important population of stars that could help us to understand star cluster formation is the population of ejected stars. While we follow the global evolution and structure of the bound cluster, the former quickly erases its initial state and rearranges in an equilibrium configuration. However, ejected stars only lose some energy as they leave the potential well of the cluster. Therefore, it is important to understand their formation, since it give us clues about the environment in which they were ejected. In this thesis, we present two independent, but closely related, works. First, we present, in two papers (the second of which is in preparation for submission) the star cluster formation model that we use in our main work, as well as it implications. Then, we present a study that analyzes how a particular observed runaway system in the Orion Nebula Cluster may have been created by exploring the parameter space of possible binary-binary interactions. This is an example of how observed runaway systems, many more of which are expected to be found by the *GAIA* mission, can be modeled to understand their launching mechanism.

Star Cluster Formation from Turbulent Clumps. I. The fast formation limit

In this paper, we set the basis for our overall project of cluster formation modeling. We present a simple form of the model in the extreme limit of fast, i.e., instantaneous, star cluster formation. Even though this model appears unrealistic, it has been the commonly adopted assumption of most previous dynamical studies exploring the early evolution of star clusters. Also, most previous studies have used initial conditions in which the stellar population is already in dynamical equilibrium. In contrast, we draw our initial conditions from observations of starless clumps and theory describing their internal structure, i.e., the Turbulent Clump Model, from which we then form star clusters. We found that in this scenario, star clusters

expand very quickly, meaning that in order to explain the current structure and sizes of observed star clusters, dense initial conditions are necessary. Also, the periods that star clusters remain dense are very short (less than a crossing time), thus not giving enough time to produce significant dynamical ejections. In fact, not a single runaway massive star was produced. This work suggests that star cluster formation must happen in a less extreme fashion, that we will explore in the subsequent papers of this series.

Star Cluster Formation from Turbulent Clumps. II. Gradual star cluster formation

In this paper, we relax the assumption of instantaneous star cluster formation explored in Paper I (and in most of studies to date). We explore a range of star cluster formation timescales, parameterized by the star formation efficiency per free-fall time. We model the natal gas of the young cluster using a time evolving background potential, based on the Turbulent Clump Model. As the stars are created, the background potential gradually vanishes assuming a global star formation efficiency. Using this simple prescription, we study the dynamic of the stars during the formation of the cluster, and found that the longer formation timescales give enough time to the cluster to get close to virial equilibrium before gas is completely exhausted/ejected. Star clusters formed in a slow fashion are much more stable against expansion than the ones forming fast. In this models, we are able to form a significant fraction of massive runaway stars even in low density environments. In general, the models presented in this paper, appear to require lower densities to reproduce parameters that could only be explained appealing to highly dense initial environments. However, several assumptions need to be relaxed and studied to understand the real extent of these results.

On the formation of runaway stars BN and x in the Orion Nebula Cluster
Star clusters formed in a slow fashion are much more stable against expansion than the ones forming fast. The Orion Nebula Cluster (ONC) is the closest region of massive star formation. It hosts a massive young star, BN ($\sim 10\,M_\odot$), that is moving with a velocity of ~ 30 km/s in the frame of reference of the ONC. New observations have show that two known nearby objects, source x ($\sim 3\,M_\odot$) and source I ($\sim 7M_\odot$), are moving away from the same location than BN and the three objects may have been part of the same ejection event about 500 years ago. However, this implies that the most massive star in the system was ejected with very high velocity, which seems questionable. We thus performed a large, $> 10^7$, set of "few-body" simulations testing this scenario, and have found that the event as described is nearly impossible to happen with the observed velocities. We conclude that to make this scenario plausible, requires source I to in fact be more massive than the $\sim 7M_\odot$ that has been adopted by some authors in their previous works. This may be possible, since source I is heavily embedded in dusty molecular gas. The results are of wider interest, since this region is the closest example of massive star formation and is one of the most well studied locations of the sky, including one of the richest sites for detection of interstellar molecules. The violent nature of the interaction, including potential gas interactions and shocks, likely has a bearing on why this region appears so luminous in the infrared and is so chemically rich.

Paper *I*

Star Cluster Formation from Turbulent Clumps. I. The Fast Formation Limit.

Juan P. Farias, Jonathan C. Tan & Sourav Chatterjee

Published in The Astrophysical Journal (2017), Volume 838(2), Page 116.

The Astrophysical Journal, 838:116 (23pp), 2017 April 1 https://doi.org/10.3847/1538-4357/aa63f6

Star Cluster Formation from Turbulent Clumps. I. The Fast Formation Limit

Juan P. Farias[1], Jonathan C. Tan[1], and Sourav Chatterjee[2]
[1] Astronomy Department, University of Florida, Gainesville, FL 32611, USA
[2] Center for Interdisciplinary Exploration & Research in Astrophysics (CIERA) Physics & Astronomy, Northwestern University, Evanston, IL 60202, USA; jfarias@ufl.edu
Received 2017 January 2; revised 2017 February 9; accepted 2017 February 27; published 2017 March 31

Abstract

We investigate the formation and early evolution of star clusters, assuming that they form from a turbulent starless clump of a given mass bounded inside a parent self-gravitating molecular cloud characterized by a particular mass surface density. As a first step, we assume instantaneous star cluster formation and gas expulsion. We draw our initial conditions from observed properties of starless clumps. We follow the early evolution of the clusters up to 20 Myr, investigating the effects of different star formation efficiencies, primordial binary fractions and eccentricities, and primordial mass segregation levels. We investigate clumps with initial masses of $M_{\rm cl} = 3000\,M_\odot$ embedded in ambient cloud environments with mass surface densities $\Sigma_{\rm cloud} = 0.1$ and 1 g cm^{-2}. We show that these models of fast star cluster formation result, in the fiducial case, in clusters that expand rapidly, even considering only the bound members. Clusters formed from higher $\Sigma_{\rm cloud}$ environments tend to expand more quickly and thus are soon larger than clusters born from lower $\Sigma_{\rm cloud}$ conditions. To form a young cluster of a given age, stellar mass, and mass surface density, these models need to assume a parent molecular clump that is many times denser, which is unrealistic compared to observed systems. We also show that, in these models, the initial binary properties are only slightly modified by interactions, meaning that the binary properties, e.g., at 20 Myr, are very similar to those at birth. With this study, we set up the foundation for future work, where we will investigate more realistic models of star formation compared to this instantaneous, baseline case.

Key words: galaxies: star clusters: general – galaxies: star formation – methods: numerical

1. Introduction

Most stars tend to form together in clusters (e.g., Gutermuth et al. 2009), which are created from overdense gas clumps typically found in giant molecular clouds (GMCs) (e.g., McKee & Ostriker 2007). Thus, understanding how stars form comes with the direct need to understand how and where star clusters form. It is still a matter of debate whether star cluster formation depends on the properties of the GMC environment. While theoretical studies have taught us the essential physical processes that determine a star cluster's evolution after the gas is dispersed, the transition from the dense star-forming clump to the star cluster that emerges from the gas is not yet well understood (see, e.g., Banerjee & Kroupa 2015 for a review). In particular, it is debated whether the process is slow, with the clump evolving in a quasi-equilibrium state (Tan et al. 2006; Nakamura & Li 2007), or very rapid, with star cluster formation occurring in just a crossing time of the system (Elmegreen 2000, 2007; Hartmann & Burkert 2007).

There are numerous physical processes potentially involved in such a transition from gas clump to star cluster, including fragmentation of a magnetized, turbulent, and self-gravitating medium into a population of pre-stellar cores; collapse of these cores via rotationally supported disks into single- or multiple-star systems; feedback from the forming stars, especially protostellar outflows that can maintain turbulence in the clump (Nakamura & Li 2007, 2014), and, eventually, radiative feedback processes from more massive stars (e.g., Dale et al. 2015); continued infall of gas to the clump; dispersal of clump gas by feedback; and dynamical interactions among the forming and recently formed stars as they orbit in the protocluster potential (e.g., Chatterjee & Tan 2012). This is a complicated, multiscale problem, the full solution of which is beyond current computational capabilities. Thus, approximate models are necessary. By investigating how the outcome of star cluster formation depends on the adopted approximations, we can learn which processes are most important.

Our approach in this paper and subsequent papers in this series is to accurately follow the dynamics of formed stars, including binary properties, via direct *N*-body integrations and to approximate various models for how individual stars are born within the star-forming clump. Our initial conditions are based on the turbulent core/clump model of McKee & Tan (2003, hereafter MT03), which approximates clumps as singular polytropic virialized spheres that are in pressure equilibrium with their surrounding cloud medium. This surrounding cloud is also assumed to be self-gravitating, so its ambient pressure is $\bar{P} \sim G\Sigma^2$, where Σ is the cloud mass surface density—the main variable describing different environmental conditions.

In this first paper, we start with the simplest approximation for star formation, i.e., instantaneous formation of the stellar population from the initial gas clump along with simultaneous, instantaneous expulsion of the remaining gas that is not incorporated into the stars. This approximation has often been adopted by previous *N*-body studies (e.g., Bastian & Goodwin 2006; Parker et al. 2014; Pfalzner et al. 2015). However, in comparison to these previous studies, our work is distinguished by (1) adopting initial conditions that have been explicitly developed for self-gravitating gas clumps (i.e., singular polytropic spheres as approximations for turbulent, magnetized clumps) and (2) following the full evolution of binary systems.

A number of authors have studied the dynamics of binaries in star clusters using numerical models (e.g., Kroupa et al. 1999; Kroupa & Burkert 2001; Parker et al. 2009; Kouwenhoven et al. 2010; Kaczmarek et al. 2011; Parker et al. 2011) focusing on various aspects of their dynamics. In our work, we follow the evolution of binary properties due to stellar interactions and stellar

evolution (SE) in clusters forming in different environments. We use and will use these results to constrain assumptions about the star cluster process (e.g., its duration) and individual star formation processes (e.g., how binaries form), i.e., the primordial binary properties. We also examine the role of binaries in producing dynamical and binary supernova ejections, especially fast runaway stars.

We anticipate that, in reality, star cluster formation is likely to proceed in a relatively gradual manner, i.e., taking at least several and perhaps many local freefall timescales of the gas clump. Modeling this process of gradual star cluster formation will be the topic of the second paper in this series. One aspect that is needed in such a model is the gradual evolution of the potential of the natal gas clump, which can be approximated via a simple analytic relation. The approach of an evolving approximate background gas potential has been adopted previously (e.g., Tutukov 1978; Lada et al. 1984; Geyer & Burkert 2001; Boily & Kroupa 2003; Chen & Ko 2009; Smith et al. 2011; Farias et al. 2015; Brinkmann et al. 2016). However, in all these studies, the full stellar population was introduced instantaneously at the beginning of the simulation. None of these studies included a full treatment of binaries, i.e., including a significant fraction of primordial binaries.

The second aspect is the gradual formation of the stellar population in the cluster. This will be the main focus of Paper II in our series. There have so far been relatively few studies using such an approach. Proszkow & Adams (2009) presented a study involving gradual star formation and the early evolution of young clusters, focusing on low- to intermediate-mass clusters (100–3000 members) without primordial binaries. However, the stellar densities of their models were relatively low, limiting the effects of stellar interactions. They also did not include SE and only simulated up to 10 Myr.

These methods of *N*-body modeling can be contrasted with other approaches to simulating star cluster formation, e.g., simulations that follow the (magneto-)hydrodynamics of the collapsing clump (e.g., Price & Bate 2009; Padoan et al. 2012; Myers et al. 2014; Padoan et al. 2014). Such simulations must still implement subgrid models for how stars form and inject feedback into the gas. Typically, they do not have the resolution to accurately follow binary orbital evolution. Still, these are complementary approaches to those based on pure *N*-body approaches, and comparison of the results of the different methods will be instructive.

2. Pre-cluster Clumps as Initial Conditions

The initial conditions for star clusters are constrained by the observed properties of dense gas clumps within GMCs. These locations are also expected to be the sites of future massive star formation. The properties of these clumps have been summarized by Tan et al. (2014) based on Galactic observational studies of infrared dark clouds (IRDCs) (e.g., Rathborne et al. 2006; Butler & Tan 2009, 2012) and mm/sub-mm dust continuum emission and molecular line surveys of clumps (e.g., Schuller et al. 2009; Ginsburg et al. 2012; Ma et al. 2013). There are a range of clump masses observed from $\sim 100\,M_\odot$ to $\sim 10^5\,M_\odot$.

In the fiducial turbulent clump model, the mass surface density of the clump of interest is only a factor of 1.22 times higher than that of its surrounding cloud (MT03). Therefore, the observed surface densities of the clumps give a reasonable estimate of the mass surface densities of the ambient clouds, $\Sigma_{\rm cloud}$, which is the other main parameter needed to set up the initial conditions of the models. The observed values of the mass surface density of Galactic clumps and protoclusters are in the range from ~ 0.03 to 1 g cm^{-2}.

In the setup of our initial conditions in this paper, we make several simplifying assumptions as first steps in describing the complexity of star cluster formation: (i) the parent clump is isolated (i.e., no external tidal fields); (ii) the clump is in hydrostatic and virial equilibrium with the structure of a singular polytropic sphere (MT03); (iii) stars are born with the same velocities as their parent gas, so that their velocity dispersion profile is the same as that of the initial gas; (iv) all stars form instantaneously, and the remaining gas is also expelled instantaneously at this time; (v) the star formation efficiency (SFE) is spatially constant, which means that the stars follow the same spatial distribution as the initial gas; (vi) there is no initial spatial or kinematic substructure given to the stars, except that which results from random Poisson sampling; and (vii) following an initial test model of equal-mass stars, a standard Kroupa initial mass function (IMF) for the stars (Kroupa 2001) is adopted, and various binary properties are investigated. It should be remembered that these are starting assumptions and that many of them will be relaxed in subsequent investigations. However, first, the behavior of this simplest, idealized model needs to be understood.

2.1. Initial Stellar Phase-space Distributions

First, we define the physical and kinematic properties of the pre-cluster clump, i.e., mass, size, density profile, and velocity dispersion profile. Stars are born from this clump and initially follow the same phase-space (position, velocity) distribution. MT03 characterize pre-cluster clumps and pre-stellar cores as singular polytropic spheres in virial and hydrostatic equilibrium. The density profile of such clumps is then

$$\rho_{\rm cl}(r) = \rho_{\rm s,cl}\left(\frac{r}{R_{\rm cl}}\right)^{-k_\rho}, \tag{1}$$

where $\rho_{\rm s,cl}$ is the density at the surface of the clump, i.e., at radius $R_{\rm cl}$. We adopt $k_\rho = 1.5$ as a fiducial value, i.e., the same as that of MT03, who made their choice based on observations of clumps reported at the time. No significant difference was found in later measurements performed by Butler & Tan (2012) in IRDCs, where they found $k_\rho \simeq 1.6$. For simplicity and consistency with the previous analysis of MT03, we thus keep $k_\rho = 1.5$ as our fiducial value. The density at the surface of the clump can be expressed as

$$\rho_{\rm s,cl} = \frac{(3-k_\rho)M_{\rm cl}}{4\pi R_{\rm cl}^3}, \tag{2}$$

where $M_{\rm cl} = M(r < R_{\rm cl})$ is the total mass of the clump.

The radius of a clump in virial and pressure equilibrium with its surroundings, i.e., a larger self-gravitating cloud of a given mass surface density, $\Sigma_{\rm cloud}$, is (MT03; Tan et al. 2013, hereafter T13)

$$R_{\rm cl} = 0.50\left(\frac{A}{k_p\phi_{P,\rm cl}\phi_{\bar P}}\right)^{1/4}\left(\frac{M_{\rm cl}}{3000\,M_\odot}\right)^{1/2} \times \left(\frac{\Sigma_{\rm cloud}}{1\ {\rm g\ cm^{-2}}}\right)^{-1/2}\ {\rm pc}, \tag{3}$$

Table 1
Parent Clump Parameters

	$\Sigma_{\rm cloud}$	$M_{\rm cl}(M_\odot)$	$R_{\rm cl}$ (pc)	k_ρ	$\phi_{P,{\rm cl}}$	$\phi_{\bar{P}}$	$\phi_{\rm B}$	$\sigma_{\rm cl}$ (km s^{-1})
Low-Σ Clump	0.1	3000	1.159	1.5	2	1.31	2.8	1.71
High-Σ Clump	1	3000	0.367	1.5	2	1.31	2.8	3.04

Table 2
Initial Conditions for Simulation Sets

Set Name	ϵ	$\langle N_*\rangle$	$f_{\rm bin}$	$f(e)$	IMF	IMS	SE	Comment in Plots
equal_mass	0.5	1500	0	⋯	Single mass	N	N	Single equal-mass particles
single_imf	0.5	4000	0	⋯	Kroupa (2001)	N	N	Single stars with IMF (no SE)
binaries_50	0.5	4000	0.5	$\delta(e)$	Kroupa (2001)	N	N	50% binaries (no SE)
fiducial	0.5	4000	0.5	$\delta(e)$	Kroupa (2001)	N	Y	Fiducial case
binaries_un	0.5	4000	0.5	uniform	Kroupa (2001)	N	Y	e uniform distribution
binaries_th	0.5	4000	0.5	$2e$	Kroupa (2001)	N	Y	e thermal distribution
segregated	0.5	4000	0.5	$\delta(e)$	Kroupa (2001)	Y	Y	Mass segregated
binaries_100	0.5	4000	1	$\delta(e)$	Kroupa (2001)	N	Y	100% binaries
sfe_10	0.1	850	0.5	$\delta(e)$	Kroupa (2001)	N	Y	SFE = 10%
sfe_30	0.3	2500	0.5	$\delta(e)$	Kroupa (2001)	N	Y	SFE = 30%
sfe_80	0.8	6500	0.5	$\delta(e)$	Kroupa (2001)	N	Y	SFE = 80%
sfe_100	1.0	7300	0.5	$\delta(e)$	Kroupa (2001)	N	Y	SFE = 100%

Notes. For each of the sets named in the first column, 20 simulations were performed for each of the clump parameters listed in Table 1. The second column shows the assumed SFE, the third column shows the average number of stars per simulation, the fourth column shows the primordial binary fraction, the fifth column shows the eccentricity distribution function, the sixth column shows the assumed IMF, the seventh column shows whether the cluster is initially mass segregated (IMS), the eighth column shows whether SE is included in the set, and the ninth column shows comments from which we will refer to the set in the graphs for clarity.

$$\rightarrow 0.37 M_{\rm cl,3000}^{1/2}\Sigma_{\rm cloud,1}^{-1/2}\ {\rm pc}, \quad (4)$$

where $k_p = 2(k_\rho - 1)$ is the power-law exponent of the pressure (P) within the clump; $\phi_{P,{\rm cl}}$ is the ratio of the pressure at the surface of the clump ($P_{\rm s,cl}$) and the mean pressure inside the cloud, $\bar{P}_{\rm cloud}$; $\phi_{\bar{P}}$ is a normalization constant, $\sim\mathcal{O}(1)$, in the relation $\bar{P}_{\rm cloud} \equiv \phi_{\bar{P}} G\Sigma_{\rm cloud}^2$; and $A = (3 - k_\rho)(k_\rho - 1)f_g \rightarrow 3/4$, since we assume that the clump is initially starless, so $f_g = 1$. As fiducial values, we choose $\phi_{P,{\rm cl}} = 2$ and $\phi_{\bar{P}} = 1.32$ (see MT03; T13). Thus, the structural properties of the fiducial clump are specified by two parameters: $M_{\rm cl}$ and $\Sigma_{\rm cloud}$. In this study, we will focus on the case of $M_{\rm cl} = 3000\,M_\odot$ and investigate $\Sigma_{\rm cloud} = 0.1$ and 1 g cm^{-2}, which are representative of the range of values observed in real clumps (Tan et al. 2014).

The total mass of stars, M_*, that form from the clump is given as

$$M_* = \epsilon M_{\rm cl}, \quad (5)$$

where ϵ is the overall SFE. We will consider a range of values from $\epsilon = 0.1$ to 1, with a fiducial value of 0.5. The stars are assumed to have the same structural profile as the clump, i.e., ϵ is independent of radial location. Then, the density profile of the stars is simply $\rho_*(r) = \epsilon\rho_{\rm cl}(r)$. The cumulative radial mass distribution of the stars is

$$M_*(r < R_{\rm cl}) = M_*\left(\frac{r}{R_{\rm cl}}\right)^{3-k_\rho}. \quad (6)$$

To set up the positions of the stars, we first create the mass sample from a given IMF (including binary companions), i.e., in the fiducial case, a standard Kroupa IMF (Kroupa 2001) with individual masses in the range $0.01\,M_\odot < m_i < 100\,M_\odot$, in random order. Next, we create a cumulative mass array from the previous sample to choose the individual distance from the center r_i according to Equation (6) (in the case of 100% mass segregation—see below—masses are sorted from the most massive to the least massive before this step). Finally, we place the star randomly on the surface of the sphere of radius r_i. In this way, we ensure that the clusters always match the desired initial density profile, no matter the nature of the stellar IMF.

The kinematic properties of the clump are specified by the condition of virial equilibrium. In a virialized clump, the velocity dispersion σ scales in the same manner as the effective sound speed $c \equiv (P/\rho)^{1/2}$. Therefore, the velocity dispersion profile of the clump is

$$\sigma_{\rm cl}(r) = \sigma_{\rm cl,s}\left(\frac{r}{R_{\rm cl}}\right)^{(2-k_\rho)/2}, \quad (7)$$

where $\sigma_{\rm cl,s}$ is the velocity dispersion at the surface of the clump. The presence of large-scale magnetic fields can provide some support to the clump so that a smaller turbulent velocity dispersion is needed to achieve virial equilibrium. The effect of the magnetic fields on the stability of the clump can be expressed as $\phi_{\rm B} \equiv \langle c^2\rangle/\langle\sigma^2\rangle$. Then, the velocity dispersion at the surface is

$$\sigma_{\rm cl,s} = 5.08\left(\frac{\phi_{P,{\rm cl}}\phi_{\bar{P}}}{Ak_P^2\phi_{\rm B}^4}\right)^{1/8}\left(\frac{M_{\rm cl}}{3000\,M_\odot}\right)^{1/4} \times\left(\frac{\Sigma_{\rm cloud}}{1\ {\rm g\ cm^{-2}}}\right)^{1/4}{\rm km\ s^{-1}}, \quad (8)$$

where we use $\phi_{\rm B} = 2.8$ as a fiducial value, which is the value for regions with an Alfvén Mach number of 1 (see Appendix

A2 of MT03). The initial velocity dispersion profile of the stars then follows Equation (7). The individual stellar velocities are then assigned velocities in each of the x, y, and z directions independently by drawing from a Gaussian centered at zero with width $\sigma(r)$. Note that the mass-averaged velocity dispersion of the clump/cluster is (T13)

$$\sigma_{\rm cl} = \frac{2(3-k_\rho)}{8-3k_\rho}\sigma_{\rm cl,s} \rightarrow \frac{6}{7}\sigma_{\rm cl,s}. \quad (9)$$

The resulting velocity distribution has the form of a Maxwell–Boltzmann distribution with $\sigma_{3D} = \sqrt{3}\,\sigma_{\rm cl}$ but with a one-dimensional velocity dispersion profile as in Equation (7). The properties of the clumps, i.e., the low- and high-Σ cases, are summarized in Table 1.

2.2. The Primordial Binary Population

Observational evidence shows that about half of the star systems in the field are binaries (e.g., Duquennoy & Mayor 1991; Fischer & Marcy 1992; Mason et al. 1998; Preibisch et al. 1999; Close et al. 2003; Basri & Reiners 2006; Raghavan et al. 2010). Given the densities of star-forming clumps and young star clusters, it is likely that most of these binaries were born together inside individual cores, rather than forming via subsequent dynamical interactions (e.g., Parker & Meyer 2014). However, this is a question that our simulations will be able to address.

Theoretically, a full understanding of binary formation from a collapsing gas core is likely to require a full non-ideal magnetohydrodynamic (MHD) treatment to resolve the formation of the accretion disk and, later, its potential fragmentation. The difficulty of this problem means that, essentially, the statistical properties of primordial binaries are very uncertain, so we will investigate several different choices based on observations.

For most of our simulations that include binaries, we assume a binary system fraction, $f_{\rm bin} = 0.5$. We adopt a period distribution from the survey (Raghavan et al. 2010) using a log-normal period distribution with a mean of $P = 293.3$ yr and a standard deviation of $\sigma_{\log P} = 2.28$ (with P in days). We use a companion mass ratio distribution of the form $dN/dq \propto q^{0.7}$, based on observations in young star clusters (Reggiani & Meyer 2011). The eccentricity distribution remains less well constrained. While Duquennoy & Mayor (1991) found a thermal distribution, i.e., $f(e) = 2e$ for solar-type stars in the solar neighborhood, a similar, more recent study (Raghavan et al. 2010) found a flat eccentricity distribution for the same kind of stars. However, if binaries form mainly via disk fragmentation, we would expect that they are born with near-circular orbits. In order to measure how much binaries are affected by dynamical interactions in the different models, we adopt initially circular orbits for the eccentricities in our fiducial model. We also investigate cases with initially thermal and uniform distributions of eccentricities.

2.3. Overview of the Cluster Models

For each of the low- and high-Σ clumps (see Table 1), we set up a stellar cluster as described above, i.e., assuming a constant SFE(r) and a velocity dispersion profile equal to that of the parent clump. Thus, the initial crossing time (i.e., dynamical time) is defined by the properties of the parent clump to be $t_{\rm cr} \equiv R_{\rm cl}/\sigma_{\rm cl}$, i.e., 0.663 and 0.118 Myr for the $\Sigma_{\rm cloud} = 0.1$ and 1 g cm^{-2} cases, respectively.

We run 20 realizations for each set of initial conditions, which are summarized in Table 2. The simulations are run for 20 Myr, varying only the random seed between simulations in the same set; this affects the initial positions and velocities of the stars, as well as the IMF sampling.

We construct these sets of simulations starting from the simplest case and moving to the one that defines our fiducial case. We start by using only single-mass particles of $m_i = 1\,M_\odot$ with no primordial binaries and with an SFE of 50% in the set `equal_mass`. Next, we include an IMF, assuming the Kroupa (2001) distribution with a mass range from 0.01 to 100 $M_\odot$ defining the set `single_imf`, again with no initial binaries. We then include 50% primordial binaries with circular orbits and other properties described in Section 2.2, defining the set `binaries_50`. The above three simulation sets do not include SE. We define the `fiducial` simulation set by assuming a Kroupa IMF and an SFE of 50%, with 50% of the stars as primordial binary systems with initial circular orbits and SE included.

Next, we test other choices and parameters of the fiducial model. We test two other eccentricity distributions: a thermal eccentricity distribution, i.e., $f(e) = 2e$ in the set `binaries_th`, and a uniform eccentricity distribution between 0 and 1 in the set `binaries_un`. An extreme scenario of mass segregation is tested in the set `segregated`, in which stars are sorted in descending order of individual stellar mass from the center of the cluster. We also test the extreme case in which all stars are binary systems ($f_{\rm bin} = 1$) in the set `binaries_100`.

We also carry out simulations with different SFEs. These simulations only differ from the `fiducial` set in their SFE; i.e., the average number of stars per simulation in each set increases with the SFE, since we use the same parent clump of $M_{\rm cl} = 3000\,M_\odot$. The SFEs investigated are SFE = 10%, 30%, 80%, and 100%, and the sets are named `sfe_10`, `sfe_30`, `sfe_80`, and `sfe_100`, respectively.

2.4. Numerical Methods

We follow the evolution of the star clusters for 20 Myr utilizing the direct N-body integrator NBODY6++ (Wang et al. 2015), which is a GPU/MPI-optimized version of the classical and widely used direct integrator NBODY6 (Aarseth 2003). NBODY6++ has implemented special regularizations to accurately follow the evolution of binaries and high-order systems in the cluster and is able to efficiently simulate star clusters with high binary fractions with no loss of accuracy. For cases with SE, we used the recipe included in NBODY6++ based on the analytical models for single and binary SE developed by Hurley et al. (2000, 2002). The code also has implemented artificial velocity kicks to emulate asymmetrical supernova ejections. The magnitudes of the kicks are drawn from a Maxwell distribution with $\sigma = 265$ km s^{-1} following the observations of Hobbs et al. (2005) on pulsar proper motions.

3. Results

3.1. Initial Dynamical State of the Clusters

Before performing any simulation from the assumptions described in Section 2, we first derive the initial dynamical state

of the clusters by characterizing their virial ratio, i.e.,

$$Q_i = -\frac{T_*}{\Omega}, \tag{10}$$

where T_* is the total kinetic energy of the stars and Ω is their total gravitational potential energy. A cluster with $Q_i < 1$ is bound, and $Q_i = 0.5$ is the value for a state of virial equilibrium. We assume that the gas was expelled immediately after the stars formed; thus, Ω only depends on the stars in the cluster, i.e., $\Omega = \Omega_*$. The potential of the stars is then

$$\Omega_* = -\frac{G}{2}\int_0^{R_{\rm cl}} \left[\frac{M(r < R_{\rm cl})}{r}\right]^2 dr - \frac{G}{2}\int_{R_{\rm cl}}^{\infty}\left(\frac{M_*}{r}\right)^2 dr \tag{11}$$

$$= -\left(\frac{3 - k_\rho}{5 - 2k_\rho}\right)\frac{GM_*^2}{R_{\rm cl}}. \tag{12}$$

The kinetic energy of the stars is given by

$$T_* = \frac{3}{2}M_*\sigma^2, \tag{13}$$

where σ is the one-dimensional mass-averaged velocity dispersion. Assuming that the stars are born from the gas following the same dispersion profile, σ is related to the velocity dispersion at the surface by Equation (9).

Substituting with Equations (9), (13), and (12) in Equation (10), as well as replacing $R_{\rm cl}$ and $\sigma_{\rm cl,s}$ with their expressions in Equations (3) and (8), respectively, we obtain

$$Q_i = \frac{3(5 - 2k_\rho)(3 - k_\rho)}{(8 - 3k_\rho)^2(k_\rho - 1)}\frac{1}{\epsilon\phi_{\rm B}}, \tag{14}$$

$$Q_i \rightarrow \frac{0.51}{\epsilon}, \tag{15}$$

where the arrow shows the relation using the fiducial values for the clump. Values of Q_i versus SFE are shown for different models in Figure 1.

The dynamical state of the clusters also depends on the presence of magnetic fields in the initial clump, i.e., $\phi_{\rm B}$. In the absence of magnetic field support ($\phi_{\rm B} = 1$), the velocities needed for virial equilibrium are higher, and stars formed from such gas will have higher values of Q_i; e.g., even in the best-case scenario, with an SFE of 100%, we have $Q_i \simeq 1.6$ (and $\simeq$3 for an SFE of 50%). However, in the fiducial case, with approximate equipartition of the energy density from large-scale magnetic fields and turbulence ($\phi_{\rm B} \simeq 2.8$), an SFE of about 50% leads to a cluster that is marginally gravitationally bound ($Q_i \simeq 1$). Note that this variation of $\phi_{\rm B}$ also corresponds to a variation in the virial parameter of the gas clump, $\alpha_{\rm vir} = 5\langle\sigma^2\rangle R/(GM)$, since, for the fiducial case with $k_\rho = 1.5$, we have $\alpha_{\rm vir} = 15/(4\phi_{\rm B}) \rightarrow 1.34$ (see Appendix A of MT03).

3.2. The Bound Stellar Cluster

As discussed in Section 3.1, star clusters born from turbulent clumps bounded by high-pressure ambient environments can start with relatively high velocity dispersions. Their virial ratio after gas expulsion will depend on the global SFE and the contribution of magnetic fields to the support of the parent clump, i.e., $\phi_{\rm B}$. There will be significant initial mass loss of the stars that are born unbound, occurring on a timescale of a few crossing times. However, the gaseous clump is assumed to have a positive power law for the velocity dispersion with radius (see Equation (9)) and so is more likely to be left with a central gravitationally bound core. In contrast, a relaxed star cluster (e.g., with a Plummer profile) has a velocity dispersion profile that decreases with radius. We thus expect differences in the early evolution of our clusters compared to those modeled with initial Plummer profiles by, e.g.,

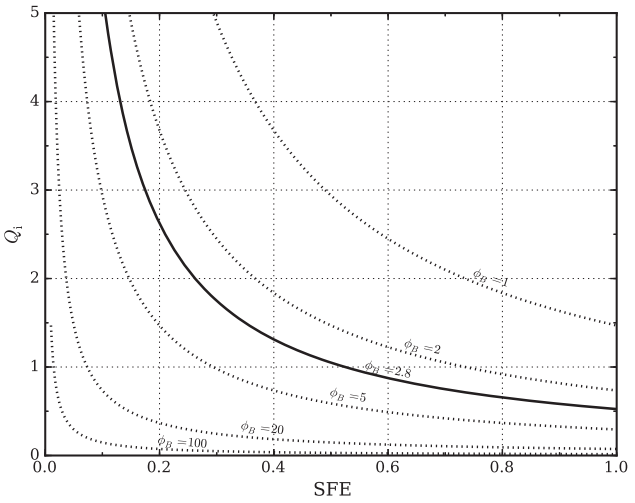

Figure 1. Initial virial ratio Q_i as a function of SFE from the clump. The solid line shows the relation for our fiducial value, and the dotted lines show the relation for different values of $\phi_{\rm B}$.

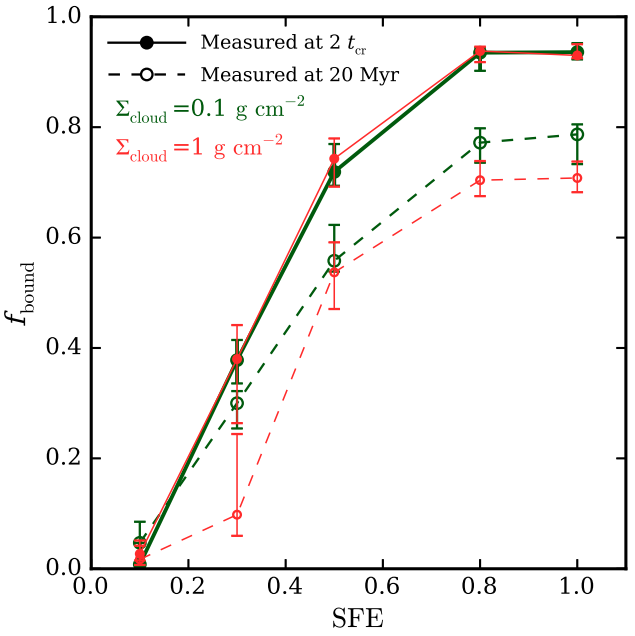

Figure 2. Bound mass fraction, $f_{\rm bound}$, as a function of SFE. Solid lines and points show the results at early times ($2t_{\rm cr}$); the dashed lines and open points show the results at the end of the simulations (20 Myr). The values are the mean averages for the simulation sets (each of 20 realizations) with cases shown for $\Sigma_{\rm cloud} = 0.1$ (green) and 1 g cm^{-2} (red). Error bars show the values between the 25th and 75th percentiles. Dynamical evolution leads to a general decrease of $f_{\rm bound}$ during the first 20 Myr of these clusters.

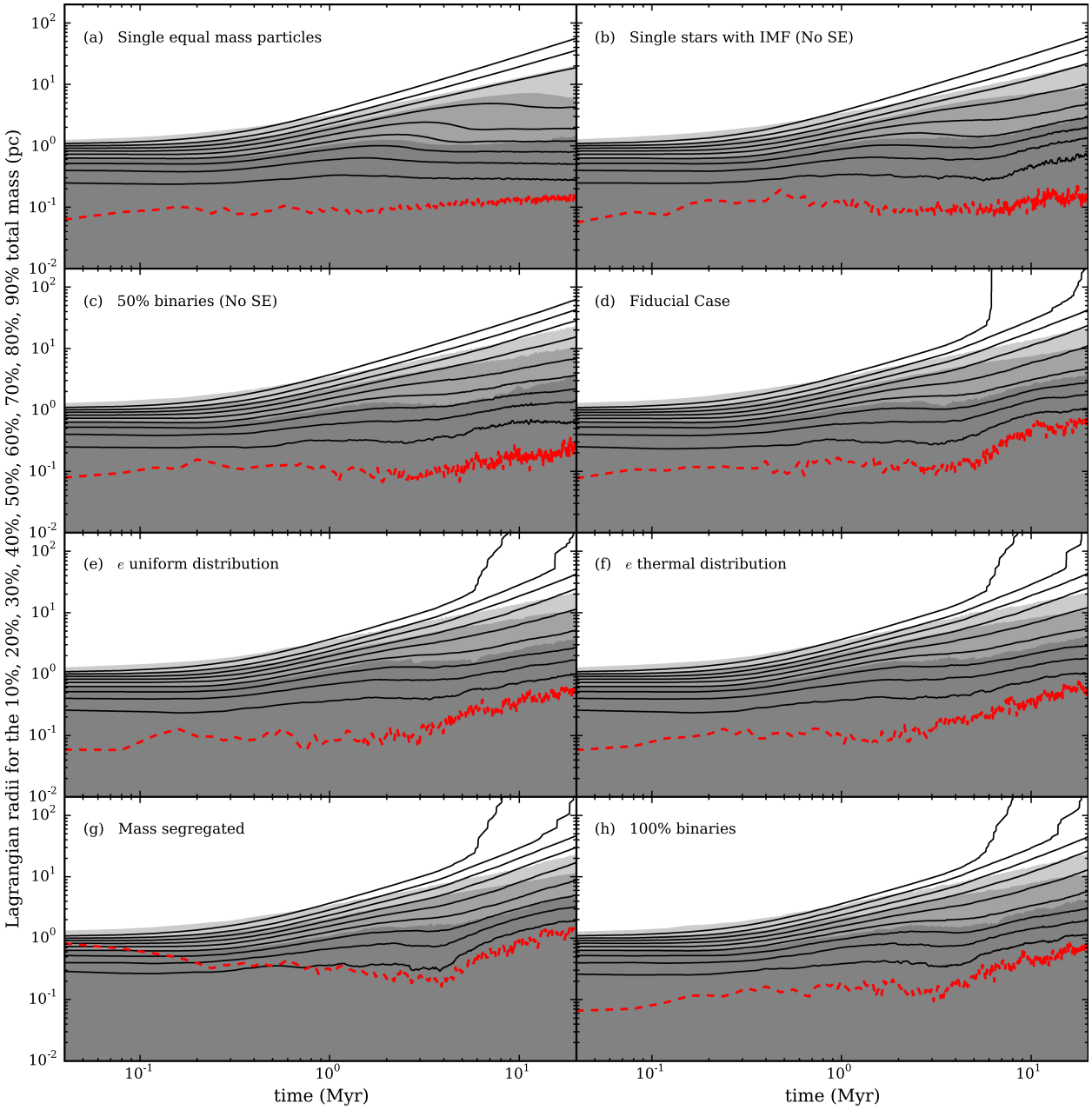

Figure 3. Average Lagrangian radii evolution for different sets of simulations for star clusters born from a parent clump with $\Sigma_{\rm cloud} = 0.1$ g cm^{-2}. We show the Lagrangian radii for the 10%, 20%, 30%, 40%, 50%, 60%, 70%, 80%, and 90% masses (black solid lines). Red dashed lines are the core radii defined in Aarseth (2003). Gray shaded areas represent the regions below the 50%, 95%, and 100% mass–radius of the bound cluster.

Goodwin & Bastian (2006), Baumgardt & Kroupa (2007), and Pfalzner & Kaczmarek (2013).

To measure the bound mass fraction, $f_{\rm bound}$, at each timestep of cluster evolution, we construct the bound entity based on an accurate measure of the mean velocity of the bound stars, and we select all stars with negative total energy in the frame of reference of the bound cluster. The velocity of the bound cluster is not known a priori (although it is expected to be close to the zero velocity of the reference frame); thus, this is solved in an iterative calculation. We start by selecting all stars with negative energy inside the half mass–radius of the full cluster and then iterate until the members between iterations do not change by more than two members. This method, called "snowballing," is described in Smith et al. (2013b).

Figure 2 shows the bound fractions measured at two crossing times and after 20 Myr for clusters with different SFEs for simulations with a parent clump with $\Sigma_{\rm cloud} = 0.1$ and 1 g cm^{-2}. The initially positive radial gradient of the velocity dispersion of the star clusters causes stars in the outer parts to leave first, while the central core can remain bound. The mass fraction of this remnant bound core depends on the initial global SFE. Later dynamical evolution and internal mass loss of its members due to SE leads to a slower decrease in the mass of the bound core over time.

The results shown in Figure 2 are those for the fiducial case, i.e., with $\phi_{\rm B} = 2.8$. As discussed in Section 3.1, the initial virial ratio of the star clusters depends sensitively on this value: a higher value of $\phi_{\rm B}$ shifts the trend shown in this figure

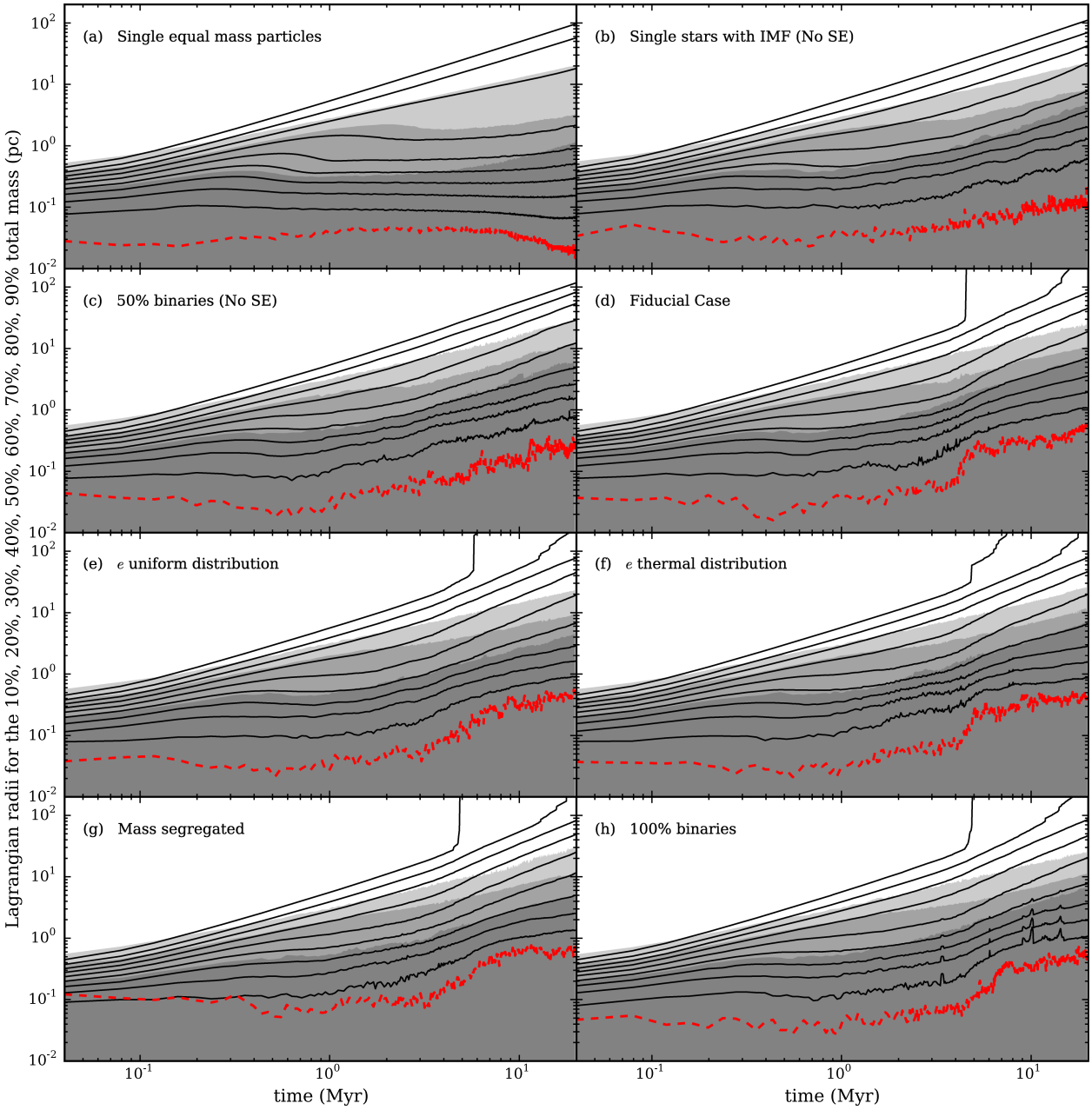

Figure 4. Same as Figure 3, but for star clusters born from a clump with $\Sigma_{\rm cloud} = 1$ g cm^{-2}.

upward so that even clusters with SFE = 10% may retain a significant bound core if $\phi_{\rm B}$ is sufficiently high.

3.3. Global Evolution

Here we explore the evolution of the structure of the clusters with time. The fiducial case has an SFE of 50% and $Q_i = 1.02$, slightly above the criterion for global boundedness. Therefore, initial expansion and some initial mass loss is expected. We show the evolution of the Lagrangian radii with time in Figures 3 and 4 for $\Sigma_{\rm cloud} = 0.1$ and 1 g cm^{-2}, respectively, where the values presented are the average of the 20 simulations performed for each set. In each figure, panels (a)–(d) show the effects of gradually adding greater degrees of realism to make the fiducial model. Panels (e)–(h) show the effects of different choices of initial binary properties and degree of initial mass segregation. The figures also show the evolution of the core radius $r_{\rm c}$ (red dashed lines), which is the density-averaged distance from the density center of the cluster (see Section 15.2 of Aarseth 2003).

As expected, the clusters expand with time. The expansion rate of the outer Lagrangian radii of the clusters, i.e., of the unbound stars, is determined by the initial velocity dispersion of the parent clump, which is higher at higher-mass surface densities. Thus, the star clusters starting from a clump with $\Sigma_{\rm cloud} = 1$ g cm^{-2} are soon more extended than the clusters forming from clumps with $\Sigma_{\rm cloud} = 0.1$ g cm^{-2} of the same mass and SFE; i.e., the half mass–radius at 20 Myr of the first group is $\sim$20 pc, compared to $\sim$10 pc for the lower-Σ case.

Initial expansion of the bound portion of the cluster happens early, within a few crossing times, as the clusters relax to a

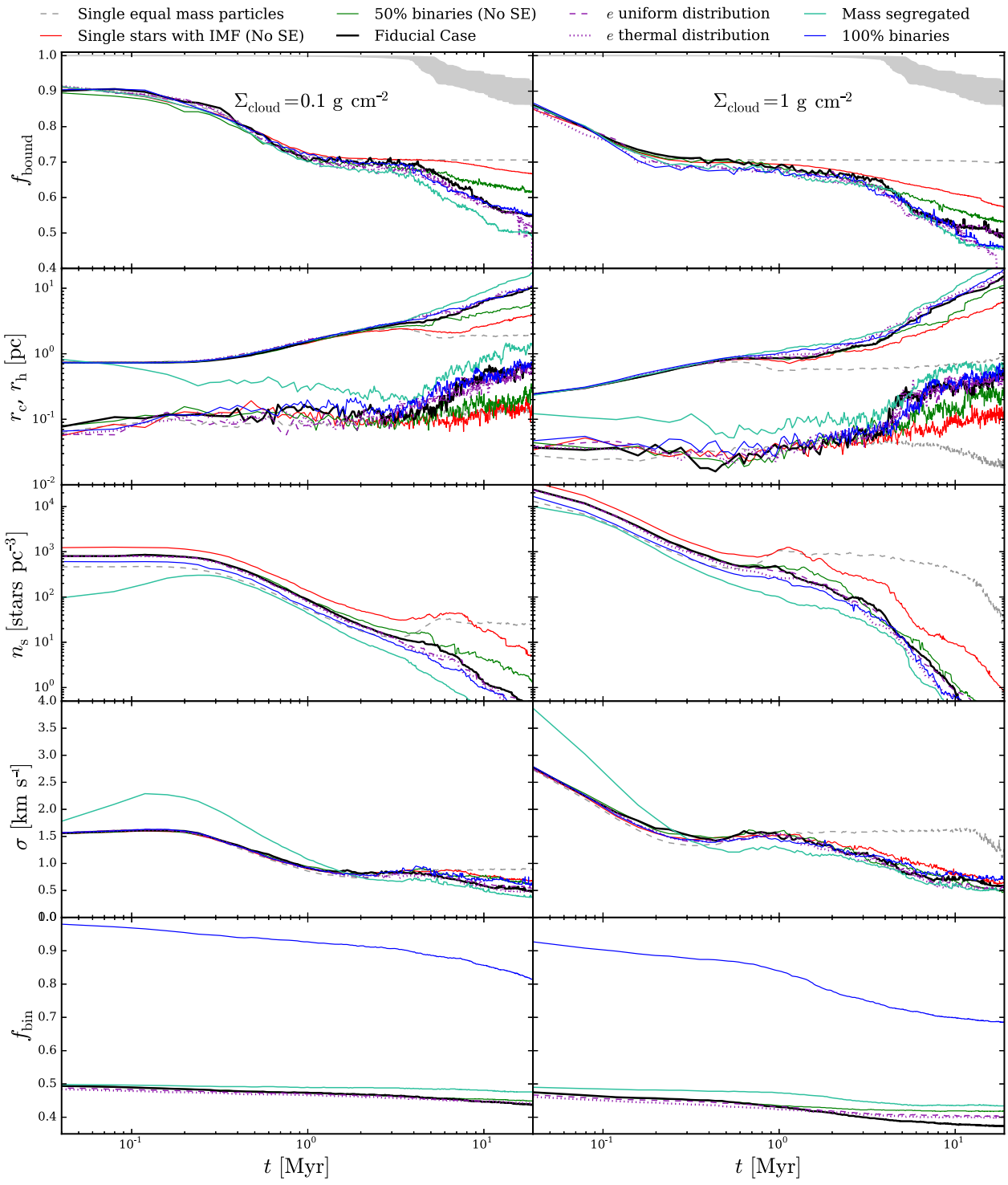

Figure 5. Time evolution of properties of fiducial clusters forming with SFE = 50%. The left column shows the clusters forming from a $\Sigma_{\rm cloud} = 0.1$ g cm^{-2} environment; the right column shows a $\Sigma_{\rm cloud} = 1$ g cm^{-2} environment. The lines in each panel show the median values calculated from the 20 simulations performed for each set. The first row shows the fraction of bound mass in the cluster relative to the initial mass; unbound stars inside the 95% mass–radius of the bound cluster are kept to show the timescale of their escape. We also show the fraction of the total stellar mass in the `fiducial` simulations that remains after accounting for SE mass loss; the gray shaded region shows the area between the 25th and 75th percentiles. The second row shows the evolution of the core radius ($r_{\rm c}$) and half mass–radius $r_{\rm h}$ for all the stars in the simulation. The third row shows the average number density of systems ($n_{\rm s}$), where by "systems" we refer to singles and binaries, measured inside the volume defined by $r_{\rm h}$. The fourth row shows the evolution of the velocity dispersion measured inside $r_{\rm h}$, and the fifth row shows the evolution of the global binary fraction.

virialized state. The later evolution is affected by dynamical interactions between the stars (i.e., mass segregation, evolution of binaries, and dynamical ejection of stars from unstable multiple systems) and mass loss resulting from SE. The relative importance of these effects can be gauged by examining the sequence of panels (a)–(d) in Figures 3 and 4. The later-stage expansion of the bound cluster is negligible in the case of equal-mass stars. The model with an IMF but only single stars

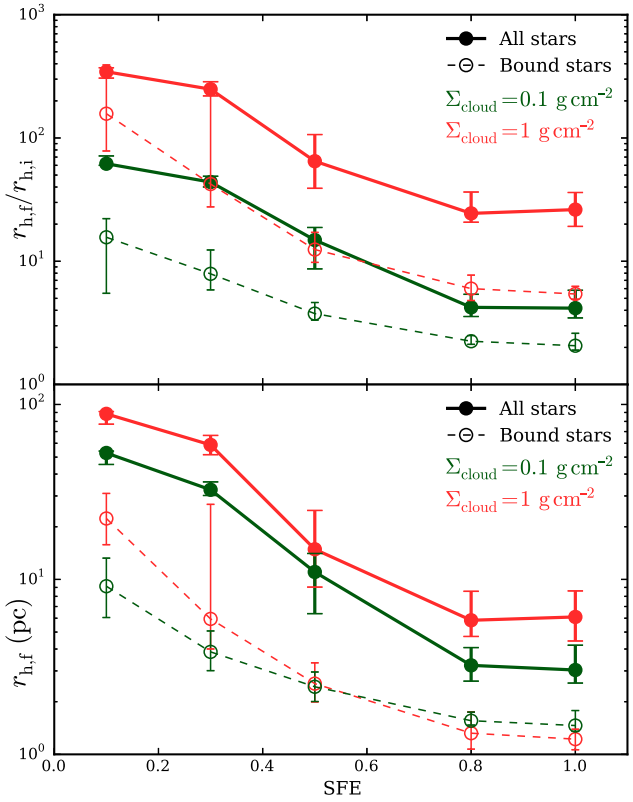

Figure 6. Size of star clusters at 20 Myr as a function of SFE. The top panel shows the final half mass–radius, $r_{h,f}$, compared to the initial half mass–radius, $r_{h,i}$. The bottom panel shows $r_{h,f}$ in physical units. Filled circles show measurements using all stars; open circles show measurements using only the bound cluster. Values are medians over the 20 simulations performed for each set, and error bars show the region between the 25th and 75th percentiles.

undergoes mass segregation that leads to noticeable expansion after about 6 Myr in the case of $\Sigma_{cloud} = 0.1$ g cm^{-2} and after about 1 Myr in the case of $\Sigma_{cloud} = 1.0$ g cm^{-2}.

Note that before adding binaries and SE in our models, the evolution of the star clusters with high Σ_{cloud} would be exactly the same as those with low Σ_{cloud} after properly scaling for the initial size and crossing time (see Aarseth & Heggie 1998). However, the characteristic timescales introduced by binaries (e.g., at their typical orbital separation) and SE break this self-similarity.

When binaries are added, their presence leads to another potential source of expansion, since their binding energy couples with the internal energy of the stellar cluster, leading to a change of kinetic energy in each interaction (Heggie 1975; Hills 1975). However, little difference appears when moving from single stars to 50% binaries, even in simulations with the high-Σ initial condition that can suffer more interactions. As we will see in Section 3.4, the initial densities of these models are not high enough and/or do not last long enough to give binaries, on average, the chance to interact significantly with other stars.

The inclusion of SE causes the cluster to expand even more. SE starts becoming important after a few Myr, when the first massive stars lose mass by stellar winds and then explode as supernovae. The supernova explosions may cause stars to be ejected (e.g., as fast runaway stars) by either the destruction of tight binaries, velocity kicks caused by the asymmetrical explosion, or both (see the outer two lines in Figures 3 and 4). We focus on the ejection of runaway stars in Section 3.6. For now, we see that cluster expansion is increased by this effect and by the fact that the potential well of the cluster is made shallower with the loss of mass through stellar winds and supernovae. However, the loss of runaway stars does not affect the global evolution of the cluster too much, even in the most extreme case with $f_{bin} = 1$. Finally, panels (e)–(h) in these figures show that variations of binary orbital properties, degree of initial mass segregation, or primordial binary fractions have relatively minor effects.

In Figure 5, we compare the evolution of several parameters of the different sets of simulations for clusters born with different initial mass surface densities: $\Sigma_{cloud} = 0.1$ g cm^{-2} on the left, and $\Sigma_{cloud} = 1$ g cm^{-2} on the right. In the first row, we show the evolution of the bound mass fraction f_{bound}. Only for the purposes of this figure, in order to show the timescale on which initially unbound stars leave the cluster, we count all stars inside the 95% radius of the bound cluster as also being bound. In all panels in this figure, the values are the medians of each set of simulations with the parameters given in Table 2. Also shown in the first row is a shaded area representing the loss of mass due to SE for all stars in the fiducial simulations (including unbound stars). The second row shows the evolution of the core radii, r_c, and the half-mass radii, r_h. The third row shows the evolution of the effective number density, n_s, i.e., the number of systems (a binary is counted as one system) inside the volume defined by r_h. The fourth row shows the evolution of the velocity dispersion measured inside r_h, while the fifth row shows the evolution of the total binary fraction.

It takes about 1.5 t_{cr} for initially unbound stars to leave the bound cluster, leading to f_{bound} decreasing to about 0.7. The velocity profile of the clusters has a positive slope, i.e., higher speeds in the outskirts; this causes outer stars to be more likely to be unbound, with practically no chance of interacting with others. These stars leave the cluster with a velocity dispersion determined by the parent clump, i.e., $\sigma_{cl,s}$. We refer to these as unbound stars, distinguishing them from the ejected stars that escape later due to dynamical ejections. After the first $\sim$1.5 t_{cr}, all initially unbound stars leave the cluster, and later evolution is determined by dynamical interactions and SE.

Simulations with equal-mass stars essentially do not lose further members. With an IMF, mass segregation does lead to some additional mass loss. When including 50% primordial binaries, mass loss at later times is moderately enhanced. Adding in SE, i.e., in the fiducial model, continues this trend, with a final value of $f_{bound} \simeq 0.5$. These trends are mirrored in the expansion of the clusters. Variations of binary orbital properties or primordial binary fractions are seen to have relatively minor effects.

Models with full initial mass segregation show some differences. In the case with $\Sigma_{cloud} = 0.1$ g cm^{-2}, the number densities at the center are initially quite low, and the core of the cluster contracts significantly. After this contraction, the number density is raised in the core, which later expands quite rapidly. Even though the number densities of these clusters are never too high, the few interactions that do occur are enough to expand the cluster, and the evolution of the 50% mass–radius is determined by these interactions.

In general, the star clusters presented here expand considerably regardless of the different parameters of the simulations. The amount of expansion depends on the SFE and the initial cluster density. The top panel of Figure 6 shows the ratio of the half mass–radius at the end of the simulations, $r_{h,f}$, and the half

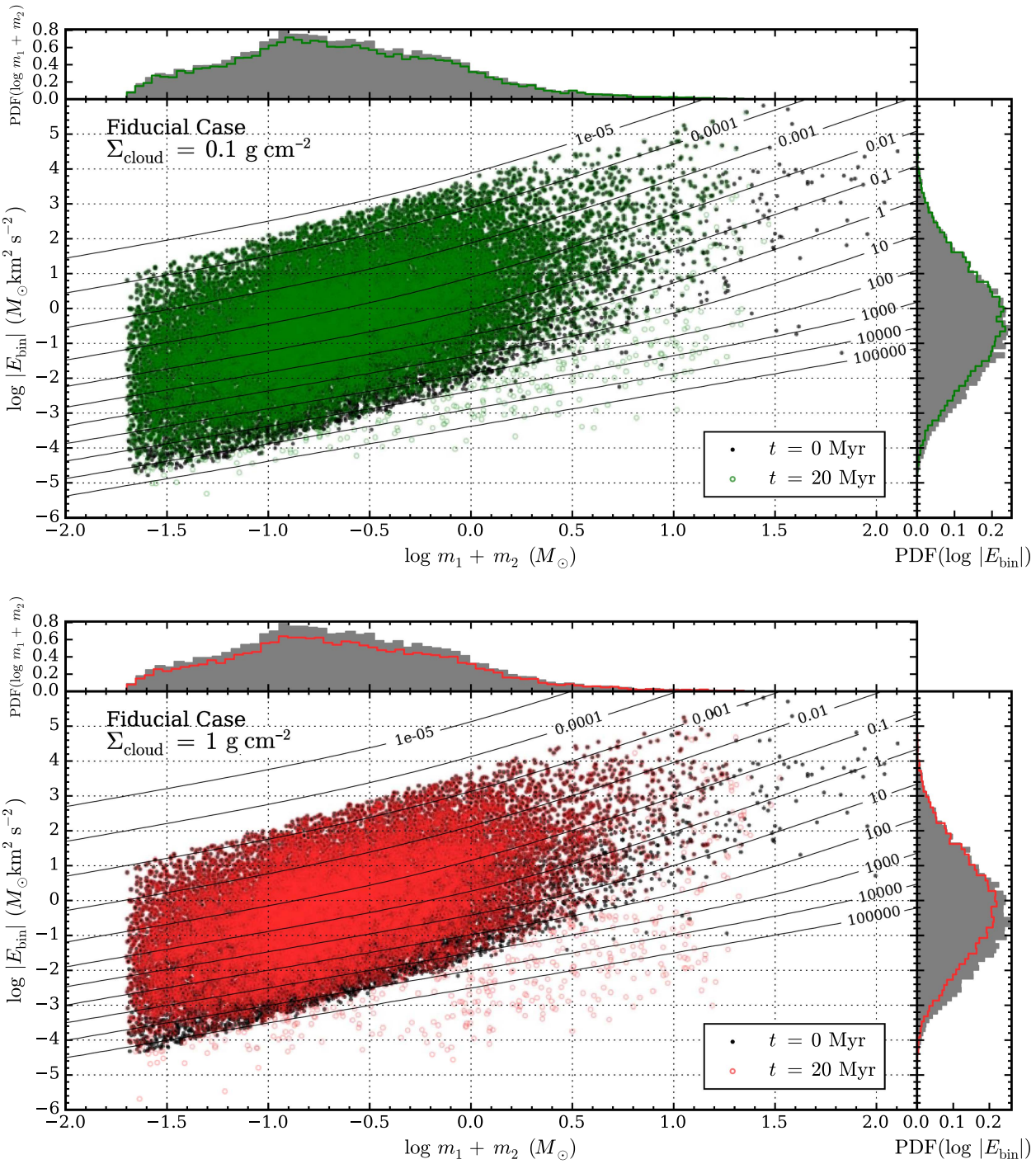

Figure 7. Binding energies as a function of total mass for primordial binaries at the start (black points) and at 20 Myr (red and green open circles) in the set `fiducial` for simulations with $\Sigma_{\rm cloud} = 0.1$ g cm^{-2} (top panel) and $\Sigma_{\rm cloud} = 1$ g cm^{-2} (bottom panel). The side panels show the corresponding probability distribution functions (PDFs), where the case at 20 Myr (red lines) is normalized by the initial number of binaries. Labeled lines represent contours of $\Gamma_{\rm b,eff}$ (Equation (22)) at the beginning of the simulations in units of Myr^{-1}, calculated using values for n_s, m_s, and σ inside the half mass–radius of the cluster. Few binary stars are modified in these models, and typically only those with small binding energies interchange energy with the cluster.

mass–radius at the start, $r_{\rm h,i}$. The differences between the models with high and low initial densities are explained mainly by the initial velocity dispersion of the parent clump. Stars that are born unbound in the denser case escape with a higher typical velocity than those in the less dense case, causing the differences in the expansion. However, when considering the bound part of the cluster, the actual size of the star clusters at 20 Myr is similar regardless of the initial density, as shown in the bottom panel of Figure 6. Differences between the sizes of the bound clusters arise when the SFEs are low. This is due to the fact that the crossing times of these bound systems are large ($t_{\rm cr} \approx 30$ Myr), and they have not yet achieved an equilibrium distribution by 20 Myr. Thus, low-SFE clusters are still in the first phase of their expansion. Regardless of the initial density,

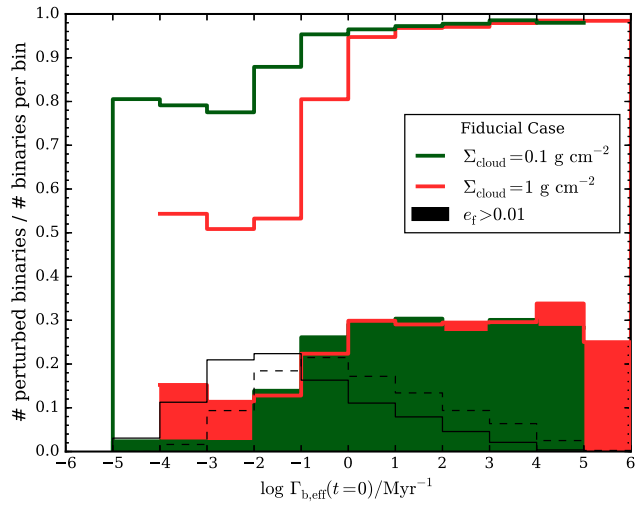

Figure 8. Number of binaries with variations in their binding energies per initial $\Gamma_{b,eff}$ bin divided by the total number of binaries in each bin for all binaries in the set `fiducial`, i.e., the probability of a given binary being modified as a function of the initial $\Gamma_{b,eff}$ for binaries in the set `fiducial`. Shaded areas represent the probability of binaries changing their initial circular eccentricities to values $e > 0.1$. Thin black lines show the total fraction of binaries in each bin for simulations with $\Sigma_{cloud} = 0.1$ g cm^{-2} (solid) and $\Sigma_{cloud} = 1$ g cm^{-2} (dashed). Only binaries with a very high initial $\Gamma_{b,eff}$ are able to considerably modify their initial eccentricity; however, there are a very small number of binaries that fulfill this condition.

the final size of the bound systems depends mainly on the initial SFE: a low SFE results in a more extended bound system.

3.4. The Effects and Evolution of Binaries

Our modeling includes a full treatment of binaries, so we are able to examine their effects and evolution in detail. A binary will be significantly perturbed by an external star (or multiples) if the potential energy of the encounter is similar to that of the initial binary, i.e.,

$$E_{bin} = -\frac{Gm_1m_2}{2a} \sim -\frac{G(m_1+m_2)m_s}{b}, \quad (16)$$

where b is the closest approach of the perturber of mass m_s, and m_1 and m_2 are the primary and secondary masses of the binary, respectively. Therefore, defining $\mu \equiv m_1m_2/(m_1+m_2)$ as the reduced mass of the binary, the closest approach needed to affect the binary properties is

$$b \sim 2a\frac{m_s}{\mu}. \quad (17)$$

We now estimate the perturbation encounter rate of a binary of a given semimajor axis a in our model star clusters. We first derive the rate assuming that stars move without significant deflection, then we include the effects of gravitational focusing. If we assume that the cluster has only single stars and binaries, the mean mass per system is $\langle m_s\rangle = (1+f_{bin})\langle m_i\rangle$. If there are higher-order multiples, then $\langle m_s\rangle$ will be higher; however, these are not included as initial conditions in our models, and we will see that interactions are typically at a relatively low rate so that such multiples do not form in significant numbers during the dynamical evolution of the clusters.

The mean rate of interactions that are able to modify the properties of a binary, Γ_b, is proportional to the cross section defined by b, i.e., πb^2, multiplied by the number density of perturbing systems n_s and a typical velocity in the cluster, i.e., the one-dimensional velocity dispersion, σ. Thus, the interaction rate for binaries with a given semimajor axis a is

$$\Gamma_b = 4\pi\left(\frac{\langle m_s\rangle}{\mu}a\right)^2 n_s\sigma. \quad (18)$$

As we show in Figure 5, the effective number density in our model clusters quickly falls from initial values of $\sim 10^3$–10^4 stars pc^{-3} (depending on the initial environment mass surface density) to values similar to 1 star pc^{-3} at 20 Myr, in our fiducial case. The typical velocity dispersions in the cluster, however, do not vary by much.

We can rewrite Equation (18) for a given binary of semimajor axis a and reduced mass μ in a more convenient way as

$$\Gamma_b(a,\mu) \lesssim 9.67\times10^{-3}\left(\frac{n_s}{10^4\ \mathrm{pc}^{-3}}\right)\left(\frac{\sigma}{2\ \mathrm{km\ s}^{-1}}\right) \times\left(\frac{a}{40\ \mathrm{au}}\right)^2\frac{\langle m_s\rangle^2}{\mu^2}\ \mathrm{Myr}^{-1}. \quad (19)$$

The above estimate does not include the effects of gravitational focusing, which will increase the effective cross section of the encounter by the factor $\mathcal{F} = (b_{eff}/b)^2$, where b_{eff} is the effective impact parameter that leads to a closest approach b. Treating the binary and the perturbing system as single point masses, conservation of energy and angular momentum and Equation (17) imply

$$\mathcal{F} = 1 + \frac{G\mu}{a\sigma^2}\left(\frac{m_1+m_2}{\langle m_s\rangle}+1\right), \quad (20)$$

where a more convenient way to express the last equation is

$$\mathcal{F} \approx 1 + \left[5.55\left(\frac{\mu}{M_\odot}\right)\left(\frac{a}{40\ \mathrm{au}}\right)^{-1}\left(\frac{\sigma}{2\ \mathrm{km\ s}^{-1}}\right)^{-2} \times\left(\frac{m_1+m_2}{m_s}+1\right)\right]. \quad (21)$$

Then, the effective encounter rate including gravitational-focusing effects is

$$\Gamma_{b,eff} = \Gamma_b\mathcal{F}. \quad (22)$$

The interaction rates of binaries are mainly determined by the number density or perturbing systems, which vary by several order of magnitude over the evolution of the clusters, while none of the other environmental parameters involved in Equation (22) vary by much. The other crucial parameters that determine the interaction rate of a binary are its own internal parameters—i.e., the internal binding energy E_{bin}, which determines how resistant the binary is to perturbations—and the total mass of the binary, which determines the strength of the gravitational-focusing effect. These parameters vary by several orders of magnitude between members of the binary population. To give a general picture of the different available interaction rates in the simulations, we show the binary binding energy against the binary mass in Figure 7 for binaries in the set `fiducial` at the start (black points) and at 20 Myr (red and

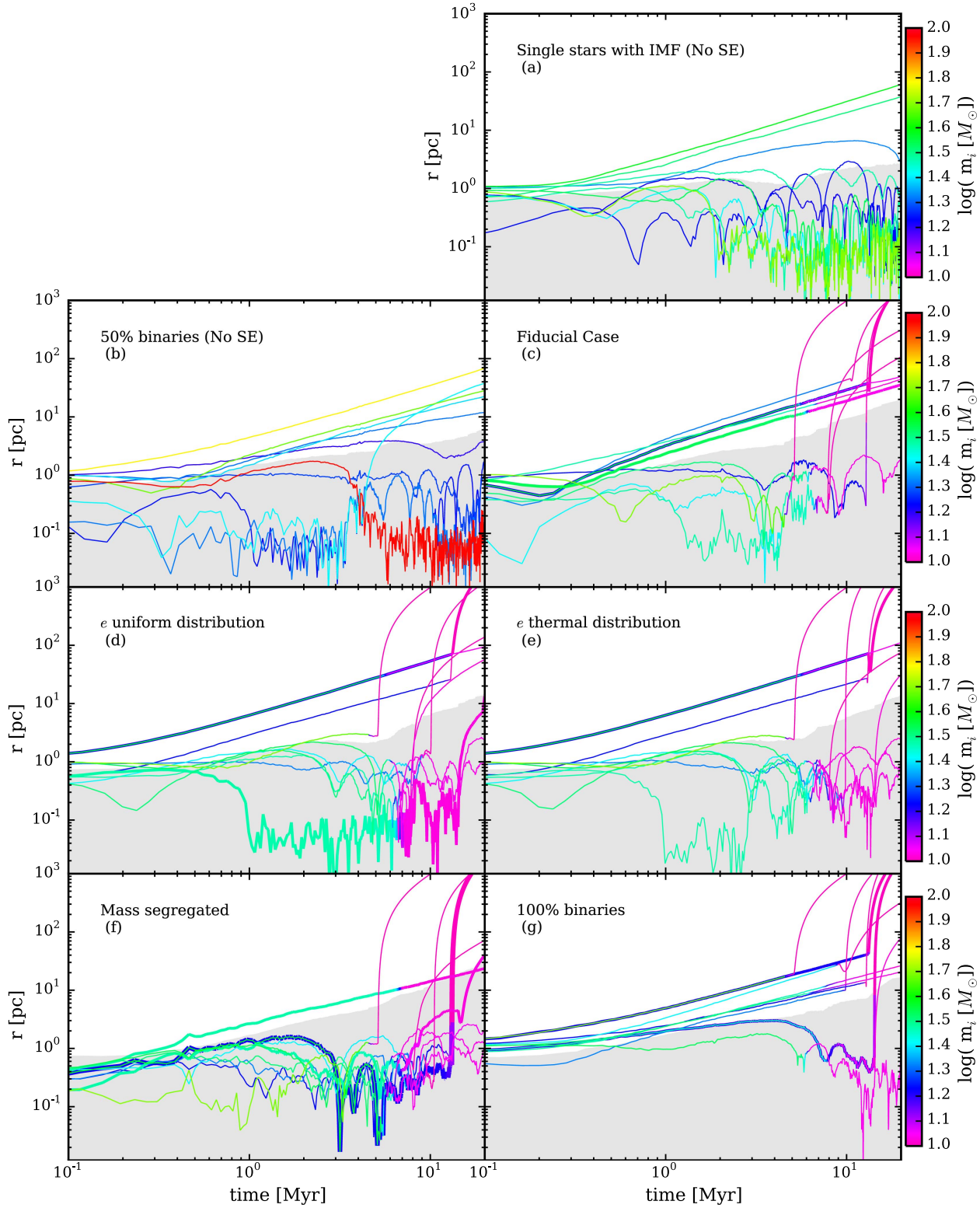

Figure 9. Evolution of the radial location of the 10 most massive stars in example simulations drawn from the model sets that have an IMF and SFE of 50%: (a) `single_imf`, (b) `binaries_50`, (c) `fiducial`, (d) `binaries_un`, (e) `binaries_th`, (f) `segregated`, and (g) `binaries_100`. Lines show stellar distances to the density center of the cluster, and colors show the mass of the individual star. Each line represents a single star, and, in the case of a binary, there is a thinner line inside the thicker line representing the trajectory of the companion, but only if the companion is also part of the 10 most massive stars; i.e., no more than 10 lines are shown in each panel. The shaded area is the region inside the half mass–radius of the cluster measured with respect to the initial mass.

green open circles). We show the values of $\Gamma_{\rm b,eff}$ at the beginning of the simulation as contour lines, where the labels are the corresponding values in units of $\rm Myr^{-1}$.

From Figure 7, we can define the typical binary as one with a total mass of $m_1 + m_2 \approx 0.2\,M_\odot$ and $E_{\rm bin} \approx 1\,M_\odot\ \rm km^2\ s^{-2}$. Such a binary has an interaction rate of $\Gamma_{\rm b,eff} \approx 0.01\ \rm Myr^{-1}$ in

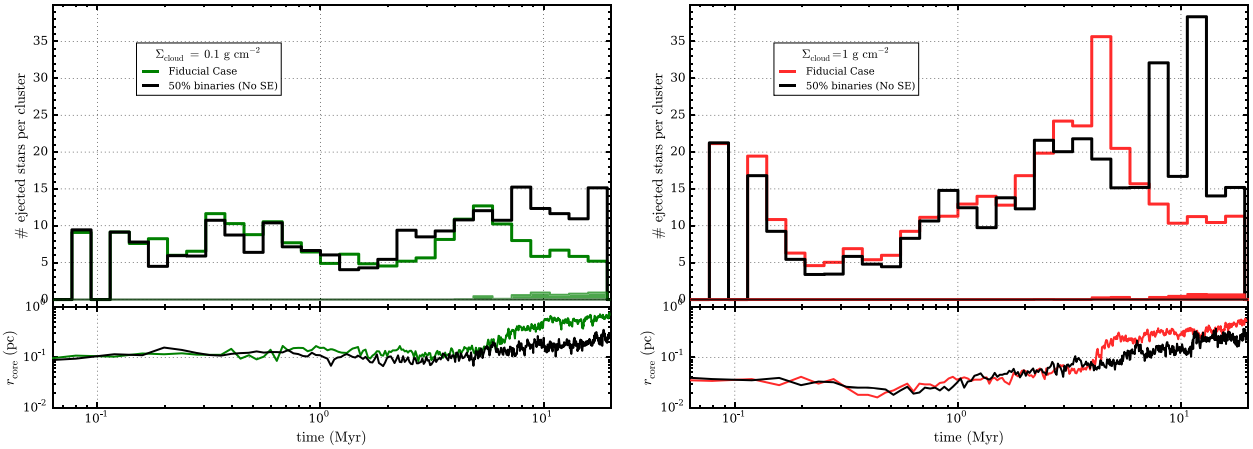

Figure 10. Number of strong dynamical ejections (see the text) per logarithmic time interval per cluster simulation for the set `fiducial` compared with the set without SE, `binaries_50`, for the low-Σ clump (left) and high-Σ clump (right). The shaded histograms show the ejections caused by supernova explosions. The bottom panels show the evolution of the average cluster core radii.

the low-Σ case and $\Gamma_{b,eff} \approx 0.2\,Myr^{-1}$ in the high-Σ case. These interaction rates are quite small and will fall quickly as the cluster expands. Massive binaries have higher interaction rates, as they attract other systems more efficiently; however, their binding energies are high, and their effective impact parameters become very small. Only binaries with the smallest binding energies have high enough interaction rates to be able to interchange energy effectively with the cluster. These stars are more likely to be low-mass stars.

There are several factors that determine how many interactions a binary will have during the simulations. If the binary is indeed perturbed, its binding energy will change and thus also its interaction rate. The environment may vary because of several factors—e.g., the expansion of the cluster, mass segregation, and binary fraction—and therefore it is quite complex to estimate the number of interactions a binary will have. However, we can use the results of our simulations and the initial $\Gamma_{b,eff}$ to calculate the probability that a binary will suffer at least one important interaction during the simulation. To do so, we measure the binding energy of all binaries at $t = 0$. At the end of the simulation, we calculate the binding energy of the binaries that have not been disrupted and compare it with their values at the start. We define "perturbed binaries" as those with a fractional change in energy of 1%.

We also measure $\Gamma_{b,eff}$ according to Equation (22), assuming the density and velocity values measured inside the half mass–radius of the cluster. Figure 8 shows the resulting histogram, where the value of each bin has been normalized by the total amount of (undisrupted) binaries in each bin. We constructed the histograms shown in Figure 8 by collecting all binaries from the 20 simulations performed for the set `fiducial`. We can see the correlation between the initial $\Gamma_{b,eff}$ and the probability of being perturbed. There is an offset in the relation for the different initial densities. For a given initial $\Gamma_{b,eff}$, the probability of suffering an encounter is higher in the low-Σ clusters. This seems counterintuitive; however, the rapid initial expansion of these clusters causes the initial $\Gamma_{b,eff}$ to be less representative, as it does not last long (see the number density evolution in Figure 5 for $t < 0.3$ Myr).

From all the perturbed binaries, we have also highlighted the cases in which the eccentricities suffered some modification ($\Delta e > 0.01$), and we display this probability as the shaded areas in Figure 8. The probability of modifying the initial eccentricity appears to increase linearly with $\Gamma_{b,eff}$ at first, but then it remains flat for higher binary interaction rates. Even stars with a high initial $\Gamma_{b,eff}$ have only an ≈30% chance of modifying their initial circular orbits ($e = 0$) into a slightly more eccentric orbit with $e = 0.01$. We have measured only a few rare cases in which the initial eccentricity increases by a significant factor.

Even though binaries with high $\Gamma_{b,eff}$ have a greater chance to interact and exchange energy with the cluster, these systems are very rare, as can be seen by the thin black lines of Figure 8, which show the total fraction of binaries in each $\Gamma_{b,eff}$ bin.

The variations in these effects between our considered models is small. The models with $f_{bin} = 1$ have a value of Γ_b that is a factor of 1.33 higher than that of the simulations with $f_{bin} = 0.5$ because of the effect on the number density of perturbing systems ($n_s \propto (1 + f_{bin})^{-1}$), and this difference becomes smaller when considering the effects of gravitational focusing. Models with initial mass segregation have central number densities about 10 times lower than those in the fiducial case, but they increase as the cluster evolves, until a point at which the few binary interactions that happen cause the cluster to expand relatively quickly. Note that most of the variables shown in Equation (19) tend to increase toward the cluster center. Especially in the case of the mass-segregated cluster, the mean mass per system is higher, which, according to Equation (19), is one of the most important parameters, since it strongly affects gravitational focusing. However, as the interactions in the center become important, the cluster expands faster; therefore, it is not possible to maintain high number densities.

If we assume that binaries are born as we have modeled them, i.e., with initially circular orbits, then to have significant modification of the orbits, such as eccentricities, requires a longer high-density phase, e.g., of several Myr. However, a longer timescale of cluster formation should not only keep the higher densities longer, it should also give more time for mass segregation, which can also boost interaction rates.

3.5. The Effect of Stellar Evolution

One important feature that can affect the evolution of cluster dynamics is SE, especially mass loss from winds and supernovae. En route to constructing our fiducial model set, we consider two sets with no SE, i.e., `single_imf` and `binaries_50`, the

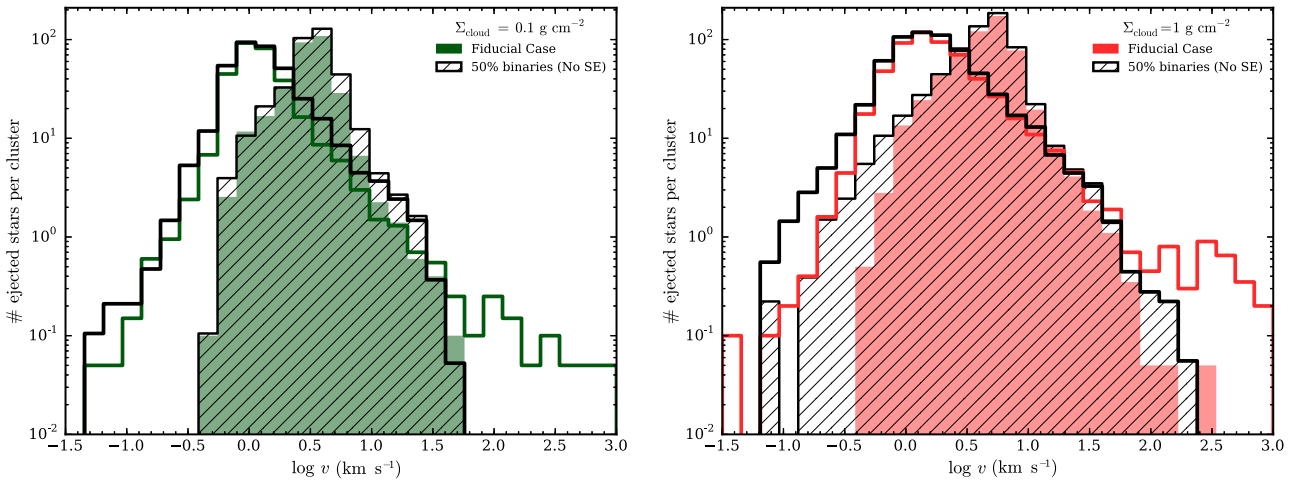

Figure 11. Velocity distribution of stars ejected dynamically in the `fiducial` set compared with ejected stars in the set with no SE, `binaries_50`. The left panel shows the low-Σ case, and the right panel shows the high-Σ simulations. The solid lines show the velocity distribution at 20 Myr (v_∞), while the shaded histograms show the distribution of velocities right after ejection (v_0).

latter only differing from the `fiducial` set by having SE turned off. We also show the total mass with respect to the initial as the shaded areas in the top panels of Figure 5, with a decrease by about 12% on average caused entirely by SE effects. Bound fractions at the end of the simulation in the `fiducial` set are $\simeq$0.55, compared to $\simeq$0.62 in the `binaries_50` runs. Thus, we see that the decrease in the bound mass fraction can, in fact, be explained entirely by the SE mass loss, rather than a significantly increased tendency for individual stellar members to be lost from the clusters.

Another way of losing mass from the cluster is due to the sudden ejection of the members of a binary system caused by a supernova explosion. After the supernova explodes, the binding energy suddenly drops, and the system may be broken (Zwicky 1957; Blaauw 1961). The stars, both the remnant of core collapse and the secondary star of the binary, may be ejected from the cluster as runaway stars. In this case, it is expected that the models with 100% binaries (`binaries_100`) will experience a higher loss of members, since all supernovae occur in binary systems. However, this has only a modest effect on the bound mass fraction, as shown in Figure 5. The orbital velocity of a 10 $M_\odot$ star in a typical binary is $\sim$0.3 km s^{-1} if it is in the peak of the period distribution, and it can vary from $\sim$0.001 to 50 km s^{-1} if we move one σ from the mean period. We find in our simulations that the mean escape velocity of the bound cluster varies from $\sim$7 to 0.6 km s^{-1} over the course of the simulation. Thus, it is not certain that a binary star will be ejected from the cluster due to binary disruption. However, we have also included velocity kicks due to asymmetric supernova explosions, with typical values of $\sim$100 km s^{-1}. This effect is the main factor responsible for ejections of the remnants of supernova explosions. The concomitant ejection of the secondaries will depend on the binary properties at the time of the supernova explosion, which for the models presented here depends mostly on primordial binary properties.

Figure 9 shows the radial trajectories of the 10 most massive stars in example simulations drawn from the sets of investigated models. Moving from panels (a) to (b), we see the effects of primordial binaries increasing the likelihood of dynamical ejection from an unstable multiple. Then, from panels (b) to (c), we see the effects of SE, especially the ejection of stars after supernova explosions. These types of ejections are more common than fast ejections resulting from the decay of unstable multiples. Varying the initial eccentricity distribution has only minor effects compared to the fiducial model. The fully mass-segregated case leads to the most extreme concentration of the 10 most massive stars in the core of the cluster. Having 100% binaries may also lead to a greater concentration of those massive stars that are bound in the cluster to its core. However, note that there is a large degree of variation caused by stochastic sampling of the IMF in the examples shown in Figure 9.

3.6. Ejected Stars and Kinematic Structure

We classify the stars into three main groups: (1) unbound stars, which are born unbound from the cluster because of the initial conditions, i.e., because of the loss of gravitational potential and confining pressure due to gas expulsion; (2) bound stars, which are the stars that are still bound at the end of the simulation; and (3) ejected stars, which become unbound during cluster evolution. Among the ejected stars, we identify three different mechanisms that can lead to ejection: (A) supernova ejection, either by the kick received to the core collapse remnant and/or by the disruption of a binary that contained the supernova progenitor (see Section 3.5); (B) dynamical ejection, due to the decay of unstable triple or higher-order multiple systems or to slingshot super-elastic encounters, which leave behind a more tightly bound binary or multiple; and (C) gentle ejection, where a star finds itself unbound as a result of the global evolution of the cluster potential.

In order to obtain detailed information about the ejection events, we identify bound members in the simulations snapshot by snapshot, recording information about the stars the first time they appear unbound and comparing with the previous output time. We also record their positions and velocities at the end of the simulation.

We are especially interested in "strong" dynamical ejections that lead to relatively fast ejection velocities from the cluster, and we identify such stars as having $\Delta T_i/\Delta\Omega_i \geqslant 2$ from the previous time output. Such stars will be easier to identify in proper-motion studies of young clusters.

Figure 10 shows the number of such strong ejection events, including supernova ejections, per cluster per logarithmic time

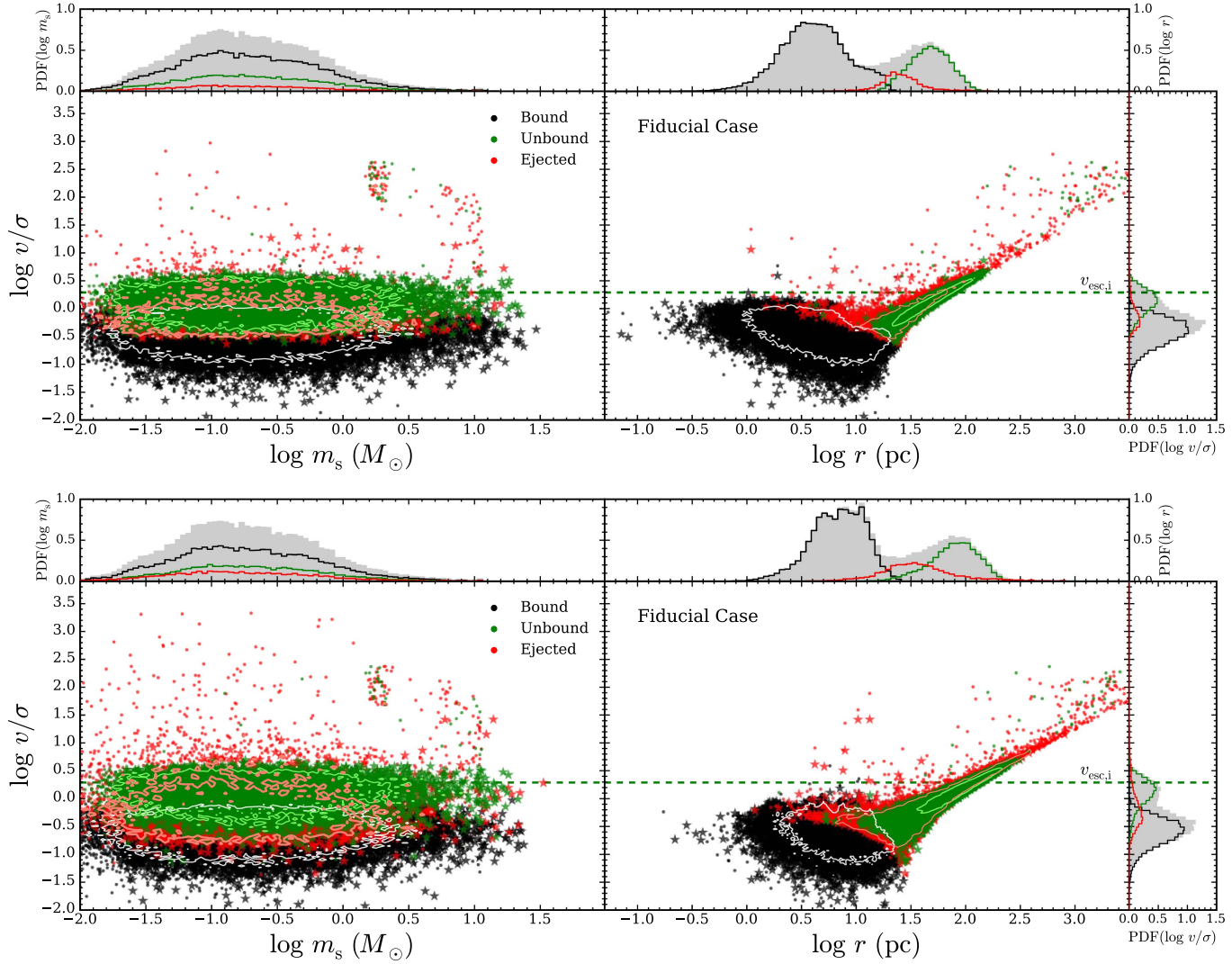

Figure 12. Normalized velocity vs. mass (left panels) and vs. distance (right panels) for all stars in the fiducial case for simulations with $\Sigma_{\rm cloud} = 0.1$ g cm^{-2} (top) and $\Sigma_{\rm cloud} = 1$ g cm^{-2} (bottom). Stars are separated into three groups: bound stars (black), stars born unbound (green), and ejected stars (red). Different symbols indicate whether the star is a single (filled circles) or a binary (filled stars). Velocity values are normalized by the mass average velocity dispersion of the parent clump (see Table 1). Small top and side panels show the PDFs considering all stars in the set (gray shaded area) and the fraction of the PDFs that correspond to each group of stars (lines). The escape velocity from the stellar cluster at its surface at the start of the simulation is shown by a green dashed line. In order to show some of the structure hiding in the cloud of points, contours that contain 90% of the stars in each set are shown in a lighter color, i.e., white for bound, light green for unbound, and light red for ejected.

interval. We compare simulations with (`fiducial`) and without (`binaries_50`) SE for the two different initial Σ cases.

As expected, a high initial $\Sigma_{\rm cloud}$ leads to bound clusters with smaller core radii and thus results in a larger rate of strong dynamical ejections than in the low-Σ case. Another difference is the number of ejections after SE becomes relevant. The number of massive stars in the cluster decreases significantly after the first supernova explosions and resulting ejections. Massive stars are likely to be near the cluster center; therefore, supernova explosions lead to a drop in the central density of the cluster that has a direct effect on the subsequent number of dynamical ejections, as can be seen in the anticorrelation with core radius. Cases without SE show a constant decrease in their rate of dynamical ejection events (i.e., a flat distribution in equally logarithmically spaced time bins), while in cases with SE, the decrease becomes steeper after the first supernova.

We also have information about the velocities right after ejection (v_0) and at the end of the simulation (v_∞). We show the corresponding distributions in Figure 11 with shaded areas for v_0 and solid lines for v_∞. As expected, low-velocity stars show a more significant relative decrease in their velocities due to their transit out of the cluster potential. We also notice a high-velocity tail of stars appearing in the fiducial case with SE; these are the result of the dynamical ejection of massive stars, which later explode as supernovae resulting in a secondary kick for their remnants and any binary companions. Such a two-step ejection scenario has been proposed by Pflamm-Altenburg & Kroupa (2010; see also Gvaramadze et al. 2008) and has been argued to explain some O-type runaway stars and remnants with no apparent origin cluster (an alternative could be isolated massive star formation), as well as the rare observed cases of hyperfast runaways with velocities above 1000 km s^{-1} (e.g., as

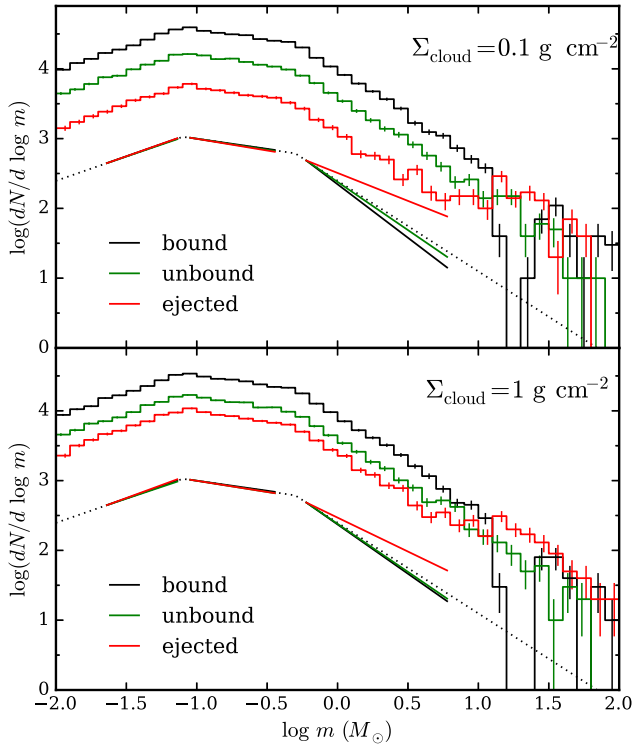

Figure 13. Collected IMFs for all the stars in the fiducial case separated as bound (black), unbound (green), and ejected (red) stars, as in Figure 12. The top panel shows the simulations with $\Sigma_{\rm cloud} = 0.1$ g cm^{-2}, and the bottom panel shows the simulations with $\Sigma_{\rm cloud} = 1$ g cm^{-2}. Lines below the steps show the shape of the best fit on each range of masses for each group of stars overplotted on the canonical IMF used as the initial condition for comparison. In all groups, the IMF below 0.5 $M_\odot$ is the same and does not change from the original, but the group of ejected stars shows a top-heavy IMF.

in Chatterjee et al. 2005) (an alternative could be interaction with the supermassive black hole in the Galactic center).

Out of all of the ejected O-type stars in our models, i.e., stars more massive than 16 $M_\odot$, 35% and 22% of them were ejected dynamically in the low- and high-Σ cases, respectively. While in the same order, 24% and 33% of them were ejected because of supernova explosions, and the remaining 41% and 45% were gentle ejections caused by the drop in the cluster potential or "weak" dynamical ejections (i.e., $\Delta T_i/\Delta\Omega_i < 2$). We expect that these numbers will change when more realistic models of gradual star cluster formation are considered, since these are likely to lead to different cluster core densities.

Figure 12 shows the normalized velocity versus mass (left panels) and normalized velocity versus radial distance from the cluster center (right panels) for all the stars in the simulations of the `fiducial` set (see Figures 15 and 16 in the Appendix for the same plots for other sets) with low (top panels) and high (bottom panels) values of $\Sigma_{\rm cloud}$. Velocities are normalized by the mass average velocity dispersion of the parent clump (see σ in Table 1 and Equation (9)). Masses show the final masses of the single stars (filled circles) or combined binaries (filled stars).

With the exception of massive stars undergoing supernova explosions, unbound stars (green symbols) do not change their velocities significantly on leaving the cluster. They have a peak on the PDF at σ, below the initial mean escape velocity of the cluster, $v_{\rm esc,i}$, shown by a green dashed line in Figure 12. Figure 15 shows that the width of the velocity PDF of unbound stars is quite constant over all the different simulation sets.

Ejected stars have a velocity PDF that peaks between those of the unbound and bound stars. This is because the escape velocity decreases with time as the cluster expands and loses members. As discussed earlier, a cluster born in a denser state expands more quickly, and, at 20 Myr, its half mass–radius is about 10 times larger than that of the same cluster born in a lower density state. This leads to a larger relative decrease in the mean escape speed of the cluster over the 20 Myr of evolution followed by these simulations, compared to the low-Σ case. This, in turn, causes a broadening of the ejected star velocity PDF. Otherwise, the widths of the velocity PDFs do not vary much between simulation sets.

Bound and unbound stars are more clearly distinguished in the velocity versus radial distance diagram. Bound stars have, in general, higher velocities at the center of the cluster and lower velocities at the outskirts. They thus populate different areas from the unbound and ejected stars: the higher velocities of these stars carry them further from the cluster, and the distance from the cluster is modulated also by the time when they were ejected. Supernova-induced velocity kicks also lead to the modification of a small fraction of stars in this diagram. The group of neutron stars seen in the velocity-mass diagram is another manifestation of such effects. Their velocities are a direct result of the assumed Maxwellian distribution for supernova-induced kick velocities with σ=265 km s^{-1}.

Figure 13 shows the IMF of the three different classes of stars: bound, unbound, and ejected. The IMF of the unbound group (green histogram) mirrors the assumed primordial distribution; stars from all masses are initially randomly distributed and are equally likely to be born unbound. The initially bound cluster shows the same pattern; however, as the cluster evolves and stars are ejected, almost all of the massive stars are lost, resulting in the black histogram shown in Figure 13. Thus, the IMF of the ejected group (red histogram) shows a clear signature of being top heavy —mostly a consequence of SE. Eventually, a large majority of the stars that are able to explode as supernovae are ejected from the cluster. When comparing with other simulation sets (see Figure 17), we see that, even before including SE, the IMF of the ejected stars is already top heavy, which is a result only of dynamical ejections. However, this effect is not strong enough to significantly change the shape of the bound cluster IMF.

Further variations from the set `fiducial` do not change these results significantly, with the exception of the `segregated` sets. Initial extreme mass segregation causes a very different evolution in the three groups of stars. Stars born unbound are preferentially the lowest-mass stars; therefore, the initially bound clusters have top-heavy IMFs. Later evolution causes the cluster to lose its massive stars. However, such extreme mass segregation is a very idealized model that is not expected to be a very realistic description of observed clusters.

3.7. Radial Structure

We now summarize the evolution of various radial distributions of stellar properties in the clusters, which, in their projected forms, are one of the most direct observables of real systems (see Figure 14 for results for the `fiducial` set of simulations and Figures 18 and 19 in the Appendix for the other sets). For the low- and high-$\Sigma_{\rm cloud}$ cases, we show the radial profiles for volume density (panels (a) and (b)), projected mass surface density (panels (c) and (d)), projected one-dimensional velocity dispersion $\sigma_{\rm 1D}$ (panels (e) and (f)), and projected mean stellar mass $\langle m_{\rm i}\rangle$ (panels (g) and (h)).

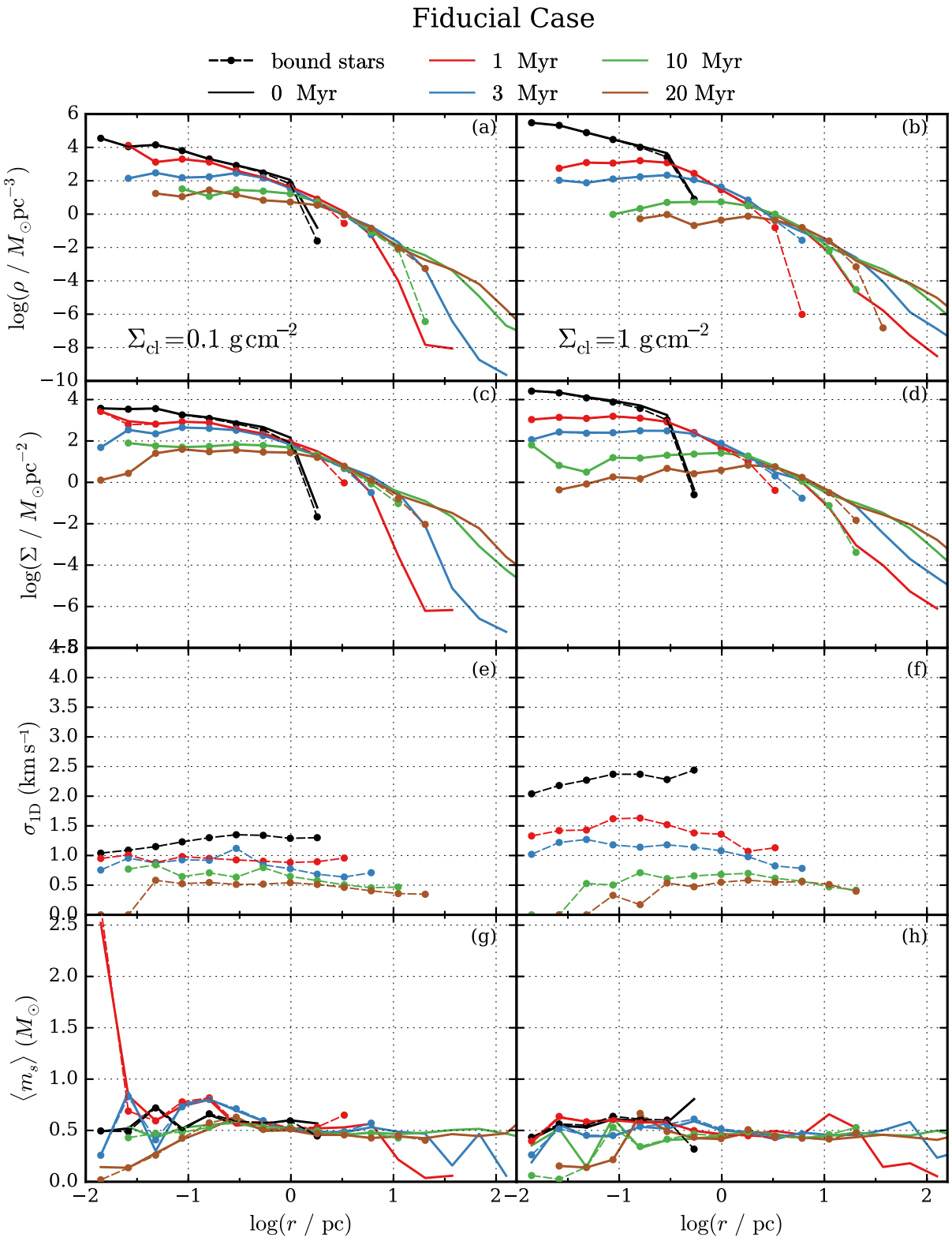

Figure 14. Radial profiles of the fiducial simulations at 0 Myr (black), 1 Myr (red), 3 Myr (blue), 10 Myr (green), and 20 Myr (brown), with results for the low-$\Sigma_{\rm cloud}$ shown in the left column and the high-$\Sigma_{\rm cloud}$ in the right column. Dashed lines and circles show the mean values of the 20 realizations for the bound clusters, while solid lines show these averages for the total stellar population. Panels (a) and (b): stellar volume density radial profile as a function of spherical radial coordinates from cluster center. Panels (c) and (d): mass surface density profile as a function of projected radial coordinates from cluster center. Panels (e) and (f): one-dimensional velocity dispersion profile as a function of projected radius. Panels (g) and (h): average mass per system profile as a function of projected radius. Note that in panels (e) and (f), $\sigma_{\rm 1D}$ for all stars has been omitted because of the large variations caused by runaway stars. Note also that binary stars are treated as unresolved systems; i.e., we use their combined mass, position, and velocity to construct each profile.

These figures show the expansion of the clusters and the flattening of the initial power-law density profile, i.e., development of a constant density core. Stars born unbound separate from the cluster as it evolves and appear as an excess "halo" around the bound cluster.

As expected, the velocity dispersion profiles of the bound stars show a general trend of evolving toward smaller values as the clusters expand. This can also be seen in Figure 5 with a similar evolution for all the different simulation sets. The velocity profiles are relatively flat but with a modest tendency to decrease in the outer regions.

Panels (g) and (h) of Figure 14 show the average stellar mass per system; i.e., the masses of binary stars are combined. By this metric, we do not see significant signatures of mass segregation developing in the clusters. At later times, SE, i.e., wind mass loss and supernovae, acts to remove massive stars. Stochastic effects due to IMF sampling are still noticeable, even when averaging over 20 clusters.

The most extreme primordially segregated case we considered (set `segregated`) is able to maintain its mass segregation for much of the 20 Myr evolution (note that stars born unbound are mostly low-mass stars), but it becomes less prominent in the high-Σ case, since massive stars are ejected more efficiently by dynamical interactions. After 3 Myr, massive stars start to be lost due to SE (supernova) effects.

4. Discussion and Conclusions

We have presented a first modeling of the dynamical evolution of star clusters forming with initial conditions prescribed by the turbulent clump model of McKee & Tan (2003). These initial conditions involve idealized descriptions of star-forming protocluster clumps as singular polytropic spheres in virial equilibrium (including effects of large-scale magnetic field support) and pressure equilibrium with a surrounding cloud medium (i.e., the clump radius is set by truncation of the polytropic sphere where the local clump pressure matches the ambient cloud pressure, with the latter assumed to be due to the self-gravitating weight of the larger-scale cloud of a given mass surface density, $\Sigma_{\rm cloud}$). In this first paper, we have assumed, for simplicity, that star clusters are formed instantaneously with a spatially uniform SFE. Subsequent papers will build realism into this model, in particular allowing for the effects of gradual star formation.

The first consequence of the above assumptions is that stars follow the spatial and kinematic distributions of the parent clump, which sets the main difference between this and previous related studies in which velocity profiles of the star clusters are constructed either using isotropic velocity distributions, using the methods described by Aarseth et al. (1974) (e.g., Goodwin & Bastian 2006), or assuming that the stars are in equilibrium with their natal gas at the onset of gas expulsion (e.g., Baumgardt & Kroupa 2007). A system in equilibrium has a velocity dispersion profile that decreases with radius. The turbulent clump model, however, involves larger velocity dispersions at larger scales, so stars born on the outskirts of the clump are less likely to remain bound to the cluster. Conversely, these models contain a central, relatively tightly bound central region.

One crucial parameter that determines the amount of retained mass after the gas is expelled in this model is the contribution of magnetic fields to the support of the parent clump. Without magnetic field support, the virial ratios at the onset of gas expulsion are relatively high even for an SFE of 100%. We can infer from our results that, without magnetic fields, a 100% SFE would result in clusters that retain only $\sim$40% of the stars (see Figures 1 and 2). However, the models presented here are the worst-case scenario in terms of cluster survivability. It has been shown that gradual gas expulsion increases the amount of stellar mass retained (e.g., Mathieu 1983; Baumgardt & Kroupa 2007; Smith et al. 2013a). Another factor is the central star–to–gas mass ratio at the onset of gas expulsion (e.g., Kruijssen et al. 2012). Our models have assumed a spatially uniform SFE, but the local SFE may be raised either by dynamical cluster relaxation before gas expulsion (Smith et al. 2011; Farias et al. 2015) or by the star formation process itself, which has been argued to be faster and globally more efficient in the densest regions of the clump (Kruijssen 2012; Kruijssen et al. 2012; Parmentier & Pfalzner 2013).

The fiducial clusters that we have simulated show rapid expansion, even just considering their bound members. For example, the half-mass radii show dramatic (factors of several) expansion after 1 Myr, especially in the $\Sigma_{\rm cloud} = 1$ g cm^{-2} case. Thus, for these models to explain observed young star clusters of a given age, mass, and mass surface density (see, e.g., Figure 1 of Tan et al. 2014) would require initial clumps that have mass surface densities at least 10 times greater. There is limited evidence for such dense starless clumps (Tan et al. 2014; see also Walker et al. 2016). This may indicate that some aspect of the model needs to be modified, such as the assumption of instantaneous star formation and gas expulsion.

Another feature of our work has been the full treatment of binaries, given assumed primordial binary properties. The processing of these binaries during the early phases of the dynamical evolution of star clusters can be a diagnostic of the process, i.e., by comparing their properties with observed field star and embedded cluster binary properties. We have also seen that binaries affect some aspects of the dynamical evolution of the cluster, in particular by enhancing the rate of dynamical ejection of stars. We consider that our main results on this topic so far are to show the relative importance of binaries in our model clusters depending on their input assumptions. In the clusters that we have investigated in this paper, there has been relatively little processing of the average initial binary properties, given the fairly rapid expansion of the clusters from their initial dynamical states. These results provide a baseline for comparison of future models of gradual star cluster formation.

Since we have a full treatment of binaries and SE, we are also able to make predictions for the properties of ejected stars, including via dynamical ejection from unstable triples and higher-order multiples and from supernova explosions. The models presented here are only able to reproduce high-velocity runaway stars by supernova kicks. Only the densest initial conditions lead to dynamical ejection of stars at speeds >100 km s^{-1} (but less than one per cluster), and we have not obtained dynamical ejection of any massive stars at speeds >20 km s^{-1}. This probably again indicates a need for more gradual models of star formation that retain a dense cluster core for a larger number of crossing times.

In the context of our presented models that apply in the limit of fast, i.e., "instantaneous," star cluster formation, our main conclusions are:

1. Magnetic fields that partially support the parent clump against collapse are a key factor that determines the initial velocity and bound mass of the newborn cluster. Star clusters born from clumps with no magnetic field support would need a very high SFE (>80%) to retain a significant part of the stellar mass after the gas is expelled.

2. Regardless of the different initial surface densities, the mass of the bound cluster that emerges from its natal gas is determined by the SFE. However, the expansion rate of the unbound stellar population is determined by the typical internal velocity of the parent clump. This means that clusters born in high-mass surface density environments will produce unbound populations that expand more rapidly than those produced from clusters formed in low-mass surface density environments.
3. The rapid early expansion of the bound clusters implies that at least $\sim 10\times$ higher mass surface density starless clumps are needed to explain observed young ($\sim$1 Myr old) clusters that have stellar mass surface densities $\gtrsim 0.1$ g cm^{-2}, but there is limited evidence for such clumps. This may indicate a need for more gradual models of star cluster formation.
4. The low interaction rates of binaries in our simulated clusters lead to only minor modifications of the average initial binary properties. If star cluster formation is rapid, then the present-day observed binary properties have not changed much from their primordial distributions, except for those effects induced by SE.
5. Based on velocity–position diagrams, it is possible to distinguish the bound cluster from the unbound stars, and we expect that this is made easier if gas is expelled quickly. Such diagrams also give us information on the initial properties of the parent clump, such as the initial escape velocity from the cluster.
6. High-velocity runaway stars in the clusters simulated so far are mostly due to supernova explosions that disrupt binaries. Such statistics likely indicate, again, that star cluster formation does not proceed in such a rapid manner.

It remains to be determined how the above metrics will vary for models of star clusters forming from turbulent clumps that involve gradual formation of stars and gradual gas expulsion. In addition, correlated spatial and kinematic substructures associated with turbulence and potential infalling accretion flows need to be incorporated into these models. Variations in global geometry, e.g., elongation of the clump into more filamentary configurations, also need to be explored. A wider range of initial conditions of clump properties and assumed star formation efficiencies, primordial mass segregation, and primordial binary properties needs to be investigated for this model family. By an eventual comparison of model results with observed kinematic properties of young clusters, we hope to constrain star and star cluster formation theories.

We thank Nicola Da Rio and Antonio Ordoñez for helpful discussions. We acknowledge support from *Hubble Space Telescope* Cycle 23 Theory Grant 14317, *The Orion Experiment* (PI: Tan).

Appendix
Ancillary Results for the Full Set of Simulations

In this Appendix we provide the results for the set of simulations with SFE = 50%, but that differ from the fiducial case in some other respects (see Table 2). Figures 15 and 16 shows the mass/position–velocity diagrams for the low and high Σ cases, respectively, analogous to Figure 12. Figure 17 shows the corresponding IMFs for both Σ cases constructed in the same way as in Figure 13. Figures 18 and 19 show the corresponding radial profiles comparing both Σ cases in the same way as in Figure 14.

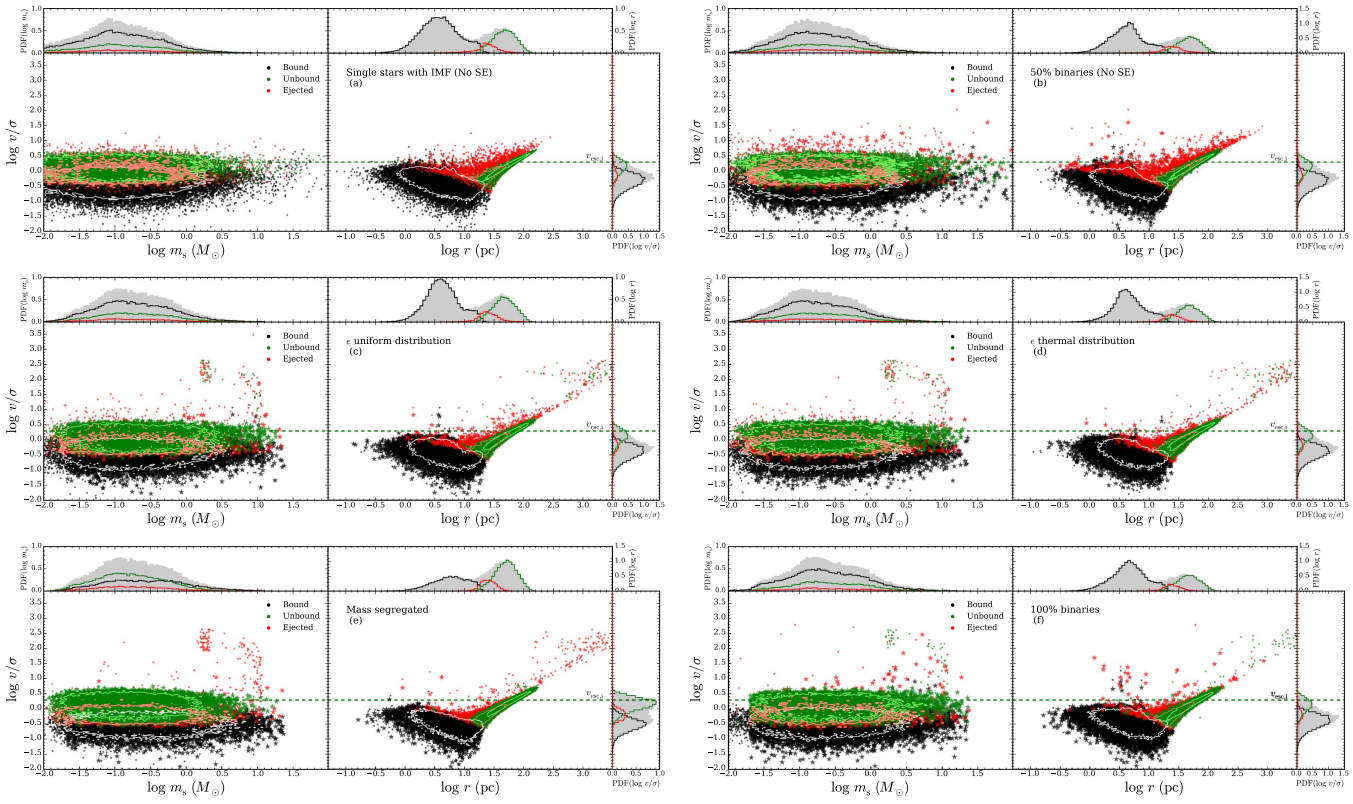

Figure 15. Same as Figure 12, but for simulation sets: (a) `single_imf`, (b) `binaries_50`, (c) `binaries_un`, (d) `binaries_th`, (e) `segregated`, and (f) `binaries_100`, all with $\Sigma_{\rm cloud} = 0.1$ g cm^{-2}.

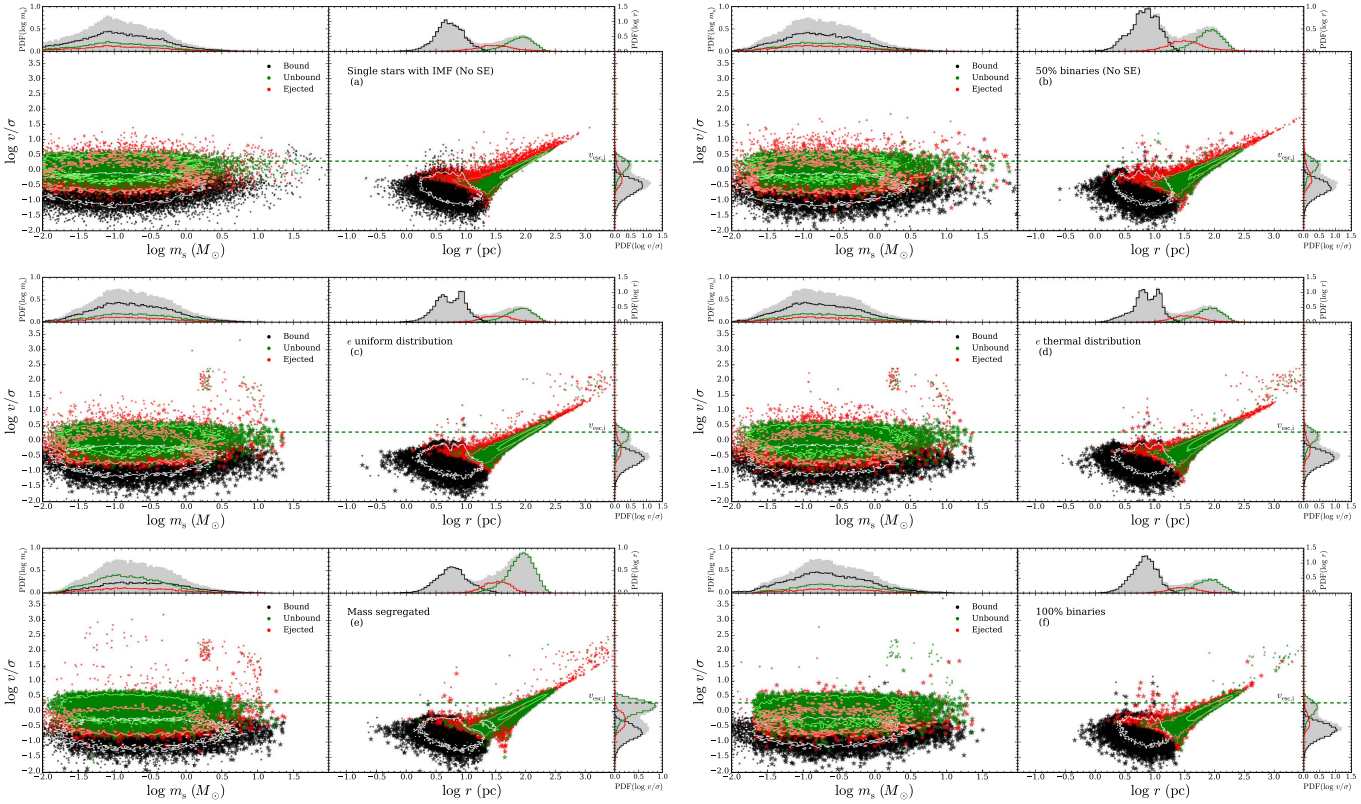

Figure 16. Same as Figure 15, but for simulations with $\Sigma_{\rm cloud} = 1$ g cm^{-2}.

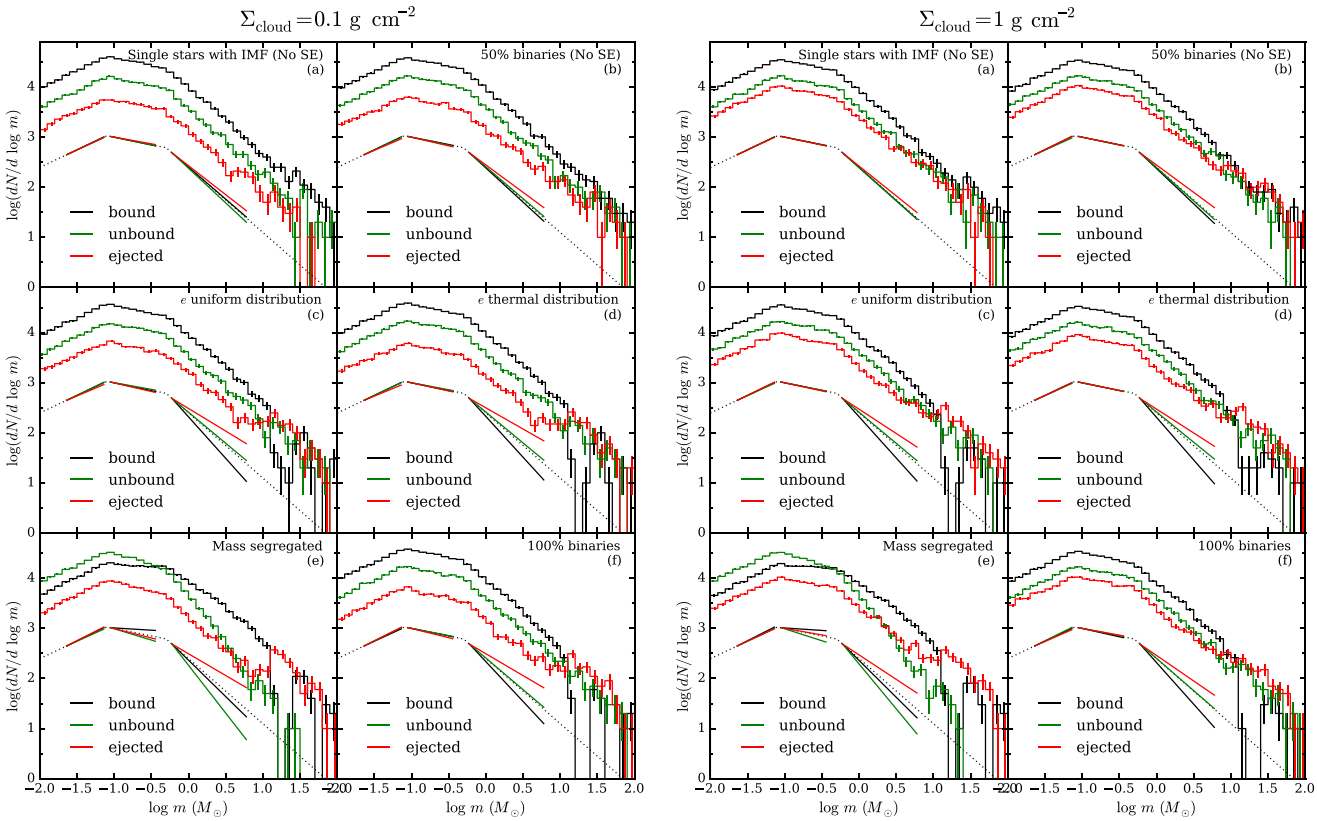

Figure 17. Same as Figure 13, but for simulations with $\Sigma_{\rm cloud} = 0.1$ g cm^{-2} (left set of panels) and $\Sigma_{\rm cloud} = 1$ g cm^{-2} (right set of panels). Labeled panels show the IMFs for the simulation sets: (a) `single_imf`, (b) `binaries_50`, (c) `binaries_un`, (d) `binaries_th`, (e) `segregated`, and (f) `binaries_100`.

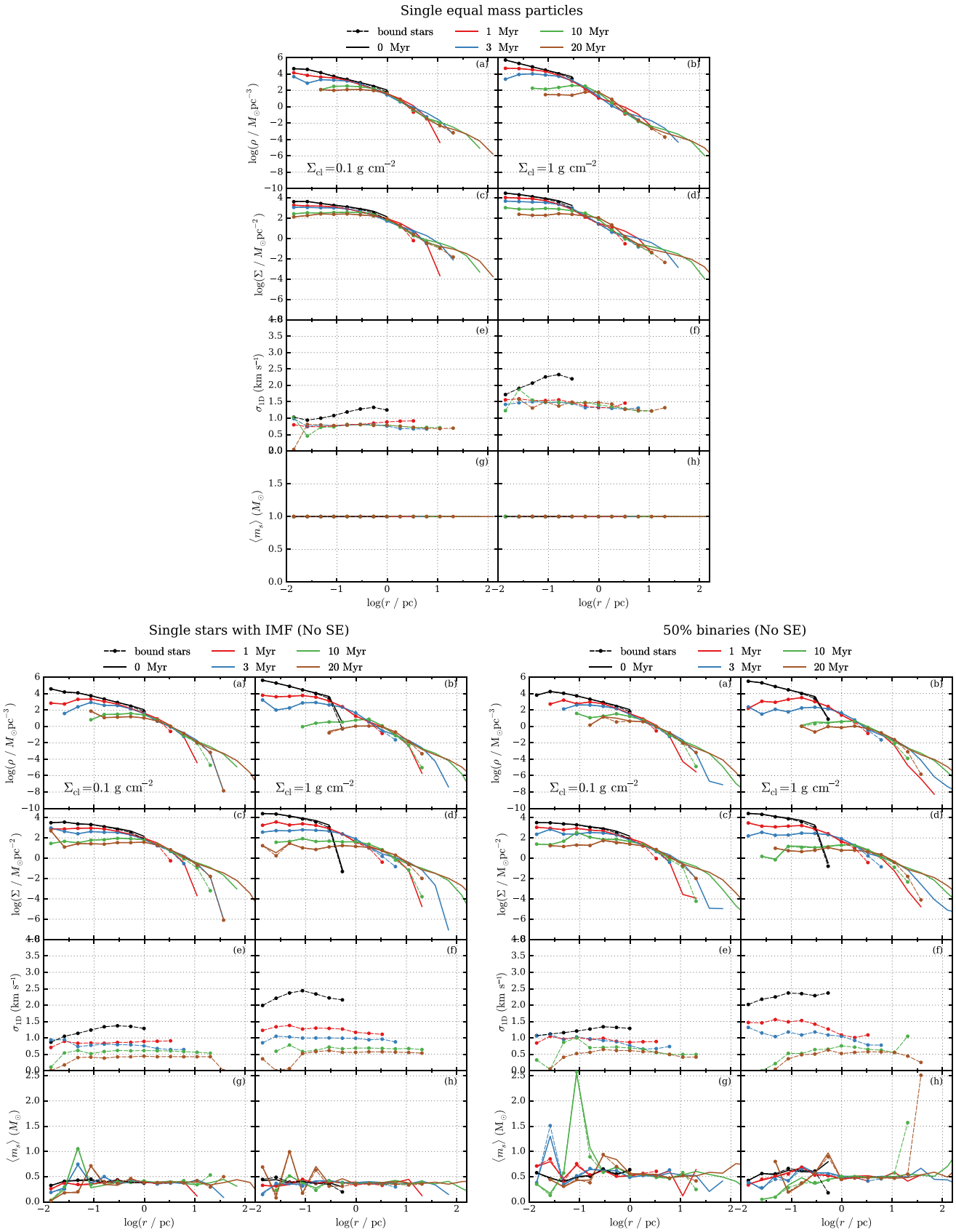

Figure 18. Same as Figure 14, but showing radial profiles for sets `equal_mass` (top), `single_imf` (bottom left), and `binaries_50` (bottom right), all with no SE.

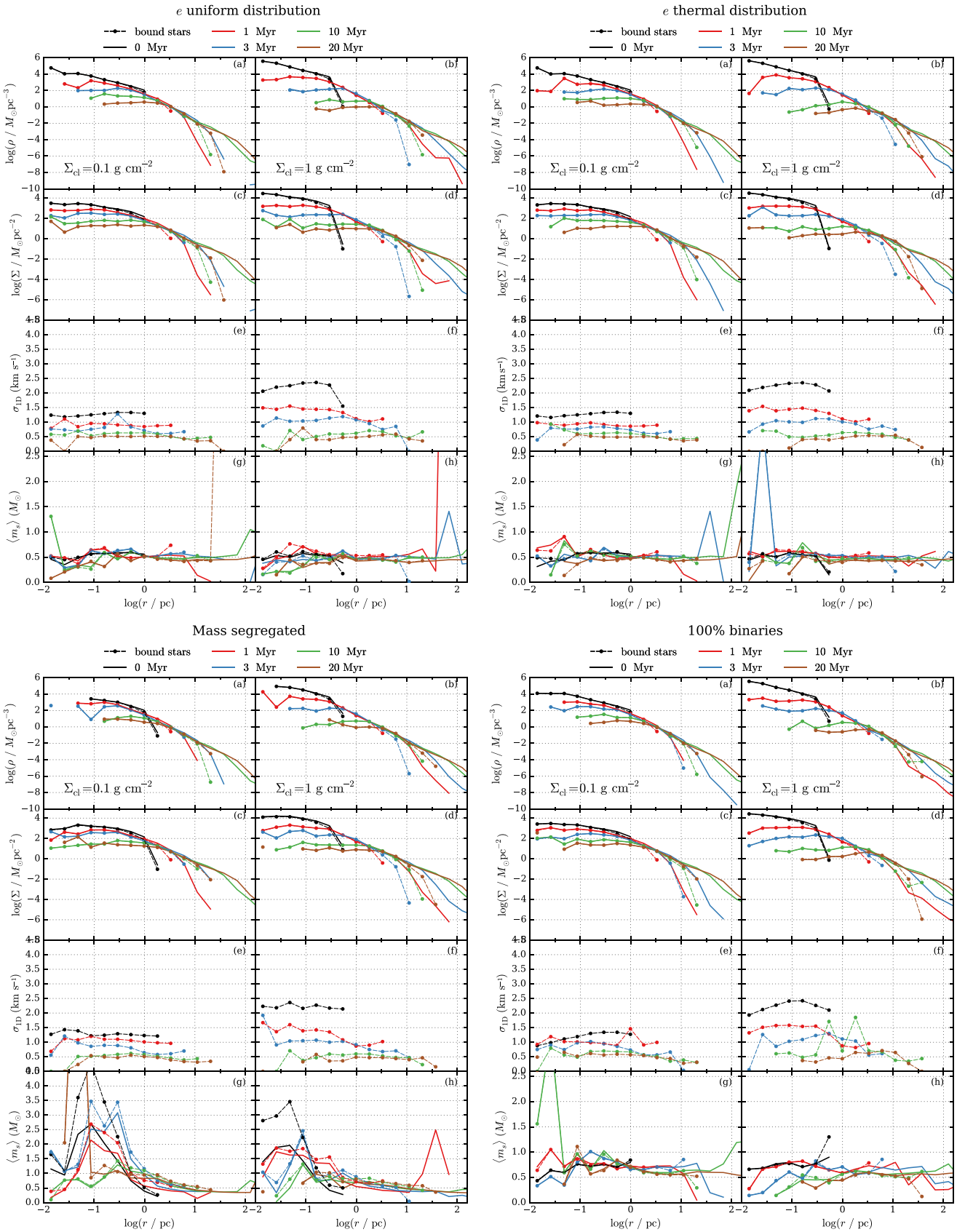

Figure 19. Same as Figure 14, but for simulations with SE turned on. The top panels show simulations with different eccentricity distributions, `binaries_un` (top left) and `binaries_th` (top right), and the bottom panels show the most extreme cases: the set with primordial mass segregation, `segregated` (bottom left), and the case with 100 binaries, `binaries_100` (bottom right).

References

Aarseth, S. J. 2003, Gravitational N-Body Simulations (Cambridge: Cambridge Univ. Press)
Aarseth, S. J., & Heggie, D. C. 1998, MNRAS, 297, 794
Aarseth, S. J., Henon, M., & Wielen, R. 1974, A&A, 37, 183
Banerjee, S., & Kroupa, P. 2015, arXiv:1512.03074
Basri, G., & Reiners, A. 2006, AJ, 132, 663
Bastian, N., & Goodwin, S. P. 2006, MNRAS, 369, L9
Baumgardt, H., & Kroupa, P. 2007, MNRAS, 380, 1589
Blaauw, A. 1961, BAN, 15, 265
Boily, C. M., & Kroupa, P. 2003, MNRAS, 338, 673
Brinkmann, N., Banerjee, S., Motwani, B., & Kroupa, P. 2016, arXiv:1611.05871
Butler, M. J., & Tan, J. C. 2009, ApJ, 696, 484
Butler, M. J., & Tan, J. C. 2012, ApJ, 754, 5
Chatterjee, S., & Tan, J. C. 2012, ApJ, 754, 152
Chatterjee, S., Vlemmings, W. H. T., Brisken, W. F., et al. 2005, ApJL, 630, L61
Chen, H.-C., & Ko, C.-M. 2009, ApJ, 698, 1659
Close, L. M., Siegler, N., Freed, M., & Biller, B. 2003, ApJ, 587, 407
Dale, J. E., Ercolano, B., & Bonnell, I. A. 2015, MNRAS, 451, 987
Duquennoy, A., & Mayor, M. 1991, A&A, 248, 485
Elmegreen, B. G. 2000, ApJ, 530, 277
Elmegreen, B. G. 2007, ApJ, 668, 1064
Farias, J. P., Smith, R., Fellhauer, M., et al. 2015, MNRAS, 450, 2451
Fischer, D. A., & Marcy, G. W. 1992, ApJ, 396, 178
Geyer, M. P., & Burkert, A. 2001, MNRAS, 323, 988
Ginsburg, A., Bressert, E., Bally, J., & Battersby, C. 2012, ApJL, 758, L29
Goodwin, S. P., & Bastian, N. 2006, MNRAS, 373, 752
Gutermuth, R. A., Megeath, S. T., Myers, P. C., et al. 2009, ApJS, 184, 18
Gvaramadze, V. V., Gualandris, A., & Portegies Zwart, S. 2008, MNRAS, 385, 929
Hartmann, L., & Burkert, A. 2007, ApJ, 654, 988
Heggie, D. C. 1975, MNRAS, 173, 729
Hills, J. G. 1975, AJ, 80, 809
Hobbs, G., Lorimer, D. R., Lyne, A. G., & Kramer, M. 2005, MNRAS, 360, 974
Hurley, J. R., Pols, O. R., & Tout, C. A. 2000, MNRAS, 315, 543
Hurley, J. R., Tout, C. A., & Pols, O. R. 2002, MNRAS, 329, 897
Kaczmarek, T., Olczak, C., & Pfalzner, S. 2011, A&A, 528, A144
Kouwenhoven, M. B. N., Goodwin, S. P., Parker, R. J., et al. 2010, MNRAS, 404, 1835
Kroupa, P. 2001, MNRAS, 322, 231
Kroupa, P., & Burkert, A. 2001, ApJ, 555, 945
Kroupa, P., Petr, M. G., & McCaughrean, M. J. 1999, NewA, 4, 495
Kruijssen, J. M. D. 2012, MNRAS, 426, 3008
Kruijssen, J. M. D., Maschberger, T., Moeckel, N., et al. 2012, MNRAS, 419, 841
Lada, C. J., Margulis, M., & Dearborn, D. 1984, ApJ, 285, 141
Ma, B., Tan, J. C., & Barnes, P. J. 2013, ApJ, 779, 79
Mason, B. D., Gies, D. R., Hartkopf, W. I., et al. 1998, AJ, 115, 821
Mathieu, R. D. 1983, ApJL, 267, L97
McKee, C. F., & Ostriker, E. C. 2007, ARA&A, 45, 565
McKee, C. F., & Tan, J. C. 2003, ApJ, 585, 850
Myers, A. T., Klein, R. I., Krumholz, M. R., & McKee, C. F. 2014, MNRAS, 439, 3420
Nakamura, F., & Li, Z.-Y. 2007, ApJ, 662, 395
Nakamura, F., & Li, Z.-Y. 2014, ApJ, 783, 115
Padoan, P., Haugbølle, T., & Nordlund, Å. 2012, ApJL, 759, L27
Padoan, P., Haugbølle, T., & Nordlund, Å. 2014, ApJ, 797, 32
Parker, R. J., Goodwin, S. P., & Allison, R. J. 2011, MNRAS, 418, 2565
Parker, R. J., Goodwin, S. P., Kroupa, P., & Kouwenhoven, M. B. N. 2009, MNRAS, 397, 1577
Parker, R. J., & Meyer, M. R. 2014, MNRAS, 442, 3722
Parker, R. J., Wright, N. J., Goodwin, S. P., & Meyer, M. R. 2014, MNRAS, 438, 620
Parmentier, G., & Pfalzner, S. 2013, A&A, 549, A132
Pfalzner, S., & Kaczmarek, T. 2013, A&A, 555, A135
Pfalzner, S., Vincke, K., & Xiang, M. 2015, A&A, 576, A28
Pflamm-Altenburg, J., & Kroupa, P. 2010, MNRAS, 404, 1564
Preibisch, T., Balega, Y., Hofmann, K.-H., Weigelt, G., & Zinnecker, H. 1999, NewA, 4, 531
Price, D. J., & Bate, M. R. 2009, MNRAS, 398, 33
Proszkow, E.-M., & Adams, F. C. 2009, ApJS, 185, 486
Raghavan, D., McAlister, H. A., Henry, T. J., et al. 2010, ApJS, 190, 1
Rathborne, J. M., Jackson, J. M., & Simon, R. 2006, ApJ, 641, 389
Reggiani, M. M., & Meyer, M. R. 2011, ApJ, 738, 60
Schuller, F., Menten, K. M., Contreras, Y., et al. 2009, A&A, 504, 415
Smith, R., Fellhauer, M., Goodwin, S., & Assmann, P. 2011, MNRAS, 414, 3036
Smith, R., Goodwin, S., Fellhauer, M., & Assmann, P. 2013a, MNRAS, 428, 1303
Smith, R., Sánchez-Janssen, R., Fellhauer, M., et al. 2013b, MNRAS, 429, 1066
Tan, J. C., Beltrán, M. T., Caselli, P., et al. 2014, in Protostars and Planets VI, ed. H. Beuther et al. (Tucson, AZ: Univ. Arizona Press), 149
Tan, J. C., Kong, S., Butler, M. J., Caselli, P., & Fontani, F. 2013, ApJ, 779, 96
Tan, J. C., Krumholz, M. R., & McKee, C. F. 2006, ApJL, 641, L121
Tutukov, A. V. 1978, A&A, 70, 57
Walker, D. L., Longmore, S. N., Bastian, N., et al. 2016, MNRAS, 457, 4536
Wang, L., Spurzem, R., Aarseth, S., et al. 2015, MNRAS, 450, 4070
Zwicky, F. 1957, Morphological Astronomy (Berlin: Springer)

Paper *II*

Star Cluster Formation from Turbulent Clumps. II. Gradual Star Cluster Formation

Juan P. Farias, Jonathan C. Tan & Sourav Chatterjee

Preparing for submission to The Astrophysical Journal

DRAFT VERSION APRIL 29, 2018
Preprint typeset using LaTeX style emulateapj v. 01/23/15

STAR CLUSTER FORMATION FROM TURBULENT CLUMPS. II. GRADUAL STAR CLUSTER FORMATION

JUAN P. FARIAS[1,⋆], JONATHAN C. TAN[1,2], AND SOURAV CHATTERJEE[3]
[1]Dept. of Space, Earth & Environment, Chalmers University of Technology, Gothenburg, Sweden
[2]Dept. of Astronomy, University of Virginia, Charlottesville, VA 22904, USA
[3]Center for Interdisciplinary Exploration & Research in Astrophysics (CIERA) Physics & Astronomy, Northwestern University, Evanston, IL 60202, USA
Draft version April 29, 2018

ABSTRACT

We investigate the dynamical evolution of star clusters during their formation, assuming that they form from a turbulent starless clump of a given mass within a parent self-gravitating molecular cloud characterized by a particular mass surface density. In contrast to the standard practice on N-body studies, we do not assume that all stars are formed at once. We explore the effects of different star formation rates on the global structure and evolution of young embedded star clusters considering different primordial binary fractions and mass segregation levels. Our clumps with initial masses of $M_{\rm cl} = 3000\,M_\odot$, embedded in ambient cloud environments of $\Sigma_{\rm cloud} = 0.1$ and 1 g cm^{-2}, gradually form stars with a fiducial star formation efficiency of 50% until gas is exhausted. We show that most of the interesting dynamical processes that determine the future of the cluster, happen during these early phases. In particular, the ejected stellar population is very sensitive to the duration of star cluster formation. We show that the average energy of runaway stars increases as the star formation rate decreases due to the longer time that the cluster is able to remain in a dense state, favouring dynamical ejections.

Keywords: galaxies: star clusters: general – galaxies: star formation – methods: numerical

1. INTRODUCTION

The majority of stars appears to form in star clusters (Lada & Lada 2003; Gutermuth et al. 2009) and therefore understanding star formation is in large part linked to understanding how and where star cluster formation takes place. Observationally, it is known that star clusters are born from overdense gas clumps within giant molecular clouds (GMC) (e.g. McKee & Ostriker 2007). However, several aspects about this process are still under active debate. In particular, there is no agreement yet if the formation timescale of star clusters is a relatively fast process, i.e., happening within about one or a few free fall times, (Elmegreen 2000, 2007; Hartmann & Burkert 2007), or a slow process that can last for several or many free fall times (Tan et al. 2006; Nakamura & Li 2007, 2014)

A key process that may regulate the formation timescale of star clusters is turbulence. Turbulent motions, in combination with magnetic fields, have been invoked to be important in stabilizing the collapse of a star-forming clump (e.g., McKee & Tan 2003). Although turbulence is known to decay in about one crossing time (Stone et al. 1998; Mac Low et al. 1998), i.e., about two free-fall times for a virialized clump, the turbulence could be maintained by protostellar outflow feedback from a low level of star formation (Tan et al. 2006; Nakamura & Li 2007, 2014).

In this work, continuing on from our initial study (Farias et al. 2017, Paper I), we study the dynamical evolution of a forming stellar population of a star-forming clump that will yield a bound star cluster, along with an unbound and dynamically-ejected population of stars. We use a dedicated N-body code, since we aim to accurately follow stellar orbits, including binary and higher-order multiple systems. The gas is treated as an evolving background potential and various aspects of the star formation process, including its rate, degree of primordial binarity, primordial binary properties, degree of primordial mass segregation within the spherical clump, are parameterized and the effects of these choices explored. The calculations are relatively inexpensive, which allows many realizations to be carried out. This is necessary since stellar dynamics is a chaotic process and the stellar initial mass function is sparsely sampled at the high-mass end, so we need many realizations of clusters to find average quantities.

⋆E-mail:juan.farias@chalmers.se

2. METHODS

2.1. *Background gas model*

We assume star clusters are formed from turbulent gravitationally bound starless gas clumps within giant molecular clouds. Following Paper I, we describe the structure of the clump using the turbulent core/clump model of (McKee & Tan 2003, hereafter MT03). Clumps are described as polytropic spheres in virial and pressure equilibrium with their surroundings. The density profile of such clumps is expressed as:

$$\rho_{\rm cl}(r) = \rho_{\rm s,cl}\left(\frac{r}{R_{\rm cl}}\right)^{-k_\rho}, \quad (1)$$

and the velocity dispersion profile as:

$$\sigma_{\rm cl}(r) = \sigma_{\rm s}\left(\frac{r}{R_{\rm cl}}\right)^{(2-k_\rho)/2}, \quad (2)$$

where $\rho_{\rm s,cl}$ and $\sigma_{\rm s}$ are the density and velocity dispersion at the surface of the clump, respectively, and $R_{\rm cl}$ is the radius of the clump, i.e., the location of this surface boundary. The values of these three characteristic quantities are defined by the surrounding cloud's mass surface density, $\Sigma_{\rm cl}$ (see Paper I for the exact relation).

Table 1
Parent clump parameters

	$\Sigma_{\rm cl}$ (g cm^{-2})	$M_{\rm cl}(M_\odot)$	$t_{\rm ff}$ (Myr)	$R_{\rm cl}$ (pc)	k_ρ	$\phi_{P,{\rm cl}}$	$\phi_{\bar{P}}$	$\phi_{\rm B}$	$\sigma_{\rm cl}$ (km/s)
Low-Σ Clump	0.1	3000	0.53	1.159	1.5	2	1.31	2.8	1.71
High-Σ Clump	1	3000	0.095	0.367	1.5	2	1.31	2.8	3.04

Table 2
Initial conditions for simulation sets

Set name	$\epsilon_{\rm ff}$	ϵ	$\langle N_*\rangle$	$f_{\rm binary}$	$f(e)$	IMF	IMS	S.E.	Comment in plots
`fiducial`	0.01, 0.03, 0.1, 0.3, 1	0.5	4000	0.5	$\delta(e)$	Kroupa (2001)	N	Y	Fiducial Case
`binaries_100`	0.03	0.5	4000	1.0	$\delta(e)$	Kroupa (2001)	N	Y	100% binaries
`segregated`	0.03	0.5	4000	0.5	$\delta(e)$	Kroupa (2001)	Y	Y	Mass segregated

Note. — For each of the sets named in the first column 20 simulations were performed for each of the $\epsilon_{\rm ff}$ values listed in column 2 and for each set of clumps parameters listed in Table. 1. Third column shows the assumed SFE, fourth column shows the average number of stars per simulation, fifth column the primordial binary fraction, sixth column the eccentricity distribution function, column seven shows the assumed IMF, column eight stands for whether the cluster is initially mass segregated (IMS). Column nine shows if Stellar evolution is included in the set and last column is a comment from which we refer to the set in the graphs for clarity.

In Paper I we assumed the fast formation limit, which means that star formation happened instantly and any residual gas also was expelled from the system instantly. In this paper, however, we leave this approximation behind and acknowledge that stars are born gradually. Therefore natal gas is still present while stars are being formed. The presence of the gas, with a radial profile described by Eq. 1, is emulated by a time-dependent background potential, i.e.,

$$\phi_{\rm gas}(r,t) = \begin{cases} \dfrac{GM_{\rm cl}(t)}{(2-k_\rho)R_{\rm cl}}\left[\left(\dfrac{r}{R_{\rm cl}}\right)^{2-k_\rho} - 3 + k_\rho\right], r \le R_{\rm cl} \\ -\dfrac{GM_{\rm cl}(t)}{r} \qquad\qquad\qquad\qquad , r > R_{\rm cl} \end{cases} \quad (3)$$

where G is the gravitational constant and $M_{\rm cl}(t)$ the time-dependent clump mass. Note, we do not include any effects of mass beyond the clump radius.

In this paper we assume a constant star formation rate (SFR) defined using the initial parameters of the clump, i.e.,

$$\dot{M}_* = \frac{\epsilon_{\rm ff} M_{\rm cl,0}}{t_{\rm ff,0}}. \quad (4)$$

As stars are formed, some gas is assumed to leave the system instantly according to a given star formation efficiency, ϵ, defined as the ratio between the stellar mass formed and the total mass required to form such stellar mass. The time-evolution of the global gaseous mass of the clump is given by:

$$M_{\rm cl}(t) = \begin{cases} M_{\rm cl,0} - \dfrac{\dot{M}_*}{\epsilon} t \, , t \le t_* \\ 0 \qquad\qquad , t > t_* \end{cases} \quad (5)$$

where t_* is the time at which gas is exhausted. Since we use a constant SFR and ϵ, Equation 5 takes a linear form and the gas exhaustion time is simply $t_* = (\epsilon/\epsilon_{\rm ff}) \times t_{\rm ff,0}$.

2.2. *Gradual formation of stars*

In order to simulate the birth of stars in a cluster at different star formation rates, we have developed a modified version of the direct N-body code `Nbody6++` (Aarseth 2003; Wang et al. 2015). We introduced routines in order to add particles during run-time, including formation of primordial binaries. The introduction of stars is carried out as follows: (1) We create the final phase-space distribution of stars following the model described in Paper I. (2) The set of particles is unsorted creating the formation sequence. The used unsort method ensures that the global binary fraction is preserved at all times if no binaries are lost during the simulation. (3) We select an initial set of $N_{\rm i} = 150$ particles from the list that are introduced in the simulation as usual, i.e., as the initial cluster, which is a small fraction of the eventual total. (4) For each particle in the subsequent list, the time needed for its formation is calculated as $t_{*,{\rm i}} = m_{\rm i}/{\rm SFR}$ and the cluster is evolved until $t + t_{*,{\rm i}}$ when the particle is born. This step is repeated until there is no more gas available. Binaries are always added together, and the time necessary for the formation of a binary is given by its total mass.

As in Paper I, stellar mass loss from stellar evolution is included in the simulations using the analytical models developed by Hurley et al. (2000, 2002) implemented in `Nbody6++`. We also include artificial velocity kicks from asymmetrical supernovae ejections. The magnitude of the velocity kicks follows a Maxwell velocity distribution with $\sigma = 265$ km/s based on proper motion observations of runaway pulsars (Hobbs et al. 2005).

2.3. *Overview of the Cluster Models*

In this work, we make exactly the same assumptions for the stellar distribution of stars in space and in velocity structure as in Paper I. We assume stars are formed from the turbulent clump of gas, and therefore they follow the same global structure given by Equations 1 and 2. In this paper we focus on the differences generated when varying the rate at which stars are formed parametrized by $\epsilon_{\rm ff}$, for which the case of Paper I can be compared as $\epsilon_{\rm ff} \to \infty$. We focus on the `fiducial` set of simulations defined in Paper I (see Table 2), i.e., using a standard initial mass function (Kroupa 2001) with a binary fraction $f_{\rm bin}$ with circular orbits. Binary properties are drawn with a log-normal period distribution with a mean of $P = 293.3$ yr and standard deviation of $\sigma_{\log P} = 2.28$ (with P in days) according to observations of Raghavan et al. (2010). The mass ratio distribution follows the form $dN/dq \propto q^{0.7}$ as observed in young star clusters (Reggiani & Meyer 2011). We test values of $\epsilon_{\rm ff} = 0.01$, 0.03, 0.1, 0.3, and 1, adopting

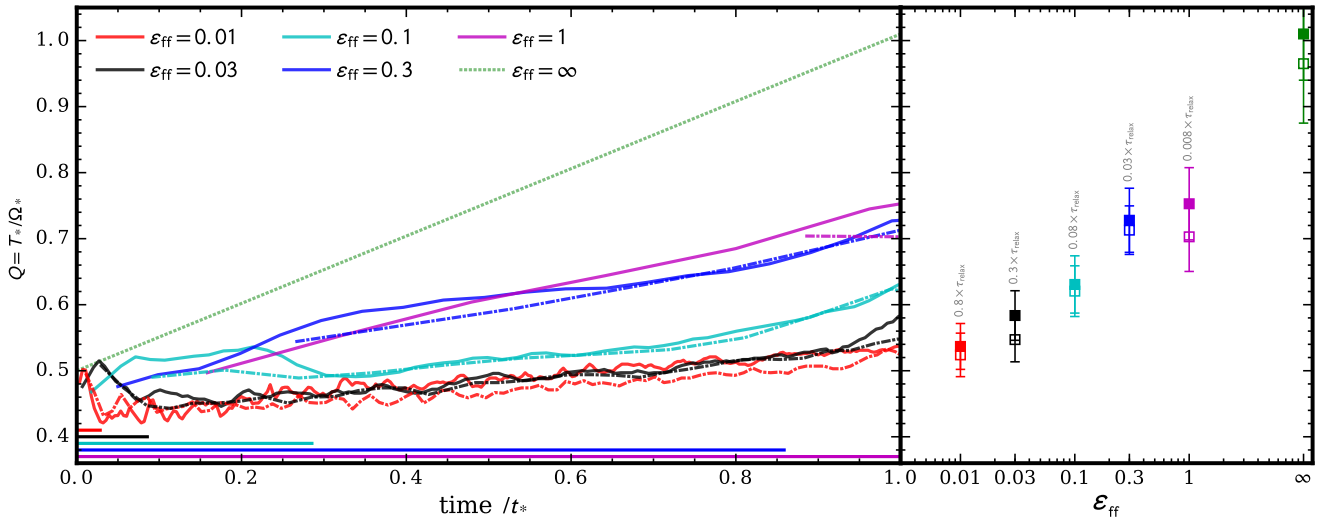

Figure 1. Evolution of the virial ratio during the formation of the star clusters (left) for different values of ϵff, where time is normalized by the duration of the star-forming stage, t_*. For reference, for each value of $\epsilon_{\rm ff}$, the length of a crossing time is drawn as an horizontal line in the bottom of the panel. The virial ratio at the end of the formation stage is shown in the right panel as a function of $\epsilon_{\rm ff}$, where errorbars representing the standard deviation of the mean values over the 20 realizations performed for each set. Each point is labelled with the length of t_* in terms of the relaxation time of the system.

$\epsilon_{\rm ff} = 0.03$ as a fiducial value.

In this work, we deviate from the fiducial case only to see differences of two extremes: the `binaries_100` case with 100% binaries and the `segregated` case where stars are radially sorted based on mass emulating an extreme case of mass segregation. However, these cases are only tested against the fiducial value of $\epsilon_{\rm ff}$.

A summary of the initial conditions is shown in Table 2, as well as the parameters chosen for the parent clumps in Table 1.

3. RESULTS

4. STAR CLUSTER FORMATION STAGE

The main difference between this and most previous N-body studies, is that we recreate the formation stage of star clusters by gradually adding stars during the simulation. Since the phase-space distribution of the stars follows the structure of the gas, this causes that low SFE star clusters are born with quite high velocities initially, and as well, a dynamical structure that does not represent a stellar system in dynamical equilibrium. Even though the virial ratio of a system with SFE of 100% would be $Q = 0.5$ (see Figure 1 of Paper I), the system is not in equilibrium since the velocity structure of the gas (a velocity dispersion that increase with the central distance) is the opposite of a dynamically stable stellar system (for which the velocity dispersion decreases with radius). A longer formation timescale is crucial for the star cluster in order to rearrange internally before residual gas is dispersed, and therefore start its gas free evolution closer to equilibrium.

Figure 1 shows the evolution of Q with time during the formation stage for the different values of $\epsilon_{\rm ff}$ adopted in this work. The time is normalized by t_*, and for reference we also show the length of a crossing time for each value of $\epsilon_{\rm ff}$ in this normalization. Initially all systems start their evolution close to $Q = 0.5$ since all the mass of the clump is present. As the cluster evolves, the stars that are present pursue equilibrium as more stars arrive with high velocities and the mass of the gas decreases. However, the initially small cluster needs about one relaxation time ($\tau_{\rm relax} \sim 50\,\tau_{\rm cross}$ in the systems studied here) to reach equilibrium. The duration of star cluster formation in the fast regime, $\epsilon_{\rm ff} > 0.1$, is comparable to the crossing time of the system. In this short time the star cluster is unable to reach equilibrium and the consequence is that it emerges from the gas with supervirial velocities. In contrast, in the low regime $\epsilon_{\rm ff} \ll 0.1$, i.e., with slow star formation, the timescale is comparable to the relaxation time, and the stellar cluster has plenty of time to reach equilibrium. In this scenario, the formation of the star cluster is a race to reach equilibrium, and the path to equilibrium is truncated when gas is gone and the cluster emerges from its natal clump

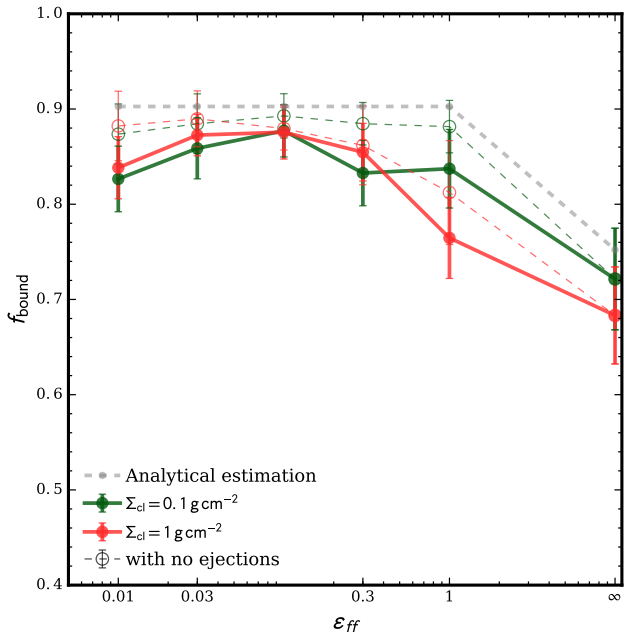

Figure 2. Bound mass fraction measured at the time at which the gas is exhausted (t_*), for simulations in the `fiducial` set in the high (red) and low (green) Σ cases. Gray dashed line shows an semi-analytical estimation (see A). Each point with errorbars represents the mean and standard deviation for the 20 simulations. Thin lines with open symbols show the resulting bound fractions, if dynamical ejections are counted as bound, for comparison with the analytic model.

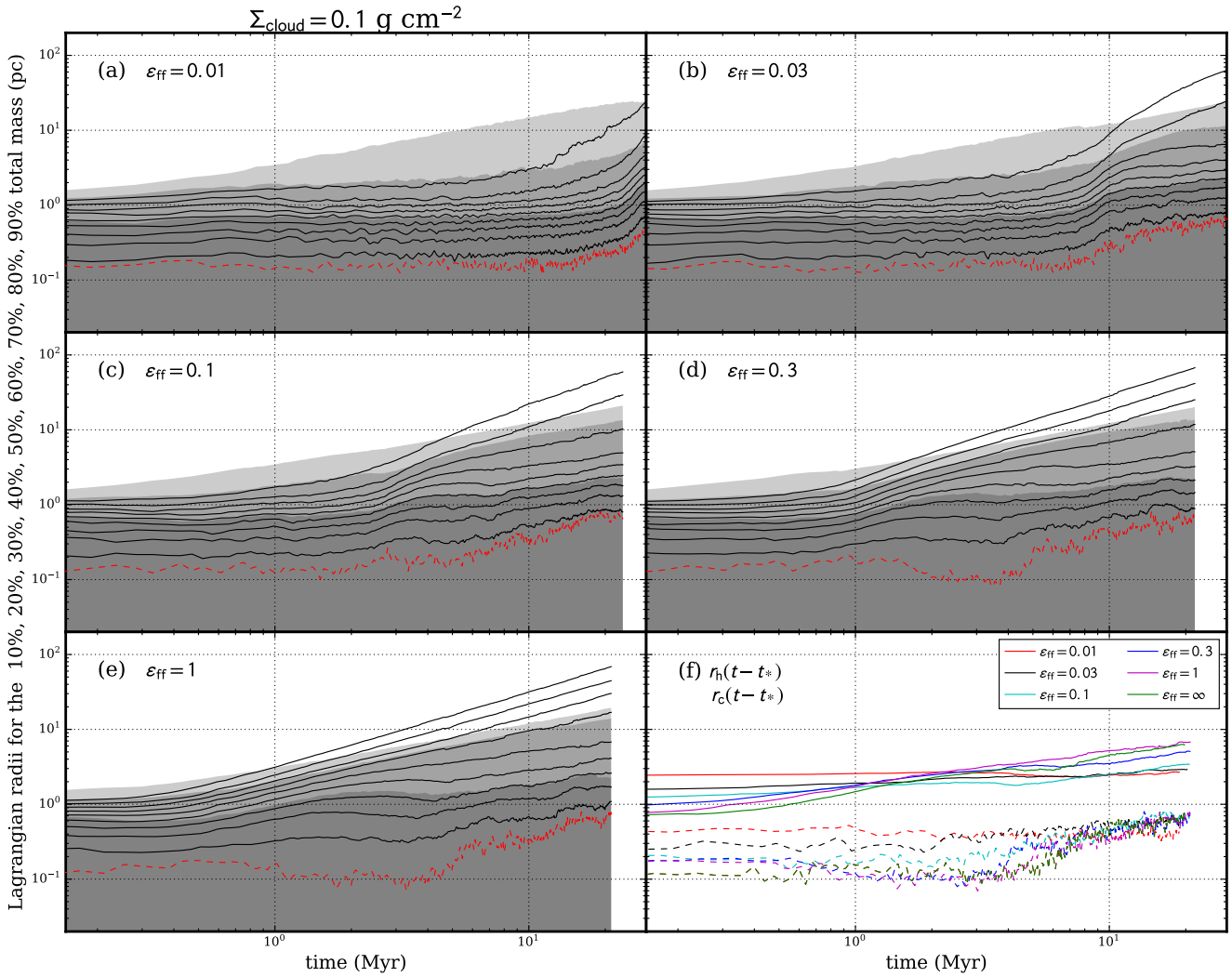

Figure 3. Average Lagrangian radii evolution for star clusters born from a parent clump with $\Sigma_{\rm cl} = 0.1$ g cm^{-2} and different values of $\epsilon_{\rm ff}$. We show the Lagrangian radii for the 10%, 20%, 30%, 40%, 50%, 60%, 70%, 80% and 90% masses (black solid lines). Red dashed lines are the core radii defined in Aarseth (2003). Gray shaded areas represent the regions below the 50%, 95% and 100% mass radius of the bound cluster.

with a virial ratio given by this truncation (see right panels of Figure 1). The two extreme values of Q that the cluster will be able to reach at the end of its formation are $Q = 0.5$ when $t_* \gtrsim \tau_{\rm relax}$, and the highest virial ratio is given by the fast formation limit, i.e., Figure 1 of Paper I. The dynamical state at the beginning of the formation is also given by Figure 1 of Paper I, but taking the values from a SFE$= 1$.

5. EMERGING FROM THE GAS

Figure 2 shows the different values of bound fraction ($f_{\rm bound}$) at $t = t_*$. While there are some differences between the models, that we will discuss below, in general there is no dependence of $f_{\rm bound}$ on $\epsilon_{\rm ff}$. The different values of Q obtained at the end of the formation stage, between $0.5 < Q < 0.8$, would suggest different bound fractions (see e.g. Farias et al. 2018; Lee & Goodwin 2016), however the differences in this narrow range are very small to reflect on the resulting bound fractions. Second order differences are a combination of dynamical effects and the assumptions of the formation process.

Let us first ignore early dynamical effects such as virialization and the rearrangement of the stellar masses. In this regime, the sequential formation of stars does not affect the final bound fraction. As each star is formed the escape velocity decreases in the same amount instantly. Therefore, how fast or slow stars are created becomes irrelevant because of the instant residual gas loss assumed in this work. Gray dashed lines on Figure 2 show an analytical estimation considering the radial and time dependent escape velocity and clump velocity distribution based on the cloud model described in Section 2.1 (see Appendix A for details). Thin lines with open symbols in Figure 2 shows the resulting bound fractions when only removing stars that are born unbound, i.e., ignoring dynamical ejections. These agree with the analytic estimation quite well, except in the high Σ case with $\epsilon_{\rm ff} = 1$ where the bound fraction drops. This is a extreme case on which star formation happens very fast, $t_* \approx 0.05$ Myr and then several stars are born in groups, with bigger drops in escape velocity, becoming closer to the extreme case of $\epsilon_{\rm ff} = \infty$ when all stars are form together.

The actual bound fraction is shown by the solid lines with solid circles on Figure 2. Values of $\epsilon_{\rm ff} = 0.1$ and 0.3 (low Σ) show slightly lower bound fractions, probably due to the combination of the higher virial ratios and dynamical ejec-

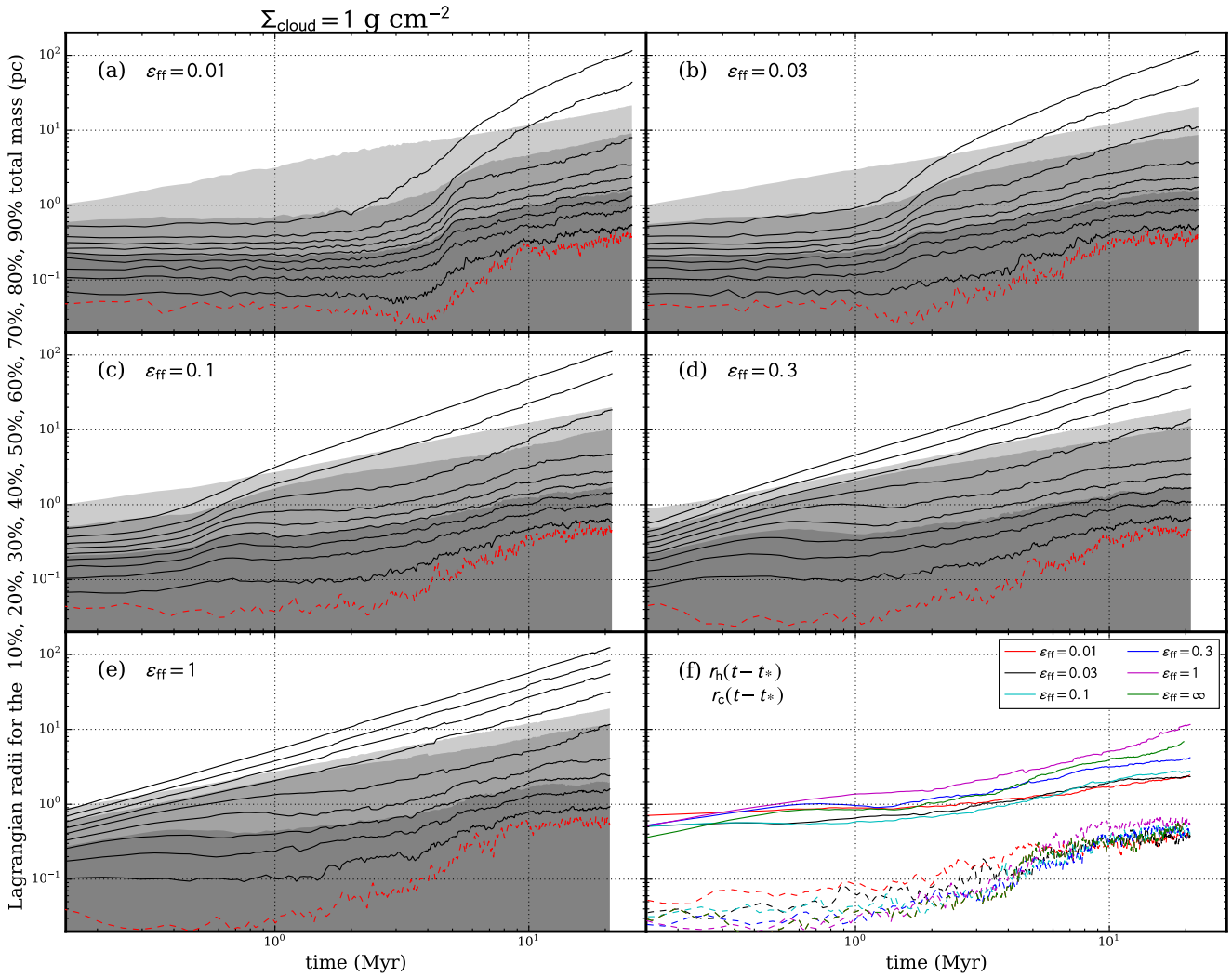

Figure 4. Same as Figure 3 for star clusters born from a clump with $\Sigma_{\rm cl} = 1$ g cm^{-2}.

tions that happen during formation. Then, at low values of $\epsilon_{\rm ff} < 0.1$ there are also slightly smaller bound fractions: in this case, dynamical ejections play an important role during formation, since it happens on several ($\gtrsim 10$) crossing times. It is at $\epsilon_{\rm ff} = 0.1$ where both effects appear to be minimized, however improved statistics are needed for confirmation.

6. GLOBAL EVOLUTION

We have seen that the key influence of different values of $\epsilon_{\rm ff}$ is the ability of the star cluster to reach equilibrium before gas is exhausted/ejected. While the difference in their ability to survive gas expulsion is not raised considerably, the condition on which they face their early gas-free evolution is very different. We have evolved every model for 20 Myr after all stars are formed. The global evolution under each model's parameters can be appreciated through the Lagrangian radii shown in Figure 3 for the low Σ case and in Figure 4 for the high Σ case. Comparing between these mass surface densities, the differences are similar as found in Paper I: star clusters born with high density expand at a faster rate than star clusters born in a less dense state. However, the expansion is also regulated by the star formation rate.

Panel (f) of Figures 3 and 4 shows the half mass and core radii for all the values of $\epsilon_{\rm ff}$ with a time offset such as the starting point is the moment when they start their gas free phase, i.e., $t-t_*$. High values of $\epsilon_{\rm ff}$ results in star clusters that expand much faster than the ones born with low $\epsilon_{\rm ff}$. As we can extract from Figure 5, where we compare the half mass radii at 20 Myr after formation, the extreme cases are when star clusters are born with low density and low $\epsilon_{\rm ff}$ do not expand at all since the expulsion of gas (they only expand initially a factor 2 during the formation stage, see Figure 9). On the other hand, a star clusters born in one free fall time ($\epsilon_{\rm ff} = 1$) expands a factor 12 during the first 20 Myr.

A summary of the evolution of different parameters is shown in Figure 6. Including the evolution of the extremely mass segregated case (`segregated` set, in dot dashed lines), which shows that dynamical effects such as primordial mass segregation can also modify the expansion rate of star clusters considerably, in a higher degree than the case `binaries_100` set (dotted lines). The reason might be that the central velocity dispersion rises rapidly in the center of a mass segregated cluster, and reaching equilibrium from such state takes a longer time since the kinetic energy is higher and the necessary half mass radii for equilibrium are also larger.

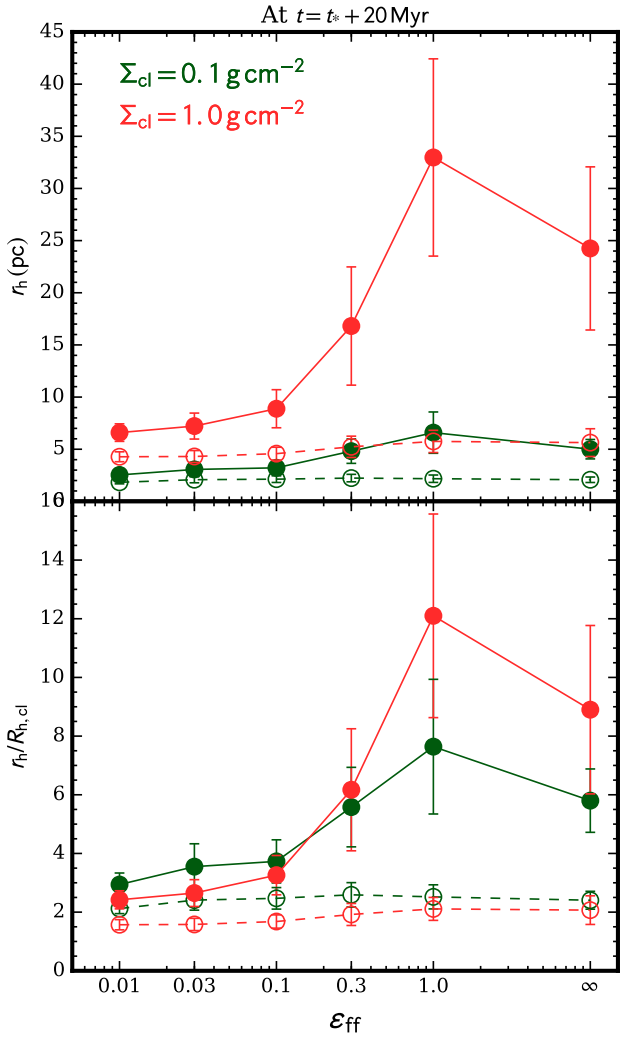

Figure 5. Size of star clusters at 20 Myr (left panels) and at 20 Myr after star formation stops (right panels). Top panels shows the half-mass radius in parsecs and bottom panels shows the half-mass radius relative to the initial clump size (R_{cl}). Filled circles are the values measured with all stars in the clusters, while open circles are values measured only with the bound stars.

7. THE UNBOUND POPULATION

Following our analysis from Paper I, we identify bound members in the simulations snapshot by snapshot, classifying stars in three groups: (1) bound stars, which are the ones that remain bound until the end of the simulation; (2) unbound stars, which are the ones that are unbound from the first snapshot that they appear, i.e., they are born unbound[1]; (3) Ejected stars, which are stars that appear bound in one snapshot but later they do not. With the ejected stars, we also subdivide them in: (A) Strong dynamical ejections, stars that shows $\Delta T_i \geq 2\Delta\Omega_i$, when ejected; (B) Supernovae ejections, including stars receiving velocity kicks during their supernovae phase, and stars ejected because they were binary companions of a star that exploded as supernovae; and (C) gentle ejections, stars that become unbound because of the evolving potential of the cluster, which we distinguish by $\Delta T_i < 2\Delta\Omega_i$. In this work, we refer to runaway stars, as dynamically ejected stars with velocities above 20 km/s.

We recorded the time when strong ejections happen and we show the number of ejected stars per cluster per logarithmic time interval in Figure 7 for the low (left) and high (right) Σ cases. The number of dynamical ejections grows continuously reaching a peak at the point where star formation finishes and the number density is at it highest point. After gas is gone and the cluster expands, dynamical ejections fall exponentially remaining relatively flat in logarithmic time intervals.

Figure 7 shows the collected unbound stars on each simulation set, including the percent of runaway stars in the O and B type mass range. Also, O and B stars ejected by being involved in the supernovae explosion of a massive binary companion, are shown in colored shaded areas. Solid lines show the total percent of dynamical ejections from the 20 simulations of each set. The percent of ejected stars increase with ϵ_{ff}, which may be a combination of several effects caused by the timescale of star cluster formation.

In the fast formation regime, the escape velocity falls faster, and there are more gentle ejections because stars do not have time to relax. However another factor is the number of massive stars that are in the cluster at the same time. In the most extreme case of long star formation – in the low Σ case and with $\epsilon_{ff} = 0.01$ – the formation of the star cluster takes 26 Myr. Given that for each cluster the total number of O-type stars is around 8 per cluster and they are born uniformly in time, and also that the life of a O-type star is typically around 5 Myr, then in the extremely long time of 26 Myr only two O-type stars are able to live in the cluster at the same time. This is much less extreme with shorter (physical) formation timescales, however this can be enhanced given that 30-60% O-type stars are ejected dynamically, and 50% of them are in binary systems (likely with other massive star). Then, the number of massive stars within the cluster at a given time may be low even in the case of shorter formation timescales. It is expected that massive stars eject many lower mass stars before they are ejected This effect raises the question of whether massive stars are actually born uniformly in time respect to other stars, or if they are born first, when the gas mass reservoir is bigger.

Even though the fraction of O stars that are ejected increase with ϵ_{ff}, the fraction of O-type runaway stars (green dashed lines) raise at low ϵ_{ff}, strongly in the low Σ case, and less dependent at high Σ scenario given that high densities enhances the ejection rates in all cases. However, if we compare the number of runaway stars in relation to only unbound stars (analog to stars in the field), i.e., dividing the values for runaways (dashed lines) by the values for ejected stars (solid lines) on Figure 7, the dependence is much stronger. The limits would be that with in the low formation regime (ϵff $= 0.01$) ~57% (22%) of field O stars are runaways in the low (high) Σ case, and in the fast regime the fraction of field runaway stars are ($\epsilon_{ff} = 1$) ~3%(9%) with low (high) Σ.

Observations of runaways have inferred that about 10-30% of O stars and 2-10% of B stars are observed to be runaways (Gies 1987; Stone 1991; De Wit et al. 2005), ranges marked as gray areas on Figure 7. These ranges are somewhat uncertain given the different definitions on the literature and completeness (see Eldridge et al. 2011). At this point, most of our results appear to be below the observational limits, except at low ϵ_{ff}, where our results approach the lower limit of estima-

[1] However, note that we are constrained by the time resolution of the simulations. This will cause us to classify as unbound stars that were dynamically ejected just after being bound and before the next output time, however we expect that the number of such cases is very small.

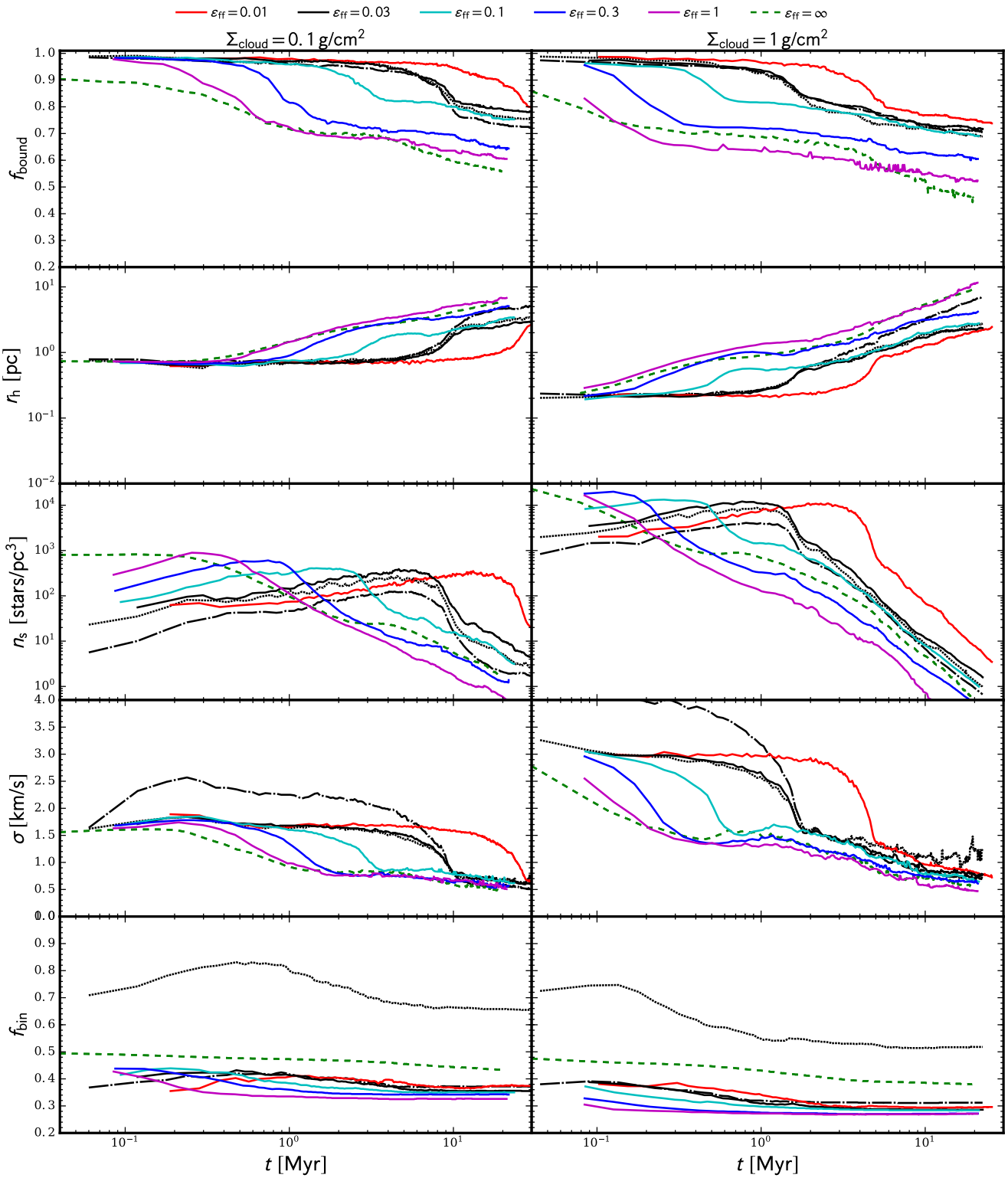

Figure 6. Time evolution of properties for our fiducial clusters formed with SFE=50% and a range of $\epsilon_{\rm ff}$ values in different colors. Solid lines show results for the `fiducial` set, dotted lines for the set `binaries_100`, dot dashed lines for `segregated` and dashed lines the results of the fast formation limit described in Paper I. Left column shows clusters forming from a $\Sigma_{\rm cl} = 0.1$ g cm^{-2} environment; right column from a $\Sigma_{\rm cl} = 1$ g cm^{-2} environment. The lines in each panel show median values calculated from the 20 simulations performed for each set. Top row shows the fraction of bound mass in the cluster relative to the instantaneous stellar mass, where in this figure unbound stars inside the 95% mass radius of the bound cluster are kept to show the timescale of their escape. Second row shows the evolution of the half mass radius $r_{\rm h}$ for all the stars in the simulation. Third row shows the average number density of systems (n_s), where per systems we refer to singles and binaries, measured inside the volume defined by $r_{\rm h}$. Fourth row show the evolution of the velocity dispersion measured inside $r_{\rm h}$, and bottom row shows the evolution of the global binary fraction.

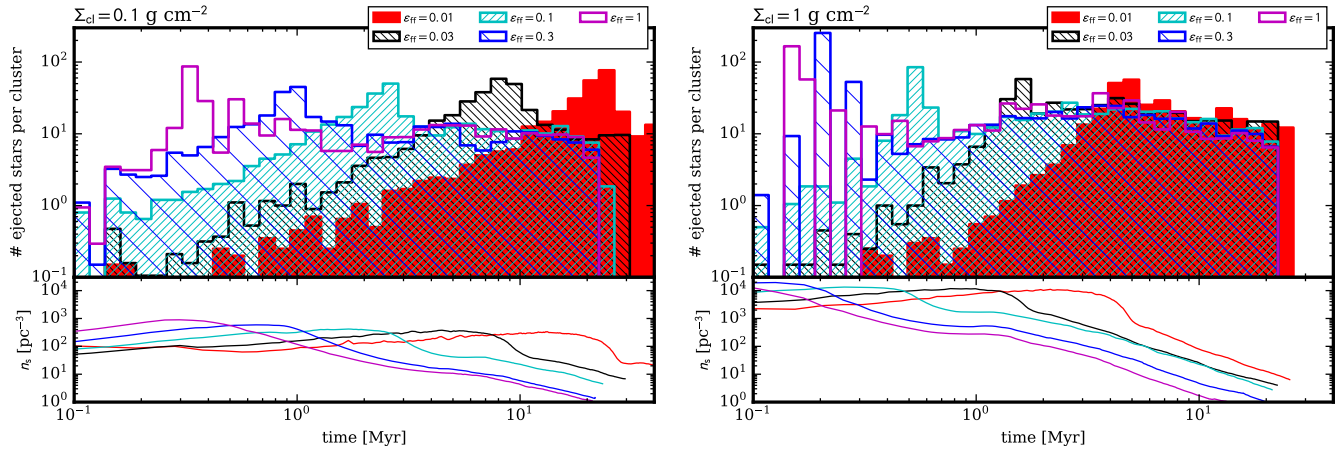

Figure 7. Number of strong dynamical ejections (see text) per logarithmic time interval per simulated cluster in the `fiducial` set with different $\epsilon_{\rm ff}$. As a reference of the cluster structure, bottom panels show the number density inside the half mass radius of the cluster.

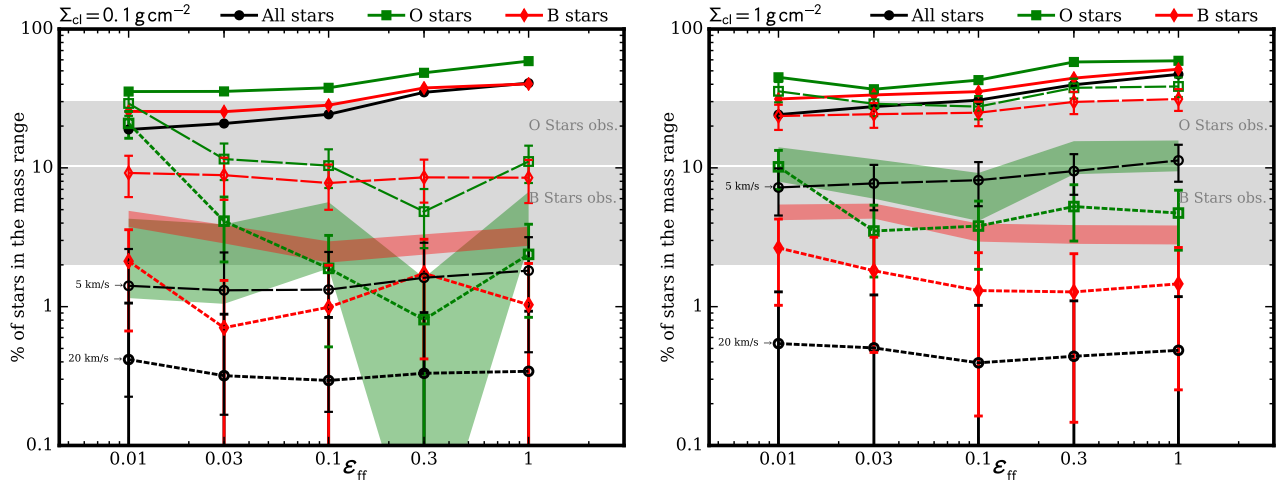

Figure 8. Percentage of ejected stars relative to all stars in each mass range. O (red diamonds) B (green squares) and all stars in each set. Open symbols show the percentage of dynamically ejected stars at different velocity cutoffs, i.e. $v_i > 20$ km/s (short dashed lines) and 5 km/s (long dashed lines). Gray shaded areas shows observed fractions of O and B star runaways. Green and red filled areas show the percentage of stars ejected by supernovae ejections.

tions. However, this result is highly dependent on the velocity cutoff that we choose, as well as those used to define the observational samples. These results suggest that the timescale of star formation could play an important role at reproducing observed numbers of runaways. However, it is still important to include more realistic assumptions in future work, such as space-time dependent $\epsilon_{\rm ff}$ and massive star formation, primordial substructure and degrees of mass segregation, which must all been taking into account before comparing with observations.

8. DISCUSSION

We have presented the second step in the modeling of star clusters born from the turbulent clump model of McKee & Tan (2003). In this paper, we have relaxed the assumption of instantaneous star formation used in Paper I and in most previous N-body studies, and we have focused on exploring the effects of the star cluster formation timescale on the evolution of star clusters, parameterized by the star formation efficiency per free fall time ($\epsilon_{\rm ff}$, Krumholz & McKee 2005). By exploring this parameter, we have studied the dynamics of the formation of star clusters including the gradual formation of stars. This stage, has been only modeled by the means of (magneto-)hydrodynamical simulations of star formation with the exception of the N-body study of Proszkow & Adams (2009), focused on relatively low densities and without including binaries nor stellar evolution.

This is the first attempt on comprehensively study the dynamics of the stars during star cluster formation. Several assumptions have made this first work possible: We have used an uniform and fixed star formation rate, defined by the initial properties of the clump. However, as the density of the clump decrease, the free fall time does as well and the formation timescale should be even longer than presented in this work. As well, given that the free fall time is density dependent, the central area of the clump will have shorter physical timescales and star formation may happen faster in the center (denser) region of the clump rather than uniformly (see e.g. Parmentier & Pfalzner 2013). However, observationally is highly difficult to estimate if this effect is really as described. It is not possible to measure the real central star formation efficiency of a star forming clump given that as soon as stars are formed, dynamical effects such as relaxation and mass segregation raise the central number of stars and it is very difficult to distinguish stars formed in situ rather than migrated to the center, and the same for the gas that is removed from the center via proto-stellar and stellar feedback. Because of the former, it is uncertain that the central gas density, and local free fall time, remains higher than the rest of the clump. Given this uncertainty, it becomes necessary that the consequences of these scenarios are explored in detail.

In this study, the gaseous clump was modeled in a simplistic way, only decreasing due to the mass of the stars formed and gas ejected. The clump, however, should evolve in much more complex ways as stars are formed. We have assumed that any residual gas is removed instantly as stars form, however this may not be the case in real star forming clumps. Protostellar jets not only could drive the turbulence that potentially can support the cloud but also it is not for sure that the residual gas from star formation will leave the cluster. Residual gas could also remain within clump boundaries and form more stars. Details of this process are uncertain and of course the full star formation process is not as simple as we have modelled it. However, observational estimations of the Orion Nebula Cluster (ONC) have shown evidence of a prolonged star formation rate over its life (Da Rio et al. 2014), suggesting that our starting point for a modeling approach may not be so far from reality. However, the ONC is simply one example and more sophisticated modeling of the efficiency of star formation and gas depletion remains to be studied.

Several authors have shown that slowly removing gas results in clusters that survive gas expulsion better than rapid gas removal (e.g. Baumgardt & Kroupa 2007; Smith et al. 2013). However, this result is not necessarily true with gradual formation of stars, because there are several factors that interplay to obtain the final state of star clusters. As stars are formed the escape velocity of the system drops and new formed stars have higher chances of being born unbound from the cluster. This, however, can be argued to be a consequence of our initial conditions, since in this first attempt, global parameters such as the initial surface velocity dispersion are drawn from the initial state of the clump and are not adapted to account for the system's ejected mass. Still, several factors could potentially drive turbulence during the cluster formation that are not account for McKee & Tan (2003) model. As stars forms, jets from protostars, stellar feedback, among other processes can potentially drive turbulence while stars are being formed in ways not yet known. Therefore, neither increasing or decreasing the system velocity dispersion as mass is loss are necessarily better assumptions.

However, there is a caveat in the assumptions used for the formation of stars that needs to be addressed in future works. As a result of our assumption of instantaneous removal of residual gas, the chances of a star of being born unbound from the cluster are not dependent on how fast stars are being formed. We used a sequential formation of stars.

Early dynamical ejections are, in general, not numerous in the models exposed here, this is a potential consequence of the isotropic formation assumed in this work. An important property that we must include when advancing the realism of our modeling, is the inclusion of substructure, since stars do not seems to form in uniform distributions (e.g. Gutermuth et al. 2008) and it has been shown that substructure influence several important dynamical processes such as mass segregation (Allison et al. 2009a; Domínguez et al. 2017), pre-gas expulsion dynamical equilibrium (e.g. Farias et al. 2015) and star cluster fragmentation (Goodwin & Whitworth 2004). As well, the merging of sub-clumps can potentially raise the interaction rates of binaries and enhance dynamical ejections. However, the energy of the ejected stars appear to be dependent on the formation timescale especially if the initial density of star forming regions is low.

9. CONCLUSIONS

In this modeling of star cluster formation with a pure stellar dynamical study, we have made simple assumptions for the formation of the stars and then explored the effects of different rates of star formation to form a cluster. We summarize our results as follows:

1. The critical difference between models with different $\epsilon_{\rm ff}$ is that star clusters forming slowly ($\epsilon_{\rm ff} \lesssim 0.1$) have several dynamical timescales to reach equilibrium before the gas is exhausted/ejected. Thus they start their gas-free evolution in a more stable configuration.

2. High values of $\epsilon_{\rm ff}$ result in star clusters that expand much faster than the ones with low $\epsilon_{\rm ff}$, which is a con-

sequence of the first result. The expansion rate, however, depends strongly on the initial density of the parent clump, and to a second degree on the level of initial mass segregation and multiplicity.

3. The various dynamical states obtained through the different formation timescales, are not reflected in the bound fractions that star cluster have after formation. In this aspect, the treatment of the residual gas from star formation is a key parameter that need to be modeled consistently.

4. The numbers of massive runaway stars increase from clusters with slow star formation, with this trend being stronger if their numbers are compared to field massive stars rather than the total number of massive stars. This trend is also stronger if the surface density of star forming clump is in the low regime ($\Sigma_{\rm cl} = 0.1$ g cm^{-2}).

In general, the models presented here, requires less dense star forming regions to reproduce the same observational properties. However, there are several other factors that need to be taken into account before comparing with observations. The simple assumptions about the star formation process will be relaxed in our next study.

REFERENCES

Aarseth, S. J. 2003, Gravitational N-Body Simulations, 430
Allison, R. J., Goodwin, S. P., Parker, R. J., et al. 2009a, ApJL, 700, L99
—. 2009b, MNRAS, 395, 1449
Baumgardt, H., & Kroupa, P. 2007, MNRAS, 380, 1589
Da Rio, N., Tan, J. C., & Jaehnig, K. 2014, ApJ, 795, doi:10.1088/0004-637X/795/1/55
De Wit, W., Testi, L., Palla, F., & Zinnecker, H. 2005, Astronomy & Astrophysics, 437, 247
Domínguez, R., Fellhauer, M., Blaña, M., Farias, J. P., & Dabringhausen, J. 2017, MNRAS, 472, 465
Eldridge, J. J., Langer, N., & Tout, C. A. 2011, MNRAS, 414, 3501
Elmegreen, B. G. 2000, ApJ, 530, 277
—. 2007, ApJ, 668, 1064
Farias, J. P., Fellhauer, M., Smith, R., Domínguez, R., & Dabringhausen, J. 2018, MNRAS, 476, 5341
Farias, J. P., Smith, R., Fellhauer, M., et al. 2015, MNRAS, 450, 2451
Farias, J. P., Tan, J. C., & Chatterjee, S. 2017, ApJ, 838, 116
Gies, D. R. 1987, The Astrophysical Journal Supplement Series, 64, 545
Goodwin, S. P., & Whitworth, A. P. 2004, A&A, 413, 929
Gutermuth, R. A., Megeath, S. T., Myers, P. C., et al. 2009, ApJS, 184, 18
Gutermuth, R. A., Myers, P. C., Megeath, S. T., et al. 2008, ApJ, 674, 336
Hartmann, L., & Burkert, A. 2007, ApJ, 654, 988
Hobbs, G., Lorimer, D. R., Lyne, A. G., & Kramer, M. 2005, MNRAS, 360, 974
Hurley, J. R., Pols, O. R., & Tout, C. A. 2000, MNRAS, 315, 543
Hurley, J. R., Tout, C. A., & Pols, O. R. 2002, MNRAS, 329, 897
Kroupa, P. 2001, MNRAS, 322, 231
Krumholz, M. R., & McKee, C. F. 2005, ApJ, 630, 250
Lada, C. J., & Lada, E. A. 2003, ARA&A, 41, 57
Lee, P. L., & Goodwin, S. P. 2016, MNRAS, 460, 2997
McKee, C. F., & Ostriker, E. C. 2007, ARA&A, 45, 565
McKee, C. F., & Tan, J. C. 2003, ApJ, 585, 850
Nakamura, F., & Li, Z.-Y. 2007, ApJ, 662, 395
—. 2014, ApJ, 783, 115
Parmentier, G., & Pfalzner, S. 2013, A&A, 549, A132
Proszkow, E.-M., & Adams, F. C. 2009, ApJS, 185, 486
Raghavan, D., McAlister, H. A., Henry, T. J., et al. 2010, ApJS, 190, 1
Reggiani, M. M., & Meyer, M. R. 2011, ApJ, 738, 60
Smith, R., Goodwin, S., Fellhauer, M., & Assmann, P. 2013, MNRAS, 428, 1303
Stone, R. C. 1991, AJ, 102, 333
Tan, J. C., Krumholz, M. R., & McKee, C. F. 2006, ApJL, 641, L121
Wang, L., Spurzem, R., Aarseth, S., et al. 2015, MNRAS, 450, 4070

APPENDIX

ANALYTICAL ESTIMATION OF BOUND FRACTIONS

Given that all properties of the newly formed stars are given by an analytical prescription, it is possible to estimate the amount of stellar mass that should keep bound at birth. Stars are born with one-dimensional component velocity dispersions following a Normal distribution with $\sigma_x = \sigma_y = \sigma_z$ given by Equation 2. Then, at a given radii, stars born with a Maxwell-Boltzman velocity distribution with scale parameter $a(r) = \sqrt{3}\sigma_{\rm cl}(r)$. Therefore, we can use the cumulative distribution function (CDF) to find the fraction of stars that have velocities below the escape velocity at a given radius.

The escape velocity at a given radii r is given by $v_{\rm esc} = \sqrt{-2\Phi(r,t)}$, where $\Phi(r,t)$ is given by Eq. 3. For convenience, we form the expression $v_\sigma(r,t) = v_{\rm esc}(r,t)/\sigma_{\rm cl}(r)$, that reduces to:

$$v_\sigma(r,t) = \sqrt{\frac{4(k_\rho-1)}{3(k_\rho-2)}\phi_{\rm B}\left[1-(3-k_\rho)\left(\frac{r}{R_{\rm cl}}\right)^{k_\rho-2}\right]\frac{M_{\rm total}(t)}{M_{\rm cl,0}}}, \tag{A1}$$

where $\phi_{\rm B}$ a factor that accounts for the magnetic field support in the cloud (see Paper I and MT03), and the factor $M_{\rm total}(t)/M_{\rm cl,0}$ is the total mass of the system (stars and gas) at a given time.

Then, using the Maxwell-Boltzman CDF, the fraction of stars that that born bound at a given radii r, is:

$$f_{\rm bound}(r) = {\rm erf}\left(\frac{v_\sigma(r)}{\sqrt{2}}\right) - \sqrt{\frac{2}{\pi}}v_\sigma(r)\exp\left(-\frac{v_\sigma^2(r)}{2}\right) \tag{A2}$$

The total fraction of mass is different at each radii, therefore the total bound fraction is Eq. A2 mass averaged over the clump, which reduces to:

$$f_{\rm bound,tot} = \frac{3-k_\rho}{R_{\rm cl}}\int_0^{R_{\rm cl}} f_{\rm bound}(r)\left(\frac{r}{R_{\rm cl}}\right)^{2-k_\rho} dr \tag{A3}$$

which can only be solved numerically.

Equation A3 can be evaluated at $t = 0$ assuming that $M_{\rm total} = M_{\rm cl,0}\epsilon$ assuming all gas is loss instantly to obtain the bound fraction of $\epsilon_{\rm ff} = \infty$. However, in order to obtain the values for other formation rates, it needs to be integrated over time using a numerical method.

EVOLUTION OF DIFFERENT PARAMETERS DURING THE FORMATION STAGE

In this section we show the evolution of several parameters during the star formation stage, i.e. with $t \leq t_*$. Figure 9 shows the evolution of the velocity dispersion σ and the half mass radius of the stars, both normalized by $\sigma_{\rm cl}$ and $R_{\rm cl}$ respectively. The evolution of these parameters shows how the cluster expands, increasing the global potential energy (decreasing the binding energy of the cluster), and the velocity dispersion decrease and therefore the kinetic energy of the stars. In this way, the cluster rearranges in order to pursuit an equilibrium state. Figure 10 shows the mass segregation ratio ($\Lambda_{\rm MSR,}$ Allison et al. 2009b) for the 10 most massive stars in the cluster. The longer dynamical scales enable the star cluster to develop higher levels of mass segregation, before starting their life as a gas-free entity.

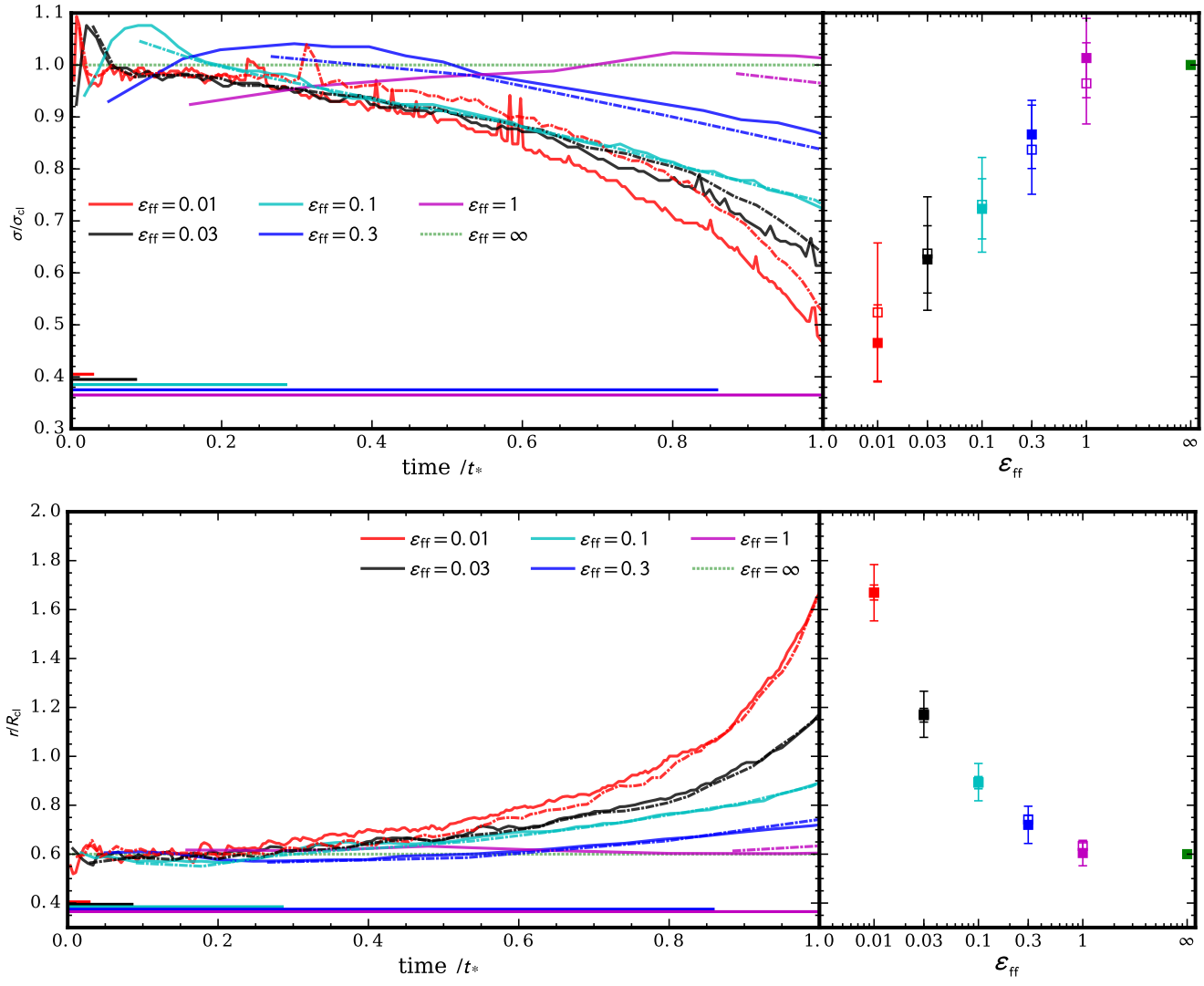

Figure 9. Same as Figure 1 for the velocity dispersion normalized by $\sigma_{\rm cl}$ (top), the half mass radius normalized by $R_{\rm cl}$ (bottom).

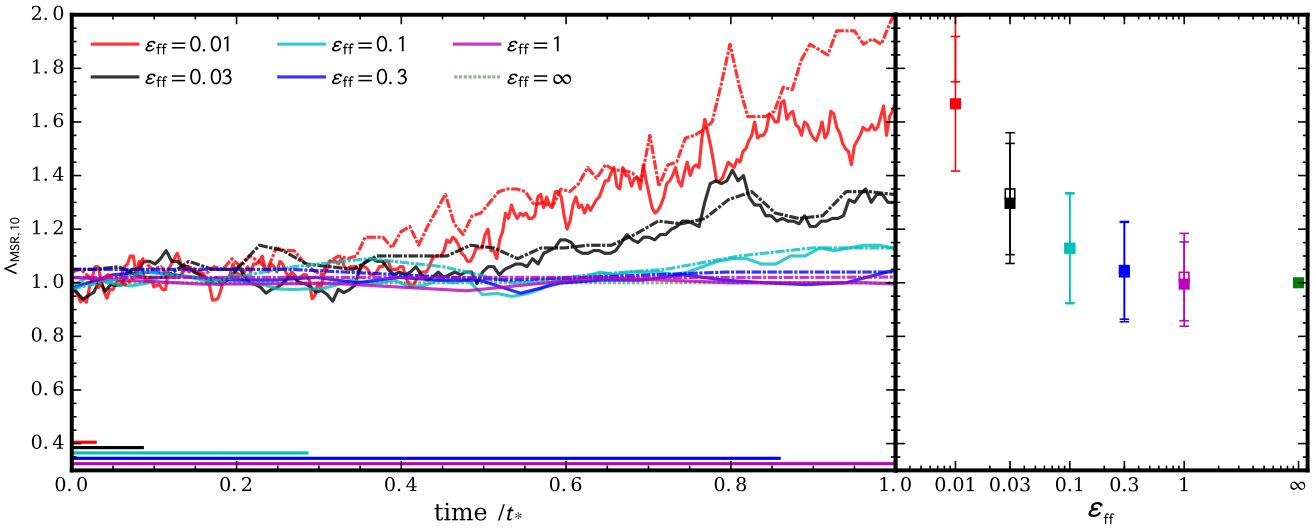

Figure 10. Same as Figure 1 for the mass segregation ratio $\Lambda_{\rm MSR}$ for the 10 most massive stars.

Paper *III*

On the Formation of Runaway Stars BN and x in the Orion Nebula Cluster

Juan P. Farias and Jonathan C. Tan

Accepted for Publication on Astronomy & Astrophysics Letters

Astronomy & Astrophysics manuscript no. main
March 27, 2018

Letter to the Editor

On the Formation of Runaway Stars BN and x in the Orion Nebula Cluster

Juan P. Farias[1] and Jonathan C. Tan[1,2]

[1] Dept. of Space, Earth & Environment, Chalmers University of Technology, Gothenburg, Sweden
[2] Dept. of Astronomy, University of Virginia, Charlottesville, VA 22904, USA

March 27, 2018

ABSTRACT

We explore scenarios for the dynamical ejection of stars BN and x from source I in the Kleinmann-Low nebula of the Orion Nebula Cluster (ONC), which is important for being the closest region of massive star formation. This ejection would cause source I to become a close binary or a merger product of two stars. We thus consider binary-binary encounters as the mechanism to produce this event. By running a large suite of *N*-body simulations, we find that it is nearly impossible to match the observations when using the commonly adopted masses for the participants, especially a source I mass of 7 $M_\odot$. The only way to recreate the event is if source I is more massive, i.e., $\sim 20\ M_\odot$. However, even in this case, the likelihood of reproducing the observed system is low. We discuss the implications of these results for understanding this important star-forming region.

Key words. methods: numerical — stars: formation — stars: kinematics and dynamics

1. Introduction

The Kleinmann-Low (KL) Nebula is a well-studied region in the Orion Nebula Cluster (ONC), being the closest, ≃400 pc (Menten et al. 2007; Kounkel et al. 2017) location where massive stars are forming. In particular, radio source I is likely to be a massive protostar (Churchwell et al. 1987; Garay et al. 1987). Close to the KL Nebula is the Becklin–Neugebauer (BN) object (Becklin & Neugebauer 1967). BN is a young, massive (8.0-12.6 $M_\odot$, Scoville et al. 1983; Rodríguez et al. 2005) star, with fast 3D motion through the ONC of about 30 km s^{-1} , i.e., it is a "runaway" star. The origin of this motion has been a matter of debate. One scenario is that BN was dynamically ejected from the θ^1Ori C system (now a binary) in the Trapezium grouping near the center of the ONC about 4,000 years ago (Tan 2004). This hypothesis has been supported with *N*-body simulations (Chatterjee & Tan 2012), which show several current properties of θ^1Ori C, including orbital binding energy and recoil proper motion, can be understood to result from the ejection of BN.

An alternative scenario has been proposed by Bally & Zinnecker (2005) and Rodríguez et al. (2005) who suggested that dynamical interaction of BN, source I and perhaps an additional member, originally proposed to be radio source n, could have resulted in the high proper motions of BN and radio source I that are approximately in opposite directions. Details of this third member are crucial for this scenario since momentum conservation using BN and source I alone results in a mass for source I of $\sim 20\ M_\odot$ in contrast to the 7 $M_\odot$ estimations from gas motions near the source (Matthews et al. 2010; Hirota et al. 2014; Plambeck & Wright 2016).

Recent observations using multi-epoch high resolution near-IR images from the *Hubble Space Telescope (HST)* (Luhman et al. 2017) have shown high proper motion of another star, source x, that strongly indicate that it was the third member of the multiple system (see Figure 1). Given source x's mass ($\sim 3\ M_\odot$) and proper motion, now the mass estimation for source I via momentum conservation and from circumstellar disk gas dynamics are in better agreement at $\sim 7\ M_\odot$. It has been also argued that if source I was a loose binary that merged during the interaction, e.g., 6 and 1 $M_\odot$ stars, the released potential energy would be more than enough to explain the kinetic energy of the system.

However, there are some aspects of this scenario that appear questionable. In particular, it involves the most massive star, BN, being ejected as a single star from a binary of two much lower mass stars, i.e., with total mass of $\sim 7\ M_\odot$. Thus in this paper we carry out numerical experiments to explore this scenario. We focus on the case where a binary source I (with components I_1 and I_2) interacted with another binary composed of BN and source x in a bound system that resulted in the dynamical ejection of source x and BN.

We present a set of $\sim 10^7$ pure *N*-body scattering simulations focused on the possible binary-binary interaction event that formed the observed system. We first test the scenario presented by Luhman et al. (2017) and then modify some of the parameters, especially source I's mass, to test the sensitivity of the results. We describe our methods and initial conditions in §2, present our results in comparison to the observed system in §3 and discuss our findings and draw conclusions in §4.

2. Methods

We explore the scenario in which the ejection of BN and source x was caused by a dynamical decay of a multiple system that included source I, which was two stars in the past that may have merged as a result of the dynamical interaction. Ignoring situations with pre-existing triples and higher-order multiples that require large numbers of parameters for their description, three possible cases can be considered as initial conditions for this event involving four members. Case 1: a binary-binary inter-

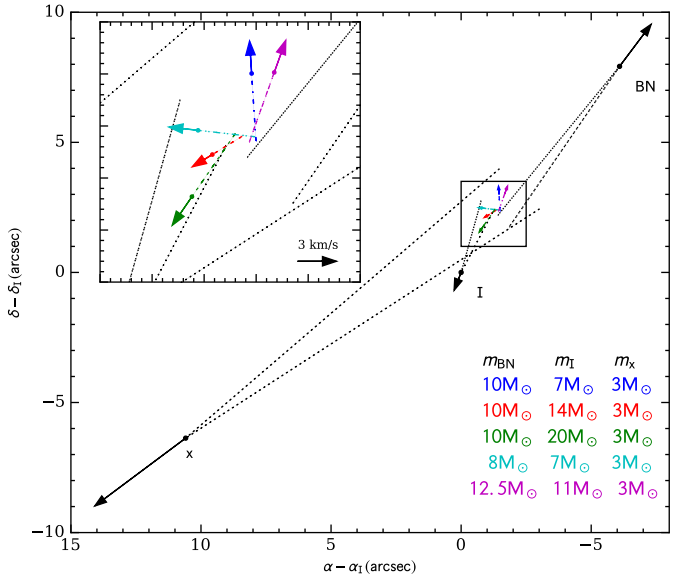

Fig. 1. Overview of the ejection scenario, also showing the center of mass motion given different combinations of masses explored in this work. Filled circles show actual positions of the stars and of the center of mass, dashed lines track the positions 540 years ago (1σ error cones shown for BN, I and x) and solid lines with arrows show 100 years into the future based on current proper motions in the rest frame of Orion (see Luhman et al. 2017). Different colors show various mass combinations of the stars that we have explored. Positions are relative to source I ($\alpha(J2000) = -05^h35^m14\overset{s}{.}516$ and $\delta(J2000) = -05°22'30\overset{''}{.}59$, Rodríguez et al. 2017).

action; Case 2: a binary system perturbed by two single stars; and Case 3: all stars were single stars. For simplicity we explore only the first case, which is arguably the most probable since it involves close interaction of only two initially independent systems. Cases 2 and 3 involve the coordinated close encounter of 3 and 4 systems, respectively, which makes them intrinsically less likely. Thus, we do not consider Cases 2 and 3 further in this letter.

Within Case 1 there are three possible initial combinations that we label as A: [I_1 I_2][BN x]; B: [I_1 BN][I_2 x] and C: [I_1 x][I_2 BN], where [a b] indicates a binary pairing of stars a and b. We look for interactions that result in the outcome [I_1 I_2]BN x, i.e., with the ejection of BN and x leaving the binary [I_1 I_2] with or without a merger, that we will refer to as `BNx-ejection`. From this subset of cases we identify those in which the velocities of the individual stars are within 2-σ of the observed values reported by Luhman et al. (2017) and Rodríguez et al. (2017) as `BNx-velocity`.

For our fiducial case, we adopt the same masses discussed by Luhman et al. (2017), i.e., $m_x = 3\ M_\odot$, $m_{BN} = 10\ M_\odot$ and $m_I = 7\ M_\odot$ (Matthews et al. 2010; Hirota et al. 2014; Plambeck & Wright 2016). Assuming that source I was two stars, binary or not, we assume a mass ratio $q = 0.166$ for its members (i.e., $m_{I_1} = 6\ M_\odot$ and $m_{I_2} = 1\ M_\odot$), but we have also tested a range of other values finding no major change in the results due to this choice. The radius of the individual stars are taken from stellar models developed by Hurley et al. (2000). We assume I_1 and I_2 are protostars or pre-main-equence stars and thus increase their radius by a factor $\eta \geq 1$ to account for the more extended radii that a protostar should have relative to a main sequence star of the same mass, adopting $\eta = 2$ as a simple, fiducial choice. We also test the sensitivity of our results to this factor finding no major difference on the results except when this becomes ≥ 3 at which point the energy of ejections falls considerably.

Given the previous assumptions, there are then several combinations of parameters that set the initial conditions of each experiment. Our standard procedure is to choose them randomly from expected distributions, summarized as follows: (1) The semimajor axis a of each binary is taken from a uniform, random distribution in logarithmic space in the range $a = 0.1 - 6300$ AU. (2) The eccentricity of each binary is chosen using two extreme distributions: A) Using only circular orbits, i.e., $e_i = 0$, which might be expected if binaries formed via circumstellar disks; B) A thermal distribution (Heggie & Hut 2003), i.e., $dF_b/de = 2e$, which is the extreme scenario in which binary systems have had enough time to thermalize via stellar encounters. (3) The direction of the angular momentum vector of each binary is chosen randomly, as is (4) the initial orbital phase of the binaries. The above parameters define the internal properties of each binary.

Next come the parameters that define the interaction itself. We setup the experiments in order to only have initially bound systems, i.e., if both binaries were single stars they would remain bound after the interaction. Therefore, (5) the relative velocity at infinity v_i is drawn from a Maxwell-Boltzmann velocity distribution with $\sigma = 3$ km s^{-1} truncated at the critical velocity

$$v_c = \sqrt{\frac{G}{\mu}\left(\frac{m_{11}m_{12}}{a_1} + \frac{m_{21}m_{22}}{a_2}\right)}, \quad (1)$$

where G is the gravitational constant, $m_1 = m_{11} + m_{12}$ and $m_2 = m_{21} + m_{22}$ are the masses of each binary, summing their respective components, and $\mu = (m_1 + m_2)/(m_1 m_2)$ is the reduced mass of the system (see Gualandris et al. 2004). Thus v_c is the velocity below which the total energy of the system in the four body center of mass is negative, and therefore the ejected stars are the result of dynamical interaction and not of the initial conditions. Also, full ionization is not possible, i.e., there will be always a binary (or merged stars) left behind.

Next is: (6) the impact parameter, b, which is drawn randomly in discrete bins of radii $b_i = 2^{i/2}b_0$ following the method of McMillan & Hut (1996) to calculate cross sections of the relevant interactions. We choose $b_0 = 100$ AU and increase i until no relevant outcomes are encountered. Then, the contribution of the events in each bin i to the final cross section of this event Σ_X is $\pi(b_i^2 - b_{i-1})N_{X,i}/N_i$ with $N_{X,i}$ and N_i being the number of events X and the number of trials respectively, both inside the i-th bin. The contribution of bin i to the squared uncertainty in the calculation, $(\delta\Sigma_X)^2$, is $[\pi(b_i^2 - b_{i-1})/N_i]^2 N_{X,i}$ (McMillan & Hut 1996). For the first bin we have chosen $N_{i=1} = 500\,000$.

Simulations are performed using the `Fewbody` software (Fregeau et al. 2004), an accurate Runge-Kutta integrator which conserves energy and angular momentum to the order of 10^{-8}. It also uses the "sticky star" approximation for collisions with no mass loss and an expansion factor of the merger product of $f_{exp} = 2$.

The above method is repeated for different combinations of the member masses. All these combinations with their respective total momentum vectors are shown in Figure 1.

3. Results

Table 1 summarises the resulting interaction cross sections and branching ratios (BR), i.e. the number of cases over the total number of simulations for each configuration, for the

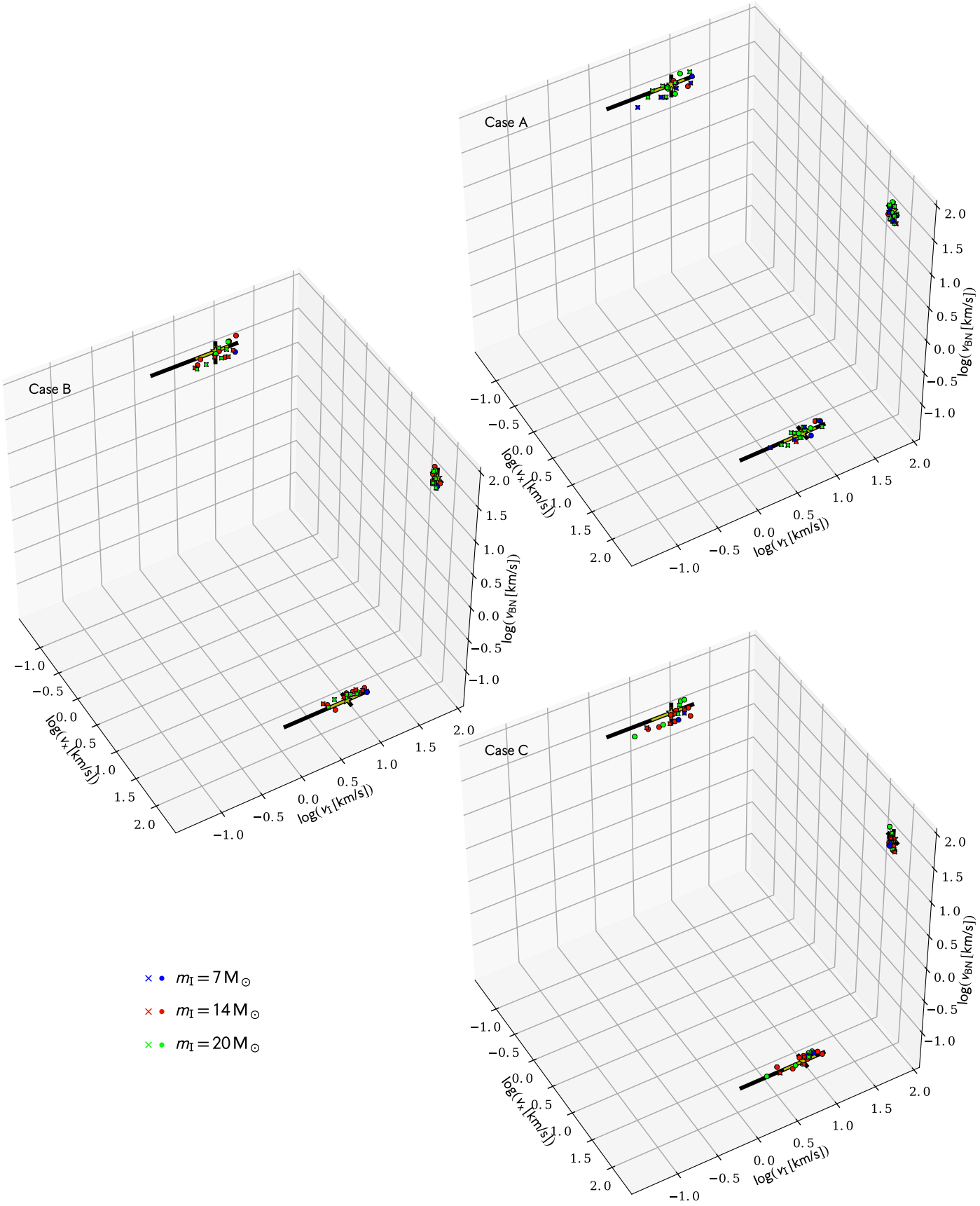

Fig. 2. Simulation results compared with observed velocities. Case A, Case B and Case C panels shows the resulting velocities that match the `BNx-ejection` event in the three velocity planes for sources I, x and BN for each respective initial combination varying only the mass of source I. Crosses and filled circles represent the adopted eccentricity distribution with thermal and circular eccentricities, respectively. Yellow star and errorbars shows the observed values with its standard error. Highlighted symbols represent `BNx-velocity` matches. Black errorbars shows the range on which `BNx-velocity` was searched, i.e., 2σ errors.

Table 1. Interaction cross sections for the different mass combinations

				BNx-ejection		BNx-velocity		
Case	Eccentricity	$m_{\rm I}$ [$M_\odot$]	$m_{\rm BN}$ [$M_\odot$]	Σ [$\times 10^6$AU^2]	BR [$\times 10^{-3}$]	Σ [AU^2]	BR [$\times 10^{-6}$]	$N_{\rm sims}$[$\times 10^6$]
A	circular	7	10	2.82 ± 0.02	35.0	0.2 ± 0.2	0.392	5.10
A	thermal	7	10	1.84 ± 0.01	29.4	2 ± 2	1.17	5.11
A	circular	14	10	6.65 ± 0.04	39.4	16 ± 8	6.85	5.11
A	thermal	14	10	4.55 ± 0.03	32.9	11 ± 4	7.88	5.71
A	circular	20	10	9.95 ± 0.07	38.3	49 ± 9	31.8	6.09
A	thermal	20	10	6.72 ± 0.04	38.4	44 ± 10	25.1	5.71
A	circular	7	8	3.29 ± 0.02	37.5	0.5 ± 0.3	0.780	5.13
A	thermal	7	8	2.01 ± 0.02	35.2	1.0 ± 0.9	1.04	4.81
A	circular	7	12.5	2.37 ± 0.02	28.1	< 0.06	< 0.12	8.50
A	thermal	11	12.5	1.50 ± 0.01	25.5	0.8 ± 0.8	0.195	5.12
B	circular	7	10	0.018 ± 0.002	0.240	0.06 ± 0.06	0.125	8.0
B	thermal	7	10	0.008 ± 0.001	0.208	< 0.06	< 0.13	7.5
B	circular	14	10	0.21 ± 0.01	4.53	1.5 ± 0.4	2.58	5.4
B	thermal	14	10	0.101 ± 0.004	3.87	2.1 ± 0.6	3.12	4.81
B	circular	20	10	0.53 ± 0.01	12.7	25 ± 14	13.7	5.41
B	thermal	20	10	0.293 ± 0.008	10.4	15 ± 2	16.8	5.12
B	circular	7	8	0.023 ± 0.001	0.458	0.06 ± 0.06	0.133	7.51
B	thermal	7	8	0.011 ± 0.001	0.347	0.2 ± 0.2	0.444	4.5
B	circular	11	12.5	0.018 ± 0.003	0.124	< 0.06	< 0.20	5.12
B	thermal	11	12.5	0.0069 ± 0.0008	0.111	< 0.06	< 0.13	7.40
C	circular	7	10	0.017 ± 0.001	0.490	0.1 ± 0.1	0.125	8.01
C	thermal	7	10	0.011 ± 0.001	0.273	0.06 ± 0.06	0.125	8.01
C	circular	14	10	0.045 ± 0.002	1.35	3 ± 2	0.823	8.51
C	thermal	14	10	0.043 ± 0.004	1.34	4 ± 1	3.13	5.12
C	circular	20	10	0.083 ± 0.004	2.15	51 ± 18	8.21	5.12
C	thermal	20	10	0.081 ± 0.005	2.66	36 ± 16	8.67	5.42
C	circular	7	8	0.020 ± 0.001	0.847	0.1 ± 0.1	0.133	7.51
C	thermal	7	8	0.012 ± 0.001	0.494	0.13 ± 0.09	0.266	7.51
C	circular	11	12.5	0.011 ± 0.001	0.281	0.1 ± 0.1	0.222	4.51
C	thermal	11	12.5	0.011 ± 0.002	0.141	< 0.06	< 0.20	5.11

`BNx-ejection` and `BNx-velocity` cases. The interaction cross sections of the `BNx-ejection` case are considerably larger for Case A, with $\Sigma_{\texttt{BNx-ejection}} = (2.8 \text{ and } 1.8) \times 10^6$AU^2 for the fiducial (i.e., $m_{\rm BN} = 10\ M_\odot, m_{\rm I} = 7\ M_\odot, m_{\rm x} = 3\ M_\odot$) circular and thermal cases, respectively. Such large cross sections, together with branching ratios of several percent of the `BNx-ejection` event in the fiducial case that we show in Figure A.1 and discuss further in Appendix A, implies that the ejection of the massive BN object and source x from the system is quite possible.

However, when considering the velocities of the ejected stars in the `BNx-velocity` case, the cross sections drop to ~ 1 AU^2 in all fiducial cases. We have checked that this result is independent of the assumed mass ratio of the source I components. Also, if η is greater, then the chance of obtaining the observed velocities becomes even smaller, due to the energy constraints that the radii of the stars imply. We have found that to match the observed velocities the parameter η must be no larger than 3, i.e., for a given mass, the protostars should not have radii larger than 3 times the radii of a main sequence star of the same mass.

The situation becomes more favorable only if the mass of source I is $> 7 M_\odot$. In the best case we explored, with $m_{\rm I} = 20 M_\odot$ cross sections increase by a factor between ~ 20 to 600 in the different initial configurations. However, the cross sectional areas are still small, $\sim$10 to 50 AU^2, which means that these events are quite rare when compared to the whole ensemble of outcomes. In Appendix A we present and discuss the branching ratios of all

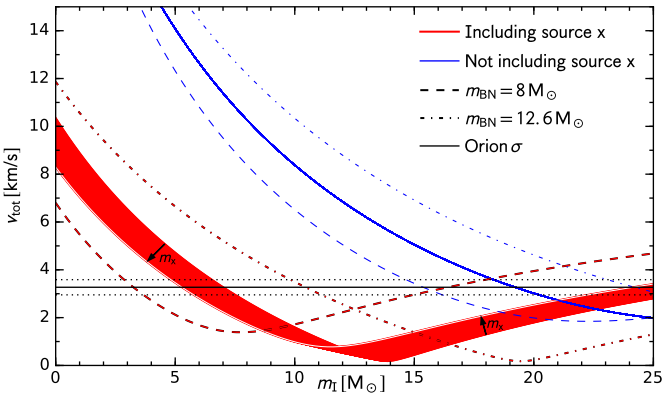

Fig. 3. The system (center of mass) velocity as a function of the mass of source I (see also Figure 1). Red lines show the scenario where source x is part of the ejection event as suggested by Luhman et al. (2017) [1]. The red shaded area shows the result of varying the mass of source x between 2.5-3.0 $M_\odot$, with the black arrows showing the direction of the increment. Blue lines show the scenario if source x was not part of the event. In both red and blue cases, the dashed and dot-dashed lines show results of adopting the lower and upper limits of BN's mass, respectively (Rodríguez et al. 2005).

[1] Note that there is an error in the units for the velocity associated with the specific momentum that they mention: it should be 1.4 mas yr^{-1} instead of km s^{-1}.

the possible outcomes of our experiments sorted from the most to least probable.

4. Discussion and Conclusions

Our simulations indicate that a more massive source I has a better chance to produce the observed system. Figure 3 shows a scatter plot of the velocities obtained in each setup when varying source I's mass. The yellow star and errorbars show the observed system. There is a very specific trend that appears in the $v_{\rm BN} - v_{\rm I}$ panels in Figure 3 showing that the observed system appears to be one order of magnitude above the trend for source I that has a mass of 7 $M_\odot$. Increasing source I's mass naturally places simulations in agreement with observations. Even though we have shown this type of event is quite rare in terms of branching ratios with respect to all possible outcomes, if by chance it happens with the correct released energy, the observed velocities would be only achieved if the mass of source I is not so small. This is also supported by the other velocity panels in all the Cases A, B and C.

Some caveats associated with our analysis should be mentioned. For example, we have ignored the dynamical effects of gas expulsion. The modeling of Chernoff et al. (1982) implies about 4 $M_\odot$ of gas has been ejected from the central region over a period of 1200 years requiring an energy of $\gtrsim 5 \times 10^{47}$ erg. If a large fraction of this gas was ejected impulsively at the time of dynamical interaction, then this could alter some of the specific results of our analysis: e.g., an even greater energy needs to be liberated in the dynamical interaction. However, we note that the gas has been ejected quasi-isotropically from BN-KL (see, e.g., Allen & Burton 1993; Bally et al. 2017), so that the effects on the plane-of-sky momentum analysis are not expected to be so large. Still, future modeling could allow for, e.g., a variable mass of stars during the interaction, i.e., sudden mass loss occuring as part of any merger event. Other caveats include that we have ignored the dynamical effects of any other masses, including other surrounding stars and gas components. Still, these are expected to be relatively minor since the velocities of the stars are relatively large compared to the velocity dispersion of the ambient material in the region.

The recent evidence that source x was involved in the ejection of the BN Object appeared to reconcile the incongruence between the mass of source I estimated by momentum analysis and estimations via rotation of its putative circumstellar disk. However, if we re-do momentum analysis with the new data we can see that source x's participation is not enough support for the low mass estimations of source I. Figure 3 shows the momentum analysis for the old and new scenarios as a function of source I mass. Blue lines shows the scenario where only source I and BN participated in the ejection with the upper and lower limits of BN's mass as dashed lines. The only way the system center of mass can be moving within the velocity dispersion of the ONC (black solid line) is if source I's mass is at least 20 $M_\odot$. Now, it has been argued that the inclusion of source x would remove this constraint. The former is true as we can see in the red lines on Figure 3, however, for the system to be moving within the velocity dispersion of the ONC, source I's mass could actually be in a very wide range of masses, from 5 to 25 $M_\odot$ with a minimum near 14 $M_\odot$.

Figure 1 shows the present center of mass with different mass combinations used in this work. If the individual masses are those adopted by Luhman et al. (2017) (blue arrow) the system is moving mostly outwards, away from the center of the ONC. However, if source I is more massive (red and green arrows) the system velocity points towards the center of the cluster, i.e., towards the Trapezium. We consider that a scenario involving infall of a dense molecular gas core from which the protostars are forming is more likely than one involving motion of the core out from the cluster center. For example, passage near the strong ionizing radiation from θ^1C is expected to have had potentially very disruptive effects on the core if it had previously been located near the Trapezium.

In conclusion, we have shown that the ejection of BN and x from source I (as a binary or merged binary) as presented by Luhman et al. (2017), i.e., with a relatively low mass for source I of $\sim 7\ M_\odot$ that is less than BN's mass, is in general a very unlikely event. In particular, with the given masses and observed velocities it is nearly impossible to reproduce the observations with the binary-binary interactions we have considered. If the interaction occurred as we have explored, then it is more probable that source I is much more massive than the preferred value of 7 $M_\odot$ presented by Luhman et al. (2017) and others. Thus future measurements of the mass of source I are needed to better constrain this proposed ejection scenario.

However, other possible initial combinations remain to be explored, e.g., a binary perturbed by two stars (i.e., effectively a 3-body initial interaction), or all initial single stars (i.e., a 4-body initial interaction), but these are expected to be inherently rarer and there is no reason to think these combinations could increase the chances significantly since the binary-binary interaction is the most likely to release the necessary energy to produce the ejection. A single star interacting with a pre-existing triple remains a possibility that needs to be considered, especially if the dynamical mass of source I does turn out to be at the low end of the range modeled, i.e., $\sim 7\ M_\odot$. Such interactions could also include unbound fly-bys. This would be the only way to reconcile the scenario of BN's ejection from $\theta^1 C$ (Tan 2004; Chatterjee & Tan 2012) with ejection of source x, although plane-of-sky momentum conservation would appear to place challenging constraints on such a model if BN suffered only minor accelerations and course deflections in such a fly-by.

References

Allen, D. A. & Burton, M. G. 1993, Nature, 363, 54
Bally, J., Ginsburg, A., Arce, H., et al. 2017, ApJ, 837, 60
Bally, J. & Zinnecker, H. 2005, AJ, 129, 2281
Becklin, E. E. & Neugebauer, G. 1967, ApJ, 147, 799
Chatterjee, S. & Tan, J. C. 2012, ApJ, 754, 152
Chernoff, D. F., McKee, C. F., & Hollenbach, D. J. 1982, ApJ, 259, L97
Churchwell, E., Felli, M., Wood, D. O. S., & Massi, M. 1987, ApJ, 321, 516
Fregeau, J. M., Cheung, P., Portegies Zwart, S. F., & Rasio, F. A. 2004, MNRAS, 352, 1
Garay, G., Moran, J. M., & Reid, M. J. 1987, ApJ, 314, 535
Gualandris, A., Portegies Zwart, S., & Eggleton, P. P. 2004, MNRAS, 350, 615
Heggie, D. & Hut, P. 2003, The Gravitational Million-Body Problem: A Multidisciplinary Approach to Star Cluster Dynamics
Hirota, T., Kim, M. K., Kurono, Y., & Honma, M. 2014, ApJ, 782, L28
Hurley, J. R., Pols, O. R., & Tout, C. A. 2000, MNRAS, 315, 543
Kounkel, M., Hartmann, L., Loinard, L., et al. 2017, ApJ, 834, 142
Luhman, K. L., Robberto, M., Tan, J. C., et al. 2017, ApJ, 838, L3
Matthews, L. D., Greenhill, L. J., Goddi, C., et al. 2010, ApJ, 708, 80
McMillan, S. L. W. & Hut, P. 1996, ApJ, 467, 348
Menten, K. M., Reid, M. J., Forbrich, J., & Brunthaler, A. 2007, A&A, 474, 515
Plambeck, R. L. & Wright, M. C. H. 2016, ApJ, 833, 219
Rodríguez, L. F., Dzib, S. A., Loinard, L., et al. 2017, ApJ, 834, 140
Rodríguez, L. F., Poveda, A., Lizano, S., & Allen, C. 2005, ApJ, 627, L65
Scoville, N., Kleinmann, S. G., Hall, D. N. B., & Ridgway, S. T. 1983, ApJ, 275, 201
Tan, J. C. 2004, ApJ, 607, L47

Appendix A: Branching ratios for all the possible outcomes

By calculating interaction cross sections for the `BNx-ejection` case we have obtained a large number of interactions on the order of a few millions per simulation set with impact parameters from near zero to as large thousands of AU, by which point no interesting interaction happens. With this large set of simulations we can calculate branching ratios of rare interactions down to $\sim 10^{-6}$. We have classified the outcomes of each experiment using a similar classification as Fregeau et al. (2004), however we distinguish the cases where there was an exchange of members or a capture of one of the members by one of the binary systems. Figure A.1 shows all the possible outcomes in this study sorted from the most to the least probable in our fiducial case with circular orbits. This trend is similar for the setups with thermal eccentricities. Figure A.1 shows that these models with thermal eccentricities have a greater chance to obtain a merger, but not in outcomes that could form the observed BN-x-I system.

In all setups, the most probable case is preservation i.e., the configuration of each setup does not change, happening $\sim 50\%$ of the time, followed by the "Triple+Single" case, i.e., the formation of a stable triple by capturing one member of the other binary ($\sim 20\%$). Our case of interest for Case A, i.e., "2 Singles+Binary", comes in third place happening $\sim 10\%$ of the time. [I_1 I_2]BN x is a subset of this case. The branching ratio of this specific subset is marked with the same symbol connected by a line to the parent set in Figure A.1. The end of the line shows the branching ratio of the subset that also match the observed velocities within 2σ. A left triangle marking the end of the line means that we did not find any velocity match for this case and the branching ratio is smaller than the position of the symbol. The branching ratio of [I_1 I_2]BN x is quite high ($\sim 4.5\%$), this means that the case where the most massive star (BN) is ejected is not so rare. However, it is almost impossible to match the observed velocities in this particular case with the masses assumed by Luhman et al. (2017). Increasing the mass of source I considerably improves the chances to obtain the observed velocities, going from a branching ratio of $< 4 \times 10^{-7}$ i.e., not a single case with $m_{\rm I} = 7\ {\rm M}_\odot$ to a branching ratio of $\sim 2 \times 10^{-5}$ for $m_{\rm I} = 20\ {\rm M}_\odot$ (with $m_{\rm I_1} = 17.14\ {\rm M}_\odot$ and $m_{\rm I_2} = 2.86\ {\rm M}_\odot$).

The matching outcome for Cases B and C without a merger involves an exchange of members, which makes the outcome less frequent, but still comparable with the original case. The mass of source I also influences the branching ratios of the matching velocity outcomes, favoring the cases where source I is more massive.

This trend also remains the same when considering a merger between I_1 and I_2, see the "3 Singles" case in Fig. A.1. Even though the branching ratios of these cases are smaller, the chances of obtaining the matching velocities are higher since it is the extreme case where most of the potential energy stored by the binary is released to the system members. How much energy is set by the semimajor axis and also individual radius of the source I original stars. For this situation, the radii of the protostars, parameterized by the factor η, is one of the largest unknowns in the system and one of the most important, since it sets the upper limit on the amount of energy the source I merger can provide.

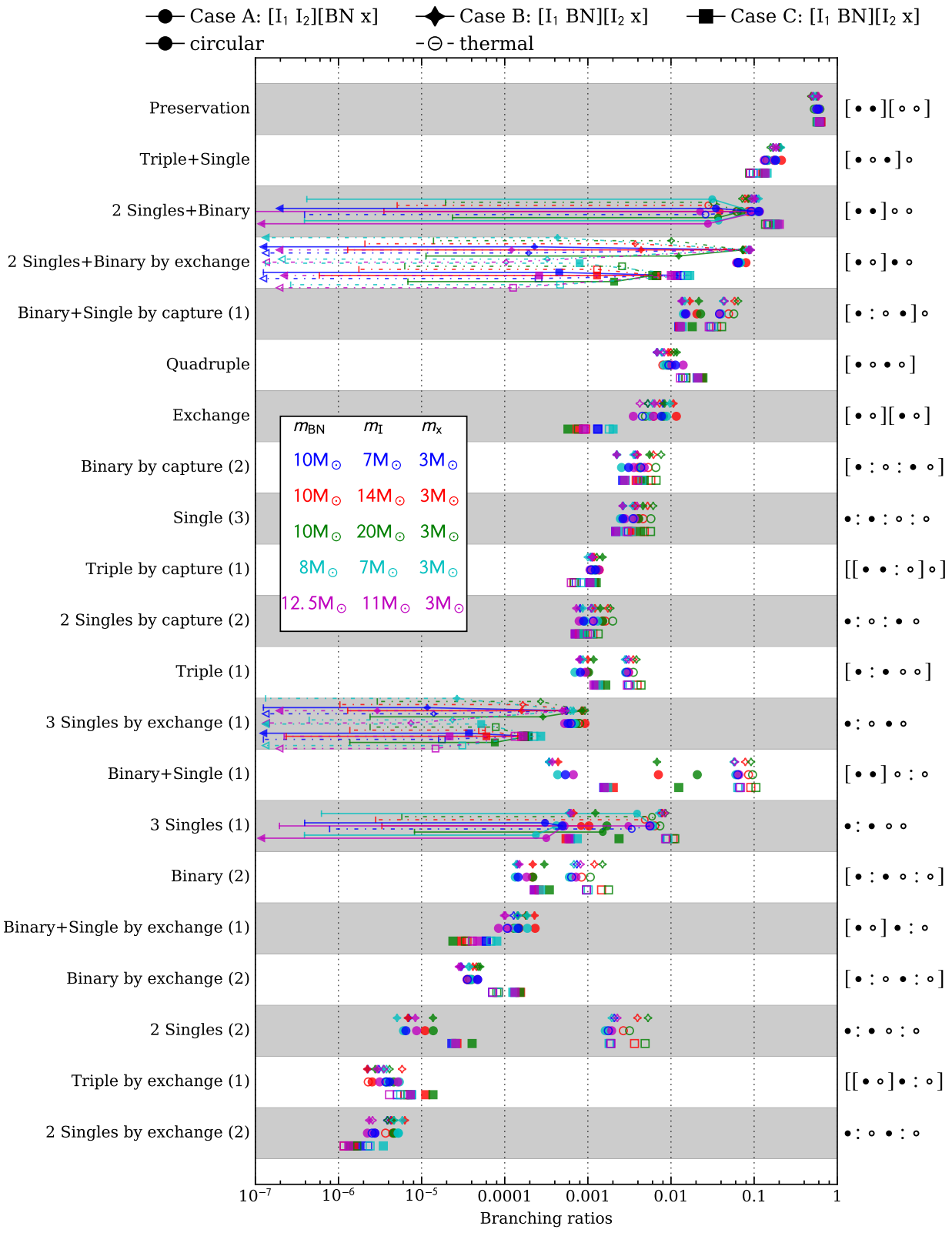

Fig. A.1. Branching ratios collected for all possible outcomes and experiments carried out in this work. Results are sorted from the most to the least probable in the fiducial case (blue filled circle). Different symbols represent the different initial configurations: Case A (circles); Case B (diamonds); and Case C (squares). Open symbols show cases with thermal distribution of eccentricities, while filled symbols show where all binaries have circular orbits initially. Colors show the different assumed masses (see legend). Left axis labels are the names used to refer to each outcome with the number of collisions needed for each outcome appearing in parentheses. Right labels show the schematic representation of each outcome, similar to Fregeau et al. (2004), but we distinguish between exchange of members or preservation of membership of the original binaries. Branching ratios of cases that match the BN-x-I observed configuration are a subset of some of the listed outcomes, these are connected to their parent outcome by a line (dashed for open symbols, solid for filled symbols). We mark outcomes where no matching velocity was found with a left triangle denoting the upper limit of their branching ratio. Thus only the outcomes that contain horizontal lines have some chance of producing the observed BN-x-I system, although typically we only have upper limits on the branching ratio that leads to the observed system.